Distributed Joule-Thomson microcooling for optical detectors in space

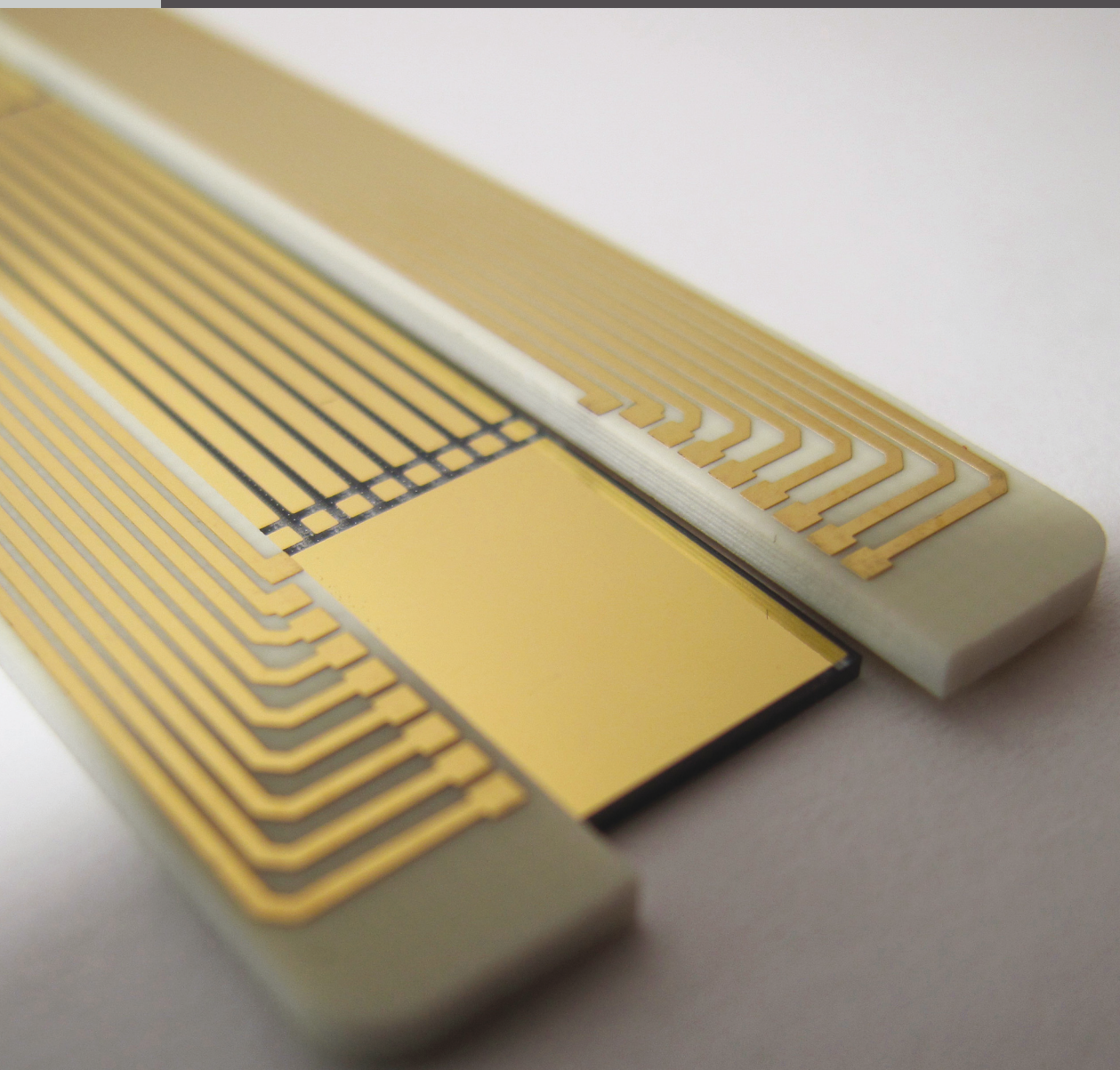

Hendrie Derking

DISTRIBUTED JOULE-THOMSON MICROCOOLING FOR OPTICAL DETECTORS IN SPACE

Hendrie Derking

Ph.D. committee:

Chairman	
prof. dr. G. van der Steenhoven	University of Twente
Secretary	
prof. dr. G. van der Steenhoven	University of Twente
Supervisor	
prof. dr. ir. H.J.M. ter Brake	University of Twente
Members	
prof. dr. ir. A.J.P. Theuwissen	Delft University of Technology
prof. dr. ir. T.H. van der Meer	University of Twente
prof. dr. J.G.E. Gardeniers	University of Twente
Dr. rer. nat. et Ing. habil. C. Haberstroh	Technical University of Dresden
dr. ir. H.V. Jansen	University of Twente

Frontcover: A picture of a miniature Joule-Thomson cold stage surrounded by a PCB taken by Harry Holland.
Backcover: Pillar structures in the counter-flow heat exchanger channels of a Joule-Thomson cold stage.

The research described in this thesis was financially supported by the European Space Agency. It was carried out at the Energy, Materials and Systems group of the Faculty of Science and Technology of the University of Twente.

Distributed Joule-Thomson microcooling for optical detectors in space
J.H. Derking
Ph.D. thesis, University of Twente, Enschede, the Netherlands
ISBN: 978-94-6191-027-1
Printed by PrintPartners Ipskamp, Enschede, the Netherlands

DISTRIBUTED JOULE-THOMSON MICROCOOLING FOR OPTICAL DETECTORS IN SPACE

PROEFSCHRIFT

ter verkrijging van
de graad van doctor aan de Universiteit Twente,
op gezag van de rector magnificus,
prof. dr. H. Brinksma,
volgens besluit van het College voor Promoties
in het openbaar te verdedigen
op vrijdag 21 oktober 2011 om 14.45 uur

door

Jan Hendrik Derking

geboren op 7 november 1980
te Hoogeveen

Dit proefschrift is goedgekeurd door de promotor:
prof. dr. ir. H.J.M. ter Brake

Nomenclature

Symbol	Meaning	Unit
A_c	Cross-sectional area	[m^2]
A_{hx}	Heat exchange area	[m^2]
A_{rad}	Radiative heat exchange area	[m^2]
$c_{p,f}$	Specific heat at constant pressure	[J kg^{-1} K^{-1}]
COP	Coefficient of performance	[-]
COP_{carnot}	Coefficient of performance normalized to the Carnot efficiency	[-]
$d\dot{H}$	Net change in enthalpy flow of a fluid	[W]
dx	Small section of length	[m]
D_h	Hydraulic diameter	[m]
FOM	Figure of merit of efficiency of heat exchange	[W m^{-1}]
FOM_{area}	Figure of merit of required heat exchange area	[m]
h	Local heat transfer coefficient	[W m^{-2} K^{-1}]
h	Height	[m]
$h_{Ph,in}$	Specific enthalpy of high-pressure fluid at warm end	[J kg^{-1}]
$h_{Pl,out}$	Specific enthalpy of low-pressure fluid at warm end	[J kg^{-1}]
H	Enthalpy	[J]
l	Length	[m]
L	Length of CFHX	[m]

Continues on next page

Symbol	Meaning	Unit
L	Lorenz number	[$V^2\ K^{-2}$]
$\dot{m}$	Mass-flow rate	[kg s^{-1}]
Nu	Nusselt number	[-]
O	Perimeter	[m]
P	Pressure	[Pa]
P_h	High pressure	[Pa]
P_l	Low pressure	[Pa]
$\dot{Q}_{cond}$	Conductive heat flow	[W]
$\dot{Q}_{conv}$	Convective heat flow	[W]
$\dot{Q}_{exp}$	Heat loss induced by experimental characterization	[W]
$\dot{Q}_{gross}$	Gross cooling power	[W]
$\dot{Q}_{loss,warm}$	Heat loss due to heat flow from the environment into the system	[W]
$\dot{Q}_{net}$	Net cooling power	[W]
$\dot{Q}_{rad}$	Radiative heat flow	[W]
$\dot{Q}_w$	Convective heat flow between wall and fluid	[W]
$\dot{Q}_{wire}$	Conductive heat flow through a wire	[W]
R_{wire}	Wire resistance	[Ω]
Re	Reynolds number	[-]
T	Temperature	[K]
T_c	Cold stage temperature	[K]
T_c	Cold-end temperature	[K]
T_{env}	Temperature of environment	[K]
T_f	Fluid temperature	[K]
T_{fh}	Temperature of high-pressure fluid	[K]
T_{fl}	Temperature of low-pressure fluid	[K]
T_h	High temperature	[K]
T_l	Low temperature	[K]
T_m	Material temperature	[K]
T_m	Mean temperature	[K]
T_w	Wall temperature	[K]
v_f	Mean fluid velocity	[m s^{-1}]
w	Width	[m]
$\dot{W}_{min}$	Minimum compressing power	[W]
x	Position along counter-flow heat exchanger length	[m]
X	Channel aspect ratio	[-]
Greek symbols		
Δh_{cold}	Change in specific enthalpy at cold end	[J kg^{-1}]
Δh_{min}	Minimum isothermal enthalpy difference	[J kg^{-1}]
Δh_{warm}	Change in specific enthalpy at warm end	[J kg^{-1}]
Δs_{warm}	Change in specific entropy at warm end	[J $kg^{-1}\ K^{-1}$]

Continues on next page

Symbol	Meaning	Unit
ε_c	Emissivity of cold stage	[-]
λ_f	Thermal conductivity of a fluid	[W m^{-1} K^{-1}]
λ_m	Thermal conductivity of a material	[W m^{-1} K^{-1}]
μ_f	Dynamic fluid viscosity	[Pa s]
σ_b	Stefan-Boltzmann constant	[W m^{-2} K^{-4}]
σ_m	Electrical conductivity of a material	[Ω^{-1} m^{-1}]
ρ_f	Fluid density	[kg m^{-3}]
Abbreviations		
BLIP	Background limited infrared photodetector	[-]
CCD	Charge coupled device	[-]
CFHX	Counter-flow heat exchanger	[-]
CMOS	Complementary-metal-oxide-silicon	[-]
CTE	Coefficient of thermal expansion	[-]
IC	Integrated circuit	[-]
IR	Infrared	[-]
JT	Joule-Thomson	[-]
LH	Linde-Hampson	[-]
LWIR	Long wavelength infrared	[-]
MEMS	Micro-electro-mechanical-system	[-]
MWIR	Middle wavelength infrared	[-]
NIR	Near infrared	[-]
PCB	Printed circuit board	[-]
QWIP	Quantum well infrared photodetector	[-]
RAL	Rutherford Appleton Laboratory	[-]
ROIC	Read-out integrated circuit	[-]
SMD	Surface mounted device	[-]
Sub-mm	Sub millimeter	[-]
SWIR	Short wavelength infrared	[-]
TMM	Thermal mathematical model	[-]
UV	Ultraviolet	[-]
VIS	Visible	[-]
Semiconductors		
AlGaAs	Aluminum-gallium-arsenide	[-]
As	Arsenic	[-]
Ga	Gallium	[-]
GaAs	Gallium arsenide	[-]
Ge	Germanium	[-]
HgCdTe	Mercury-cadmium-telluride	[-]
InGaAs	Indium-gallium-arsenide	[-]
InP	Indium phosphorus	[-]
InSb	Indium antimony	[-]

Continues on next page

Symbol	Meaning	Unit
PtSi	Platinum silicide	[-]
Si	Silicon	[-]
Subscripts		
f	Fluid	[-]
h	High pressure line	[-]
l	Low pressure line	[-]

Contents

CHAPTER 1

Introduction

Miniature Joule-Thomson (JT) coolers have a high potential for cooling a wide variety of electronic devices, including optical detectors in space missions, low-noise amplifiers, and semiconducting and superconducting electronics. These devices are cooled to reduce their thermal noise, to increase the bandwidth or to obtain superconductivity. For these applications, the cooler should be small, low-cost, low-interference and have a very long life-time. At the University of Twente, the miniaturization of JT coolers have been investigated for many years. This research resulted in the realization of micromachined JT cold stages with a cooling power around 10 to 20 mW at 100 K.

In 2007, two follow-up projects were started. Under support of the Dutch Technology Foundation (STW), the development of two-stage JT cold stages is investigated as well as the integration of JT cold stages with a sorption compressor and a small vacuum chamber. Under support of the European Space Agency (ESA), the utilization of single-stage micromachined JT cold stages for cooling small detector systems in future space missions is investigated. The latter is the topic of this thesis.

In this chapter, the basic cooling cycle of a JT cooler, the Linde-Hampson cycle, is described and an overview of miniature JT coolers is given. Furthermore, the motivation and goals of the research described in this thesis are considered. This chapter ends with the outline of the thesis.

1.1 Linde-Hampson cooling cycle

A Joule-Thomson (JT) cooler is based on the Linde-Hampson (LH) cooling cycle of which a schematic representation is shown in Fig. 1.1. Basically, a LH cycle consists of a counter-flow heat exchanger (CFHX), a JT valve or restriction, an evaporator and a compressor with an aftercooler. The heat of compression is, usually, rejected to the environment in an aftercooler heat exchanger, which in Fig. 1.1 is assumed to be part of the compressor. In the cooling cycle, a warm high-pressure fluid flows through a CFHX exchanging heat with the colder low-pressure fluid that flows in the opposite direction. The high-pressure fluid thus cools and reaches the JT restriction at a lower temperature. There, it expands adiabatically and partly liquefies. A heat load, resulting from the device to be cooled, then evaporates the liquid, and the vapor flows back through the CFHX. In a closed cycle, a compressor pressurizes the low-pressure fluid back to the high pressure.

The operating temperature of a JT cooler with a pure fluid as refrigerant is determined by the boiling temperature of the refrigerant at the low pressure [1]. The gross cooling power ($\dot{Q}_{gross}$) is defined as the change in enthalpy of the working fluid at the cold end. In a perfect CFHX, no heat is exchanged with the environment and a maximum amount of enthalpy is exchanged between the high-pressure fluid and the low-pressure fluid. Since the JT expansion is isenthalpic, the change in specific enthalpy of the fluid at the warm end (Δh_{warm}) equals that one at the cold end (Δh_{cold}) [1]. The gross cooling power of a pure refrigerant JT cooler can thus be determined by the change in enthalpy of the fluid at the compression temperature, i.e. after compression and re-cooling,

$$\dot{Q}_{gross} = \dot{m}\Delta h_{cold} = -\dot{m}\Delta h_{warm} \tag{1.1}$$

where $\dot{m}$ is the mass-flow rate.

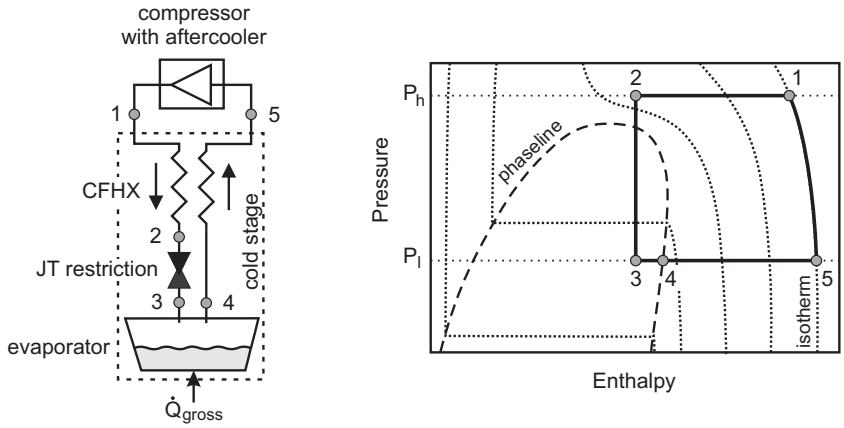

Figure 1.1: Left: Schematic representation of a Linde-Hampson cycle and right: corresponding pressure versus enthalpy diagram.

The minimum compressing power ($\dot{W}_{min}$) corresponding to a reversible and isothermal process can be calculated as the change in Gibbs free energy of the fluid during compression ('available work') [2]. Now, the maximum possible coefficient of performance (*COP*) is given by

$$COP = \frac{\dot{Q}_{gross}}{\dot{W}_{min}} = \frac{\Delta h_{warm}}{\Delta h_{warm} - T_h \Delta s_{warm}} \tag{1.2}$$

where T_h is the temperature at which the fluid enters the warm end of the CFHX and Δs_{warm} the change in specific entropy of the fluid during compression and after-cooling.

1.2 Miniature Joule-Thomson coolers

Electronic devices, such as optical detectors, low-noise amplifiers, CMOS circuitry and superconducting devices require cryogenic temperatures to reduce their thermal noise, to increase the bandwidth or to obtain superconductivity [3, 4]. In many cases, these devices only dissipate a few milliwatts while most cryogenic coolers deliver a cooling power in the range of 1 W at 80 K. To obtain cryogenic coolers that match the cooler needs of these devices more closely, various research groups around the world have investigated the miniaturization of cryogenic coolers [5–20]. Most of the research was focused on the development of small JT coolers, because these coolers do not contain moving parts in the cold stage. This makes the miniaturization of these coolers easier.

Pioneering work to produce a miniature JT cold stage by means of micro-electro-mechanical-systems (MEMS) technology was done by Little et al. [6, 7]. They produced the first miniature JT cold stage out of glass plates by using a photolithograpic fabrication process [6]. The smallest cold stage had dimensions of 15.0 x 2.0 x 0.5 mm ^{3} and cooled down to 88 K in about 45 s when operated with nitrogen. Its cooling capacity was about 25 mW.

Burger et al. combined a miniature JT cold stage to a sorption compressor and in that way produced a closed-cycle cooler system [12, 21]. The cold stage consisted of tube-in-tube heat exchangers made of glass capillaries glued to a micromachined silicon evaporator volume. The cold stage was operated with ethylene and delivered a cooling capacity of 200 mW at 170 K, while it was precooled to 238 K with a thermoelectric cooler [12].

Lerou et al. successfully developed and tested micromachined JT cold stages that were fabricated by MEMS-technology only [5, 22, 23]. These cold stages consisted of a stack of three glass wafers. The high and low-pressure lines were placed on top of one another; etched in the top and middle wafer as rectangular channels with supporting pillars. A thin, highly reflective layer of gold was sputtered on the outer surface to minimize the parasitic heat loss due to radiation. A schematic and photograph of these micromachined JT cold stages is shown in Fig. 1.2. Operated with nitrogen, net cooling powers of 10 to 20 mW at 100 K were obtained [23]. An important distinction with the work of Little et al. is that

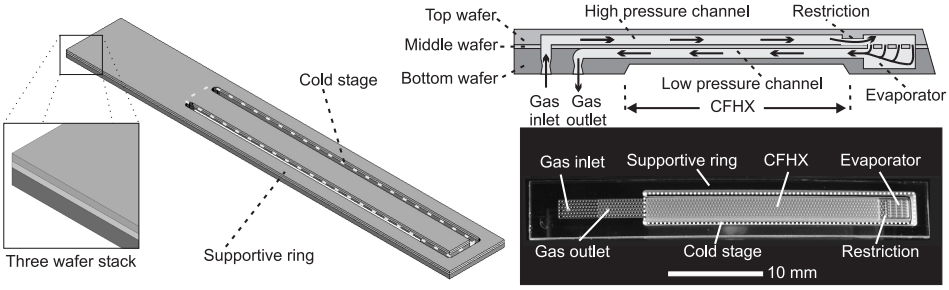

Figure 1.2: Left: schematic of a micromachined JT cold stage. Right top: schematic cross-section and right bottom: photograph of a JT cold stage. From [5].

the cold stages of Lerou et al. were optimized for maximum performance in combination with minimum size by minimizing the entropy generation [24]. This resulted roughly in doubled net cooling powers for the same input power. The smallest cold stage had dimensions of 30.0 x 2.2 x 0.7 mm^3. The JT cold stages described in this thesis are based on the design of Lerou et al.

Lin et al. developed a miniature cryogenic JT cooler for cooling a thermal detector [20, 25]. The heat exchanger was formed by six hollow-core glass fibers with an outer diameter of 125 μm placed in a fiber with a diameter of 0.61 mm and had a length of 25 mm. The CFHX was solder bonded to a silicon cold head with dimensions of 2.0 x 2.0 x 1.2 mm^3. This cold stage was operated with a five-component mixed-gas refrigerant and cooled down to 77 K. A thermoelectric cooler was used to precool the warm end to 240 K.

1.3 Motivation and research goals

Vibration-free miniature JT coolers have a high potential for future earth observation and science missions in cooling small optical detector systems [26–28]. For this application, JT cooling has several advantages above other cooling cycles. JT cooler tips do not contain moving parts and therefore can be scaled to very small sizes [5, 7]. When combined with a sorption compressor [29], a closed-cycle cooler without containing moving parts can be obtained. Such a cycle is virtually vibration free and potentially has a long life-time. Also, JT coolers lend themselves perfectly for distributed cooling in which multiple cold tips are driven by a single compressor [30]. The cold tips, each cooling an optical detector array, can be distributed over a satellite, remote from the compressor. This allows for maximum flexibility in interfacing and satellite design.

The miniaturization of JT coolers have been investigated at the University of Twente for many years. In 1995, Burger et al. started with exploring the possibility to fabricate JT cooler parts by means of MEMS-technology, resulting in a first cooler prototype in

2001 [12, 21]. In 2007, Lerou et al. finished their research to design and realize a miniature JT cold stage completely made by MEMS-technology [5, 22, 23]. The work that is described in this thesis focuses on the utilization of these micromachined JT cold stages.

The scope of the project is to obtain distributed JT microcooling of small detector systems for future space missions. This project can be divided into four main steps:

- Identify the detector systems that are suitable for cooling with a miniature JT cold stage.
- Develop a conceptual design of a JT cold stage - detector system.
- Design and test micromachined JT cold stages for cooling detector systems.
- Obtain distributed microcooling in which multiple JT cold stages are driven by a single compressor.

1.4 Outline

In this thesis, the research done to obtain distributed cooling of small detector systems used in space applications is described. The research focuses on the use of single stage micromachined JT coolers that can provide cooling within the temperature range of 65 - 250 K. To identify the detector systems that are suitable for cooling with a miniature JT cold stage, a literature survey is done. In chapter 2, the results of this survey are discussed. First, the various detector systems used in space applications are described. Then, the results of the literature survey are given and the cooler requirements of the detector systems are listed. This chapter ends with a discussion on which detector arrays are suitable for cooling by a miniature JT cold stage.

In chapter 3, the application of JT cold stages in the temperature range of 65 - 250 K is investigated. To cover this temperature range with JT cooling, various working fluids can be used. To select the most suitable working fluid for a specific temperature, an optimization study is done that is based on the thermodynamic properties of the fluids only. Furthermore, a theoretical analysis is performed to investigate whether a JT cold stage can be operated with different working fluids. To simulate the performance of a miniature JT cold stage, a thermal model is built in the software program ESATAN. This model is also discussed in this chapter.

In chapter 4, a conceptual design of a miniature JT cold stage - detector array system is discussed. This design focuses on the interface between the JT cold stage and the detector array as well as on the wiring of the array. First, various techniques for bonding a detector array to a micromachined JT cold stage are listed and the most suitable technique is selected. Then, various ways for realizing the wiring of the detector array are discussed. Chapter 4 ends with a description of the conceptual design.

Single-stage micromachined JT cold stages for cooling small detector arrays were designed and tested. In chapter 5, the results of the experiments are discussed. The temperature profiles along the length of the CFHX of various JT cold stages were measured as well as their net cooling powers. To validate the theoretical analysis done to investigate whether a JT cold stage can be operated with different working fluids, the JT cold stages were driven with both nitrogen and methane. Furthermore, the thermal model is validated with experimental data. Also, experiments done to measure the performance of the JT cold stages cooling a (dummy) electronic device are discussed.

A closed-cycle JT cooling system is built by combining a JT cold stage with a linear compressor. Because this compressor can produce only a relatively modest compression ratio, the JT cold stage was operated with a mixed-gas refrigerant. In chapter 6, an introduction to mixed-gas JT cooling is given. Also, experiments were done to measure the performance of the closed-cycle JT cooling system and the results are discussed. Furthermore, distributed JT cooling, in which multiple JT cold stages are combined with a single compressor, is described.

The thesis ends with conclusions and an outlook given in chapter 7.

CHAPTER 2

Optical detector arrays in space applications

In space-based astronomy, a wide variety of optical detector arrays are used to explore the universe. For example, the beginning of the universe, the formation of galaxies, the creation of stars and the expanding of the universe are studied with the use of detector arrays. Furthermore, the planet Earth is monitored by detecting the gas concentrations in the atmosphere, clouds, rainfall, the temperature of the oceans and so on and so fort. Many of these detector arrays require cooling for operation. A literature study is performed to investigate which types of detector arrays that are used in space-based astronomy can be cooled by a miniature JT cooler.

In this chapter, an overview of the various types of detector arrays used for the detection of optical radiation is given. Both, thermal and photon detector arrays are considered. Furthermore, the results of a literature survey among photon detector arrays offered by the major manufactures are discussed and the cooling needs of photon detector arrays are listed. This chapter ends with a selection of detector arrays that can be cooled by a miniature JT cold stage.

2.1 Detection of optical radiation

A wide variety of detector arrays exists that is sensitive to optical radiation [31–34]. This is considered as radiation ranging from the vacuum ultraviolet to the submillimeter wavelength (25 nm - 1000 μm), as shown in Table 2.1. State-of-the-art detector arrays consist of thousands to millions of pixels, each containing a detector that is integrated with its own amplifier. Large read-out integrated circuits (ROICs) convert the output of each individual pixel to a single (or a number of) electric output(s) in a multiplexing process. Most of the detectors convert optical radiation to an electrical response (e.g. current or voltage). Depending on the conversion mechanism, optical detectors can be divided into two main classes: thermal detectors and photon detectors.

In thermal detectors, incident radiation is absorbed within the detector material, changing its temperature. The change in a temperature-dependent material property, such as the resistance, generates an electrical output. The response of a thermal detector depends on the heat energy falling on the detector. In general, these detectors have a modest sensitivity and a relatively slow response compared to photon detectors, but they are cheap and easy to use [31].

Photon detectors usually are made of semiconductor material. Their operation is based on the photoelectric effect: incident photons are absorbed within the semiconductor and produce free charge carriers, which change the electrical distribution in the detector material. This results in, for example, a change in voltage or current. Photon detectors directly respond to the number of photons absorbed. They are characterized by a very high signal-to-noise performance, which can be much higher than that of thermal detectors. Furthermore, these detectors have a very fast response to a change in optical radiation. However, to achieve this, they need cryogenic cooling for detecting photons with a wavelength beyond approximately 3 μm [31].

Table 2.1: Various spectral ranges of optical radiation [31].

Spectral range	Name	Abbreviation
25-200 nm	Vacuum ultraviolet	VUV
200-400 nm	Ultraviolet	UV
400-700 nm	Visible	VIS
700-1000 nm	Near infrared	NIR
1-3 μm	Short wavelength infrared	SWIR
3-5 μm	Medium wavelength infrared	MWIR
5-14 μm	Long wavelength infrared	LWIR
14-30 μm	Very long wavelength infrared	VLWIR
30-100 μm	Far infrared	FIR
100-1000 μm	Submillimeter	Sub-mm

In many applications, photon detectors are the detectors of choice, because of their higher resolution and faster response. However, thermal detectors are often used in the wavelength range beyond 25 μm, where there is lack of suitable material for photon detectors [31, 35, 36].

2.2 Thermal detector arrays

Thermal detectors absorb incident photons and convert their optical energy into heat [31, 32]. This process changes the temperature of the detector material and thus a temperature-dependent material property, such as the resistance. This results in a change in an electrical output (i.e. current or voltage), that can be sensed by an external electric circuit. The response of a thermal detector depends on the total energy deposited by the incident photons. As long as the number of photons is adjusted to keep the absorbed energy the same, the detector response is identical to signals at any wavelength. Thus, the wavelength dependence of the response is flat and as broad as the photon-absorbing material will allow [32]. Various examples of thermal detectors are bolometers of semiconducting or superconducting materials, thermovoltaic devices such as thermocouples and thermopiles, pyroelectric detectors and thermopneumatic devices that work on basis of gas expansion, such as the Golay cell [32, 35, 37].

In space-based astronomy, in general, thermal detectors, usually in the form of bolometers, are used for detecting radiation in the Sub-mm spectral range (100 - 1000 μm) for which no good photon detector exists [35, 36]. To achieve a sufficiently low noise-level, these detectors are operated at temperatures in the order of 100 mK [36, 38, 39]. JT coolers cannot reach such low temperatures [40]. Therefore, thermal detectors are not further considered in this thesis.

2.3 Photon detector arrays

Photon detectors are usually made of semiconducting materials [31, 32]. These materials are excellent for photon detection, because their electrical properties change dramatically when a photon is absorbed. Incident radiation falling on the detector is absorbed and produces free charge carriers. These carriers change the electrical distribution within the semiconductor, which results in a change in electrical output, such as a current or voltage. Photon detectors directly respond to the number of photons absorbed. As long as the energy of a photon is higher than the bandgap energy, the photon is 'counted'. The spectral range in which photons can be detected by a certain photon detector depends on the semiconductor used [32–34]. An important temperature-dependent parameter in that respect is the cut-off wavelength, defined as the maximum wavelength at which a photon can be detected with a reasonable efficiency. This cut-off wavelength is mainly determined by the bandgap energy of the semiconductor. Semiconductors that

Table 2.2: Spectral range and operating temperature range of semiconductors that are often used for photon detection.

Semiconductor	**Spectral range** (μm)	**Temperature** (K)
Si	0.1 - 1.1	170 - 300
InSb	1 - 5	10 - 80
HgCdTe	1 - 25	30 - 160
InGaAs	0.7 - 2.5	220 - 300
AlGaAs/GaAs	4 - 12	30 - 80
Si:As	14 - 30	< 10
Ge:Ga	40 - 120	< 10

are often used for photon detection are silicon (Si), indium-antimony (InSb), mercury-cadmium-telluride (HgCdTe), indium-gallium-arsenide (InGaAs), aluminum-gallium-arsenide (AlGaAs) and Germanium (Ge). Table 2.2 presents a list of these semiconductors along with the spectral range they are sensitive for and their typical operating temperature range.

There are many different structures used in photon detectors to convert the generated electron-hole pairs into an electrical output. The most common structures are the photoconductive, photovoltaic and photoemissive structure [32, 33]. However, all photon detectors contain a region with few charge carriers and hence a high resistance. An electrical field is maintained across this region. Photons are absorbed within the semiconductor material and produce free charge carriers, which are driven across the high-resistance region by the field. The resulting current is the output of the detector. For more information about the different structures, the reader is referred to some excellent books on this topic [32, 33].

2.3.1 Architectures of photon detector arrays

Photon detectors are combined with ROICs to built large 2-dimensional detector arrays. State-of-the-art detector arrays consist of thousands to millions of detectors, called pixels, each containing a photon detector that operates at the fundamental noise limit. Large ROICs convert the output of each individual pixel to a single (or a number of) electrical output(s) in a multiplexing process. In the visible spectrum, these detector arrays are often called charge coupled devices (CCDs) or CMOS imagers; named after the silicon technique used to build the device. These arrays, often made of silicon, have a monolithic structure; the photon detectors and ROICs are integrated on a single wafer. For the UV and IR spectrum, a hybrid structure is used in which the photon detector array and ROIC are fabricated separately on different substrates and then integrated.

For the visible spectrum, CCDs were the dominant detector arrays used in space [41–43]. Their operation is based on the photoelectric effect. The generated photoelectrons are collected under an electrode in each pixel. During the read-out of the array, the stored electrons are moved simultaneously along columns to one edge of the CCD array by alternating the bias voltage levels. An output amplifier converts the electrons to a useful signal. CCDs are virtually perfect detectors. They have nearly 100% quantum efficiency (defined as the percentage of incident photons that add to the ouput signal), almost no dark current (intrinsic noise, see page 12) at 150 K and a very low read-out noise of a few electrons [43, 44]. Furthermore, very large uniform detector arrays could be built with a very high fabrication yield and a perfect signal-to-noise performance. The drawback of CCDs is the relatively low read-out speed and the dramatic charge transfer efficiency degradation under charged particle irradiation [41, 45].

CMOS imagers are upcoming detector arrays, also in space applications [41, 46, 47]. The use of standard CMOS-technology for the fabrication of these arrays offered the possibility to integrate more electronics on chip. Nowadays, most CMOS imagers contain a pixel array, signal processing electronics, an analog-to-digital converter, and timing and control electronics [47, 48]. An amplifier is integrated in each pixel. This makes them more radiant tolerant, because no electrons have to be transferred across the array before read-out. Furthermore, it is possible to address each pixel separately, resulting in a much higher read-out speed compared to CCD's. Also, the power consumption of CMOS imagers is typically an order of magnitude lower than that of CCD's [41].

Hybrid detector arrays are used for the detection of UV and IR radiation [31, 32, 49]. The photon detection takes place in an optimized detector material for the spectral range of interest. Often, the semiconducting materials InSb, HgCdTe and InGaAs are used [32, 34, 50]. The ROIC is made of silicon with CMOS technology and integrated with the detector array by flip-chip bonding [32, 50]. Nowadays, hybrid arrays are made as large as 4096 x 4096 pixels [51].

2.3.2 Operating temperature of photon detector arrays

The operating temperature of a photon detector array is determined by a combination of parameters [35]. The most important parameter is the required spectral range of the detector array application which determines the detector material that should be used (Table 2.2). Another parameter is the expected photon flux that determines the maximum noise level that the detector array is allowed to have for detecting the incident photons. The fundamental limit of performance of a detector array is reached when its noise and that of its amplifier are low compared to the photon noise and background radiation noise [34, 35]. The photon noise is caused by statistical fluctuations in the incident photon stream resulting in a fluctuation in produced electron-hole pairs and thus in a fluctuation in the output signal. This noise source can not be reduced. The background radiation noise is caused by photons from the background that fall on the detector and can

be reduced by narrowing the field of view, by observing the radiation through a narrow-band cold filter or by reducing the temperature of the background [34]. Important internal noise sources of the detector array are Johnson noise caused by the random motion of electrons in a conducting material and dark current noise due to thermally generated free charge carriers in the semiconductor. Both noise sources can be reduced by decreasing the operating temperature of the detector array.

Photon detector arrays have to be cooled to achieve the fundamental limit of performance. Detectors are said to operate in the signal fluctuation limit, when the photon noise is the limiting noise source. In practice, this limit is only achieved in some UV and VIS detectors [31]. In the IR spectrum, the background radiation noise is often larger than the photon noise. When the background radiation noise is the limiting factor for photon detection, the detector is said to operate at the BLIP limit (i.e. background limited infrared photodetector limit) [31].

2.4 Photon detector array survey

2.4.1 Overview of main photon detector arrays

To identify the photon detector arrays that can be cooled by a miniature JT cold stage, in 2010 a literature survey is done among arrays fabricated by the major manufacturers (E2V [52], Raytheon [53], Sensor Inc. [54], Sofradir [55], Teledyne [56] and XenICs [57]). The main characteristics of these arrays, such as size, spectral operating range, operating temperature, power dissipation, detectivity and wiring requirements are collected. Table 2.3 presents a list of state-of-the-art photon detector arrays made by each manufacturer and their most important characteristics. A complete list of arrays and their characteristics that are relevant for microcooling is given in Appendix A. The typical operating temperature as a function of the wavelength for various detector materials is given in Fig. 2.1.

Silicon detector arrays are widely used in the spectral range 0.2 - 1.1 μm and can even be used for detecting gamma and X-ray radiation. In space, these detector arrays are mostly used for star trackers [58], sun sensors [59], and UV and VIS astronomy [43, 60]. The first two applications are used for the position control of satellites. Sun sensors determine the attitude angle of the satellite with respect to the sun. Star trackers observe the star field and match this to a star catalog to determine the satellite's attitude. Almost any satellite has a number of these sensors on board. Till now, most silicon detector arrays flying in space are CCDs. However, also in this market, CMOS arrays are becoming more popular [49]. Typically, sun sensors do not need cooling for operation, whereas star trackers operate within the temperature range 220 - 300 K. Detector arrays used for VIS astronomy are cooled down further, but not below 150 K.

InGaAs detector arrays are sensitive for radiation in the NIR and SWIR part of the spectrum (1.0 - 2.6 μm). They find their applications in high-speed light-wave

Table 2.3: Typical state-of-the-art photon detector arrays offered by the major manufacturers in the year 2010.

Manufacturer	Detector material	Size/architecture* (pixel x pixel)	Pixel pitch (μm x μm)	Spectral range (μm)	Operating temperature (K)
E2V	Si CCD	4096 x 4096 /M	12 x 12	0.3 - 1.1	173
	Si CCD	2048 x 2048 /M	14 x 14	0.4 - 1.1	233 - 300
	Si CMOS	1415 x 1430 /M	18 x 12	0.4 - 0.9	293
Raytheon	Si PIN	2048 x 2048 /M	10 x 10	0.4 - 1.1	273 - 300
	HgCdTe	2048 x 2048 /H	20 x 20	0.85 - 2.5	70 - 80
	HgCdTe	260 x 256 /H	40 x 40	7 - 12.5	40 - 50
	InSb	2048 x 2048 /H	25 x 25	0.6 - 5.4	30
	InSb	640 x 480 /H	20 x 20	3 - 5	70 - 80
	Si:As	512 x 412 / H	30 x 30	1 - 28	4 - 10
Sensor Inc	InGaAs	320x320 /H	40 x 40	0.9 - 1.7	300
	InGaAs	1 x 256 /H	25 x 25	1 - 2.6	223
Sofradir	HgCdTe	1000 x 256 /H	30 x 30	0.8 - 2.5	< 200
	HgCdTe	1280 x 1024 /H	15 x 15	3.4 - 4.8	77 - 110
	HgCdTe	320 x 256 /H	30 x 30	7.7 - 11	70 - 90
	AlGaAs	640 x 512 /H	20 x 20	8 - 9	70 - 75
Teledyne	HgCdTe	2048 x 2048 /H	18 x 18	0.4 - 1.7	140
	HgCdTe	2048 x 2048 /H	18 x 18	0.4 - 2.5	77
	HgCdTe	2048 x 2048 /H	18 x 18	0.4 - 5.4	40
	Si PIN	1024 x 1024 /H	18 x 18	0.2 - 1.1	150 - 200
XenICs	InGaAs	640 x 512 /H	20 x 20	0.9 - 1.7	263
	InGaAs	1 x 512 /H	25 x 25	1.1 - 2.5	223
	HgCdTe	320 x 256 /H	30 x 30	0.85 - 2.5	200
	InSb	640 x 256 /H	20 x 20	3 - 5	50 - 80

* H=Hybrid, M=Monolithic

communication systems and astronomy [31, 61]. By changing the alloy composition of InGa and GaAs, the responsivity can be maximized at the desired wavelength [31]. For most applications, InGaAs detectors are operating within the temperature range 220 - 300 K [62]. However, for example for space-based spectroscopy of the Earth atmosphere and for astronomy the detector arrays are cooled to 150 K [61].

Detector arrays based on HgCdTe can be used in the wide spectral range 0.4 - 25 μm [50, 63, 64]. Their response for a particular wavelength can be optimized by changing the alloy composition of HgCd and CdTe. The high resolution at relatively high operating temperatures compared to competing arrays such as InSb arrays, quantum

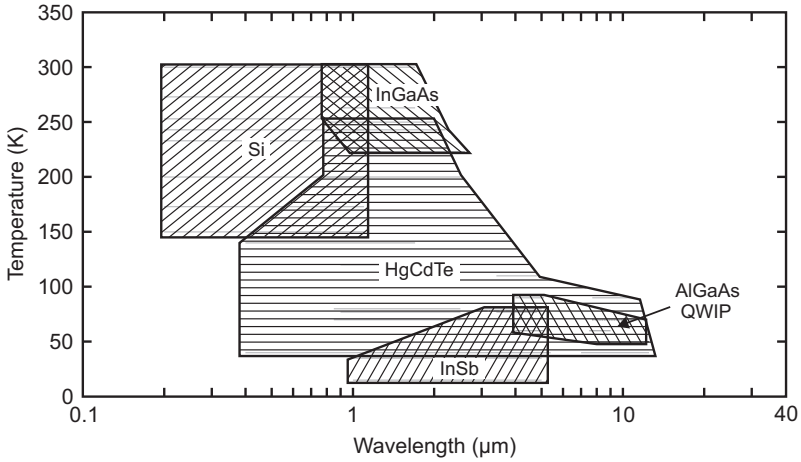

Figure 2.1: Operating temperature versus spectral range for state-of-the-art photon detector arrays offered by the major manufacturers in the year 2010.

well infrared photodetectors (QWIPs) and platinum silicon (PtSi) Schottky arrays, and the high flexibility makes HgCdTe the most popular material for infrared detector arrays. Nowadays, the largest HgCdTe detector array contains 4096 x 4096 pixels [51]. The operating temperature for HgCdTe SWIR detector arrays is about 30 - 250 K, MWIR arrays operate at 30 - 120 K, and arrays for the LWIR are cooled to about 30 - 80 K [34]. The disadvantage of HgCdTe is that it is difficult to produce large uniform arrays of this material. This results in a relatively low fabrication yield and thus expensive arrays [31, 63].

The binary compound InSb is a competing semiconductor of HgCdTe for the detection of optical radiation in the spectral range 1 - 5 µm. Despite the lower operating temperature compared to HgCdTe, InSb remains a popular material for the MWIR, because of the easier production process [34]. Large and highly-uniform arrays can be built with a high yield and thus a relatively low cost. For astronomy, InSb detector arrays of 2048 x 2048 pixels and a dark current as low as 0.01 electrons per second are built that operate at a temperature of 30 K [65]. Typically, detector arrays based on InSb operate within the temperature range 30 - 80 K.

QWIPs are alternative devices for the LWIR region (5 - 14 µm) [32, 66–68]. The advantages of these devices include the use of standard manufacturing techniques based on GaAs growth and processing technologies. The growth is highly uniform and well-controlled which results in a high yield and thus low costs. The disadvantages are the low quantum efficiency, typically less than 10%, and the narrow spectral response band compared to other detectors [31]. QWIPs typically operate at a temperature of about 40 to 80 K.

2.4.2 Cooler requirements of photon detector arrays

In Fig. 2.1, it is shown that photon detector arrays made of Si, InGaAs and HgCdTe (for the SWIR and MWIR spectrum) require an operating temperature within the range of 80 - 300 K. These arrays, in principle, can be cooled by a single-stage JT cooler that can cool down from room temperature to about 65 K [69]. Detector arrays made of InSb and QWIPs usually operate within the temperature range of 10 - 80 K and therefore can be cooled by two-stage JT coolers [69]. In this thesis, we focus on the use of single-stage JT cold stages and therefore detector arrays made of Si, InGaAs or HgCdTe can be cooled.

In appendix A, a complete list of detector arrays offered by the main manufacturers in the year 2010 and their characteristics relevant for cooling are given. This list shows that these arrays typically have the following specifications:

- An operating temperature in the range of 80 - 300 K, depending on the material used.
- A power dissipation of a few milliwatts to about 200 mW.
- 50 to 100 electrical connections to the external warm-end electronics.
- Dimensions as small as 2 x 2 mm^2 and as large as 40 x 40 mm^2.

2.5 Selection of photon detector arrays

Miniature JT cold stages typically have a cold tip with dimensions up to 10 x 10 mm^2 and a cooling power in the range of 10 - 150 mW at 100 K. The size of the cold tip limits the size of a detector array that can be cooled. Assumed that the pixel size is 15 x 15 μm^2 (which is a reasonable average pixel size of state-of-the-art arrays), detector arrays up to 512 x 512 pixels can be cooled. Arrays with more pixels will become too large, especially because also some area is needed for the integrated electronics.

The relatively low cooling power of a miniature JT cooler means that they are only suitable for cooling CMOS and hybrid detector arrays. These arrays typically have a power dissipation of a few milliwatts to about 50 mW. CCDs have a higher power dissipation in the order of 100 mW and therefore are not suitable for cooling with a miniature JT cooler. Especially, because cooling power is required for the parasitic heat loads on the cold tip, such as conduction through the wiring and radiation on the detector array. The conduction through the wiring of a detector array is a large parasitic heat load, especially because a huge amount of wiring is required. In section 4.2, it will be discussed how to minimize this heat load. The radiative heat load on top of a detector array of 10 x 10 mm^2 operating at 100 K is about 40 mW.

2.6 Conclusions

A wide variety of detector arrays exists that is sensitive for optical radiation. These arrays can be divided into two main classes: thermal detector arrays and photon detector arrays. In space-based astronomy, thermal detector arrays, such as bolometers, thermovoltaic devices and pyroelectric detectors, are used for the Sub-mm spectral range and operate at a temperature in the order of 100 mK. Therefore, this type of detector array is not suitable for cooling with a JT cooler. Photon detector arrays are used to detect radiation in the spectral range of 0.2 - 25 μm. The operating temperature of these arrays depends on the spectral range of interest and the incoming photon flux and lies within the wide range of 10 - 300 K.

Following a survey among photon detector arrays offered by the major manufacturers, it is concluded that arrays based on silicon, InGaAs and HgCdTe (sensitive for SWIR and MWIR radiation) can be cooled by single-stage JT coolers. It is difficult to give exact specifications, because that depends on various parameters, such as the amount of electric connections required and the power dissipation of the detector array. To give an indication, the detector arrays can have up to 512 x 512 pixels that correspond to an array size of about 10 x 10 mm^2 at a pixel pitch of 15 x 15 μm^2. Furthermore, the power dissipation of the detector array can be up to about 50 mW, so that cooling power is left for cooling other parasitic heat loads such as the conductive heat load through the wiring and the radiative heat load.

CHAPTER 3

Joule-Thomson cold stages

In space-based astronomy, a wide variety of detector arrays are used as discussed in chapter 2. Most of these detector arrays need cooling and the operating temperature required depends mainly on the spectral range of interest and the incoming photon flux. For example, it was shown that bolometer arrays operate typically at a temperature in the order of 100 mK, whereas silicon detector arrays operate at 150 K to 300 K. Because single-stage JT coolers can reach temperatures as low as about 65 K, we focus on the cooling of detector arrays that operate in the temperature range of 65 - 250 K.

In this chapter, the application of miniature JT cold stages within the temperature range 65 - 250 K is investigated. The fluid dynamics and heat transfer relevant for a miniature JT cold stage are discussed. To cover the temperature range of 65 - 250 K with JT cooling, different working fluids have to be used. The most suitable working fluid for a JT cold stage operating at a specific temperature is selected on basis of the thermodynamic properties of a fluid. Furthermore, a theoretical analysis is developed to investigate whether a miniature JT cold stage can be operated with different working fluids. To predict the performance of a miniature JT cold stage, a thermal model in the software program ESATAN is built.

3.1 Fluid dynamics and heat transfer

In this section, the fluid dynamics and heat transfer relevant for a miniature JT cold stage are discussed. The configuration of the JT cold stages in this thesis are based on that of Lerou et al. [5] as described in section 1.2. The discussion in this section focuses on this design.

3.1.1 Reynolds number

The Reynolds number (Re) gives an indication of the type of flow in a fluid channel. It is defined as the ratio of inertial forces to viscous forces and can be calculated by [70]

$$\mathrm{Re} = \frac{\rho_f v_f D_h}{\mu_f} \tag{3.1}$$

Here, ρ_f, v_f and μ_f are the density, the mean velocity and the dynamic viscosity of the fluid, respectively, and D_h is the hydraulic diameter of the fluid channel that can be written as

$$D_h = \frac{4A_c}{O} \tag{3.2}$$

where, A_c is the cross-sectional area and O is the perimeter of the fluid channel. The flow in a fluid channel is laminar for $\mathrm{Re} < 2300$ and turbulent for $\mathrm{Re} > 6000$. For Reynold numbers in the interval between 2300 and 6000, the flow is neither laminar nor turbulent and difficult to predict. By using $\dot{m} = \rho_f v_f A_c$ [70], the Reynolds number becomes a function of the mass-flow rate

$$\mathrm{Re} = \frac{4\dot{m}}{O\mu_f} \tag{3.3}$$

In this thesis, the miniature JT cold stages operating with nitrogen between 80 bar and 6 bar have a maximum mass-flow rate of around 17 mg/s, resulting in a maximum Reynolds number of around 700 occurring at the coldest temperature in the low-pressure channel. Therefore, the flow in a miniature JT cold stage is laminar.

3.1.2 Nusselt number

The Nusselt number (Nu) gives the ratio of convective to conductive heat transfer and is defined as [70]

$$\mathrm{Nu} = \frac{hD_h}{\lambda_f} \tag{3.4}$$

Here, h is the local heat transfer coefficient and λ_f is the thermal conductivity of the fluid. The Nusselt number is close to unity for laminar flow and for turbulent flow it lies typically within the range 100 - 1000.

In the case of fully developed laminar flow, the Nusselt number is a constant that is fully determined by the geometry of the CFHX [70]. For a uniform heat flux and a

rectangular channel the Nusselt number can be calculated as a function of the channel aspect ratio (X) [71]

$$\mathrm{Nu} = 8.235\left(1 - \frac{2.0242}{X} + \frac{3.0853}{X^2} - \frac{2.4765}{X^3} + \frac{1.0578}{X^4} - \frac{0.1861}{X^5}\right) \tag{3.5}$$

In the JT cold stages, pillars are placed in the fluid channels to withstand the high pressures [5]. Therefore, the Nusselt number should not be calculated for the full width of the channel, but instead the limited width due to the pillars should be taken into account. As an approximation, we assume the width to be the minimum distance between the pillars. This results in a different Nusselt number inside the high-pressure channel (Nu $\approx$ 4.65) and low-pressure channel (Nu $\approx$ 6.45).

3.1.3 Enthalpy flow through the fluid channels

By flowing through the CFHX, the fluid undergoes a change in enthalpy. The net change in enthalpy flow of the fluid ($d\dot{H}$) at constant pressure in a small section (dx) of the CFHX can be calculated by

$$d\dot{H} = \dot{m} c_{p,f} dT_f \tag{3.6}$$

Here, $c_{p,f}$ is the local specific heat of the fluid at constant pressure and dT_f is the local temperature difference of the fluid over a length dx in the flow direction.

3.1.4 Conductive heat flow

Conduction is the transport of heat through a solid material from a warm side to a cold side. In a miniature JT cold stage, conduction takes place in the longitudinal direction of the CFHX through the glass and the gold layer. Also, there is conduction from wafer to wafer through the pillars located in the fluid channels and from the high-pressure channel to the low-pressure channel through the middle wafer. Conductive heat flow ($\dot{Q}_{cond}$) can be calculated by the Fourier law [70] as

$$\dot{Q}_{cond} = \lambda_m A_c \frac{dT_m}{dx} \tag{3.7}$$

Here, λ_m is the thermal conductivity of the material, A_c is the cross-sectional area and dT_m is the temperature difference in the material over a small distance dx.

3.1.5 Convective heat flow

When a fluid flows through a duct, convective heat transfer takes place between the fluid and the wall of the duct. In a miniature JT cold stage, convection take place between the fluid and the channel walls, and between the fluid and the pillars. Convective heat flow

($\dot{Q}_{conv}$) from a fluid node at a temperature T_f to a material node at temperature T_m can be written as [70]

$$\dot{Q}_{conv} = hA_{hx}(T_f - T_m) \tag{3.8}$$

where, A_{hx} is the heat exchange area. The local heat transfer coefficient (h) can be determined by using Eq. 3.4.

3.1.6 Radiative heat flow

Radiation is the transfer of heat between two objects by electromagnetic waves that even takes place in a vacuum environment [70]. The net radiative heat flow ($\dot{Q}_{rad}$) from a body with outer area A_1, temperature T_1 and emissivity ε_1 that is completely enclosed by another body with inner area A_2, temperature T_2 and emissivity ε_2 can be calculated by [70]

$$\dot{Q}_{rad} = \frac{\sigma_b A_1 (T_2^4 - T_1^4)}{\frac{1}{\varepsilon_1} + \frac{A_1}{A_2}(\frac{1}{\varepsilon_2} - 1)} \tag{3.9}$$

where, σ_b is the Stefan-Boltzmann constant. In the measurement set-up, the miniature JT cold stage is surrounded by a much larger vacuum chamber ($A_2 >> A_1$). In that case, the total emissivity of the surroundings can be assumed as a black body ($\varepsilon_2 = 1$). Therefore, the radiative heat flow from the surroundings at temperature T_{env} to the JT cold stage with emissivity ε_c, temperature T_c and outer surface A_{rad} can be simplified to

$$\dot{Q}_{rad} = \varepsilon_c \sigma_b A_{rad} (T_{env}^4 - T_c^4) \tag{3.10}$$

Thus, to reduce the radiative heat flow, the emissivity of the miniature JT cold stage should be as low as possible. The emissivity of glass is around 0.8 - 0.95 [72]. Therefore, a thin layer of gold with emissivity of 0.02 [73] is sputtered on top of the outer surface of the JT cold stage.

3.2 Mass-flow rate

The mass-flow rate of a miniature JT cold stage is determined by the dimensions of the restriction that in our case consists of rectangular slits [5, 22]. Assumed that the JT expansion is adiabatic and thus isenthalpic, the mass-flow rate for fully developed, laminar, isenthalpic and viscous flow through a rectangular channel can be calculated by [70]

$$\dot{m}(H,P) = \frac{wh^3}{12l} \int_{P_l}^{P_h} \frac{\rho_f(H,P)}{\mu_f(H,P)} dP \tag{3.11}$$

where w, h and l are the width, height and length of the restriction, respectively, and P_l and P_h are the low and high pressures, respectively. Lerou et al. [5, 22] assumed that the restriction has a constant temperature equal to that of the evaporator, because

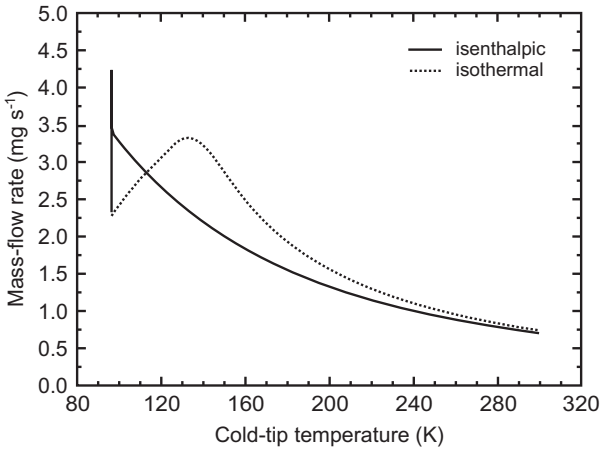

Figure 3.1: Calculated mass-flow rate versus the cold-tip temperature for a miniature JT cold stage operating with nitrogen between 80 bar and 6 bar.

the restriction is in close contact with the evaporator. In that case, the JT expansion is isothermal and for fully developed, laminar, isothermal and viscous flow through a rectangular channel the mass-flow rate can be calculated by [70]

$$\dot{m}(T,P) = \frac{wh^3}{12l}\int_{P_l}^{P_h}\frac{\rho_f(T,P)}{\mu_f(T,P)}dP \tag{3.12}$$

An example of the calculated mass-flow rate as a function of the cold-tip temperature of both methods for a miniature JT cold stage operating with nitrogen between 80 bar and 6 bar is given in Fig. 3.1. The width, height and length of the restriction were taken as 0.98 mm, 2.80 mm and 1100 nm, respectively. As shown, the mass-flow rate increases with decreasing cold-tip temperature due to the change in density and viscosity of the fluid. In the isenthalpic case, as the cold tip is at its lowest temperature, the mass-flow rate first increases and then decreases. Here, the value of the mass-flow rate depends on the temperature of the high-pressure fluid when it enters the restriction. In a miniature JT cold stage, the temperature of the high-pressure fluid can change due to the formation of two-phase fluid that flows back into the CFHX and in that way cools down the high-pressure fluid further. In the isothermal case, it is assumed that the restriction temperature is equal to that of the evaporator. Therefore, this process of increasing and decreasing mass-flow rate takes place over a temperature range, as shown in Fig. 3.1. In section 5.5, both methods to calculate the mass-flow rate will be compared with experimental data.

3.3 Optimization of the working fluid in a Joule-Thomson cold stage

The operating temperature of a JT cold stage is determined by the boiling temperature of the working fluid at the low pressure. To reach a specific temperature, multiple working fluids can often be used. The most suitable working fluid can be selected on basis of the *COP* (Eq. 1.2). However, in situations that the *COP* is almost equal for two working fluids, also a figure of merit (FOM) that determines the efficiency of heat exchange in the CFHX can be derived. This FOM depends only on the thermal properties of the working fluid. In this section, the optimization of the working fluid in a JT cold stage for the temperature range 65 - 250 K is described. Only the case of laminar flow is considered, because the flow in a miniature JT cold stage is calculated to be laminar (section 3.1.1). For the case of turbulent flow and for the optimization study in the temperature range 2 - 65 K, the reader is referred to [40].

3.3.1 Deriving a figure of merit of heat exchange

To determine the efficiency of heat exchange in a CFHX, a FOM can be derived as follows. As discussed in section 3.1.5, the convective heat flow ($\dot{Q}_w$) from the CFHX wall to the low-pressure fluid in a small section dx at position x of the CFHX (Fig. 3.2) can be expressed by [70]

$$\dot{Q}_w = hO[T_w(x) - T_{fl}(x)]dx \tag{3.13}$$

where, $T_w(x)$ and $T_{fl}(x)$ are the local temperatures at position x of the wall and of the low-pressure fluid, respectively. Using Eqs. 3.2 and 3.4, the heat transfer between the

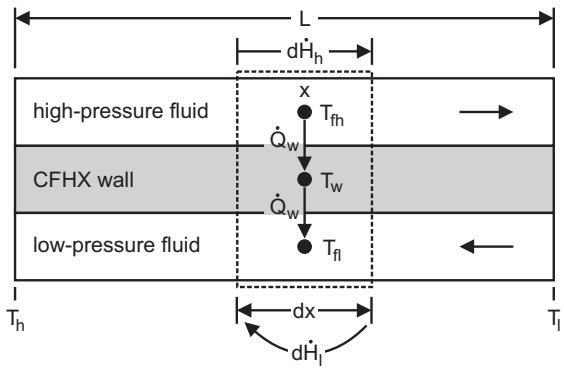

Figure 3.2: Detail of a CFHX for calculating a FOM of heat exchange.

wall and the low-pressure fluid becomes

$$\dot{Q}_w = \frac{4A_{cl}}{D_{hl}^2}\mathrm{Nu}_l\lambda_{fl}[T_w(x) - T_{fl}(x)]dx \tag{3.14}$$

where, the subscript l refers to the low-pressure fluid properties. For a perfect CFHX, the change in enthalpy flow of the low-pressure fluid (Eq. 3.6) equals the heat flow between the CFHX wall and the low-pressure fluid (Eq. 3.14), thus

$$\dot{m}_l c_{p,fl} dT_{fl} = \frac{4A_{cl}}{D_{hl}^2}\mathrm{Nu}_l\lambda_{fl}[T_w(x) - T_{fl}(x)]dx \tag{3.15}$$

Furthermore, for a perfect CFHX, the change in enthalpy flow of the low-pressure fluid equals that of the high-pressure fluid. In the stationary case, the mass-flow rates at both sides are equal and one can write

$$c_{p,fh}[T_{fh}(0) - T_{fh}(x)] = c_{p,fl}[T_{fl}(0) - T_{fl}(x)] \tag{3.16}$$

where, the subscript h refers to the high-pressure fluid properties and $T_{fh}(0)$ and $T_{fl}(0)$ are the warm-end high pressure and low-pressure fluid temperatures, respectively. From Eq. 3.16 follows that

$$T_{fh}(x) = T_{fh}(0) - \frac{c_{p,fl}}{c_{p,fh}}[T_{fl}(0) - T_{fl}(x)] \tag{3.17}$$

We define the wall temperature node to be in between the two fluid temperatures as

$$T_w(x) = \frac{1}{2}[T_{fh}(x) + T_{fl}(x)] \tag{3.18}$$

Substituting Eq. 3.17 in Eq. 3.18 and the result in Eq. 3.15 gives

$$\dot{m}_l c_{p,fl} dT_{fl} = \frac{2A_{cl}}{D_{hl}^2}\mathrm{Nu}_l\lambda_{fl}\left[[T_{fh}(0) - T_{fl}(x)] - \frac{c_{p,fl}}{c_{p,fh}}[T_{fl}(0) - T_{fl}(x)]\right]dx \tag{3.19}$$

By putting all temperature dependent terms on one side, integration over the length L of the CFHX, under constant pressure, results in

$$L = \frac{\dot{m}_l D_{hl}^2}{2A_{cl}}\int_{T_l}^{T_h} \frac{1}{([T_{fh}(0) - T_{fl}(x)] - \frac{c_{p,fl}}{c_{p,fh}}[T_{fl}(0) - T_{fl}(x)])}\frac{c_{p,fl}}{\mathrm{Nu}_l\lambda_{fl}}dT_{fl} \tag{3.20}$$

Here, T_h and T_l are the low-pressure line temperatures at the warm and cold ends of the CFHX, respectively. In the case of laminar flow, the Nusselt number is a constant, which is fully determined by the geometry of the CFHX (section 3.1.2). Then, Eq. 3.20 indicates that, the higher the thermal conductivity of the fluid and the smaller its specific heat, the more effective is the heat exchange in the CFHX and, as a result, the shorter the CFHX can be. To investigate the impact of the specific heat and the thermal conductivity of a

working fluid on the heat exchange in the CFHX, a FOM with dimension W m^{-1} in the case of laminar flow can be derived from Eq. 3.20 as the ratio of cooling power to the length of the CFHX

$$FOM = -\Delta h_{warm} \left[\int_{T_l}^{T_h} \frac{1}{[T_{fh}(0) - T_{fl}(x)] - \frac{c_{p,fl}}{c_{p,fh}}[T_{fl}(0) - T_{fl}(x)]} \frac{c_{p,fl}}{\lambda_{fl}} dT_{fl} \right]^{-1} \quad (3.21)$$

Except for a geometry factor, the reciprocal value FOM^{-1} represents the length needed for the CFHX in order to achieve a certain cooling power. The higher the FOM, the shorter the CFHX can be.

3.3.2 Optimization method

The working fluid in a JT cold stage, at a specific operating temperature, is optimized on basis of the COP as defined in Eq. 1.2. If the COP values for various working fluids are almost equal, the FOM (Eq. 3.21) is taken into account. In this way, the most suitable working fluid is selected on the basis of these parameters. The constraints used in the analysis are discussed below.

Temperature at the warm end

It is assumed that the temperature at the warm end of the JT cold stage is 300 K. In section 3.3.4, the influence of decreasing the warm-end temperature on the selection of the most suitable working fluid is investigated.

Low-pressure range

The low pressure determines the boiling temperature of a working fluid and thus the cold-tip temperature of a JT cold stage. The cold-tip temperature of the JT cold stage can only be varied within a limited range by varying this low pressure. If this pressure is set too low, the pressure drop along the low-pressure channel of the CFHX may have negative effects on the stability of the low pressure and thus on the stability of the cold-tip temperature. If the cold stage is driven by a sorption compressor, some limits are also imposed on the value of the low pressure [29]. As a result, the low pressure is selected to be between 0.2 bar and 10.0 bar.

High-pressure range

The minimum high pressure is set at 1 bar, provided it remains higher than the low pressure of the cycle in every case. The maximum high pressure is set equal to the pressure of a standard 50 L gas bottle, which is 200 bar.

Counter-flow heat exchanger

It is assumed that the CFHX is ideal and thus Eqs. 1.2 and 3.21 can be used to calculate the *COP* and the *FOM*, respectively. The fact that in practice the CFHX will not be ideal does not play a role in the selection of the most suitable working fluid. The *COP* yields the maximum attainable efficiency and the *FOM* indicates the minimum length of the CFHX required to achieve that efficiency.

Cooling power

In this analysis, the cooling power of the JT cold stage is set at 100 mW. However, the chosen cooling power does not play a role in the selection of the most suitable working fluid. For a given enthalpy change at the warm end of the system, the required cooling power determines the mass-flow rate. Since, in this ideal case, the input power to the cold stage scales linearly with the mass-flow rate, the *COP* is independent of flow and thus of the required cooling power. Also, the *FOM* is fully determined by fluid properties and by temperature and pressure boundary conditions. Thus, it is concluded that the cooling power does not play a part in the selection of the most suitable working fluid.

Operating temperature range of working fluids

Because the operating temperature is determined by the low pressure that can only be varied within a limited range, a variety of working fluids will have to be used to cover the complete temperature range between 65 K and 250 K. The temperature range in which a fluid can be used depends on the selected low-pressure range and for the most common pure fluids it is shown in Fig. 3.3. The minimum temperature is calculated for a low pressure of 0.2 bar, except for those fluids that have a triple-point pressure above 0.2 bar. For such fluids, the triple-point pressure is used for evaluating the minimum attainable temperature. The maximum temperature corresponds to a pressure of 10 bar.

3.3.3 Optimization results

In this section, the optimization analysis of the working fluid in a JT cold stage is discussed. All fluid properties were taken from Refprop [74]. The most common pure working fluids that can be used in a JT cold stage to reach a temperature within the range 65 - 250 K are listed in Fig. 3.3. The *COP* is calculated as a function of the high pressure, and for the three cases of operating temperatures of 100 K, 180 K and 250 K the results are shown in Fig. 3.4. At low operating temperatures, the *COP* of a JT cold stage is rather poor (Fig. 3.4a). In that case, the fluid is compressed at a temperature far above its critical temperature, where it will behave as essentially an ideal gas. This means that only small changes in its specific enthalpy can be obtained during compression, which results in a rather low *COP*. A fluid at a temperature close to its critical temperature behaves

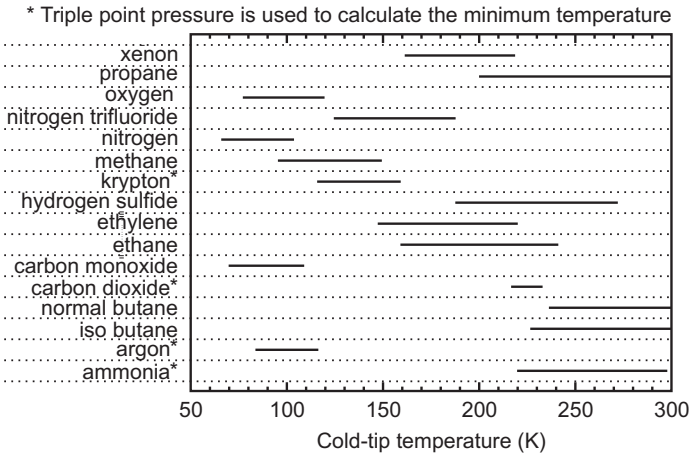

Figure 3.3: Operating temperature range in which a fluid can be used for a JT cold stage corresponding to a low-pressure range of 0.2 - 10.0 bar.

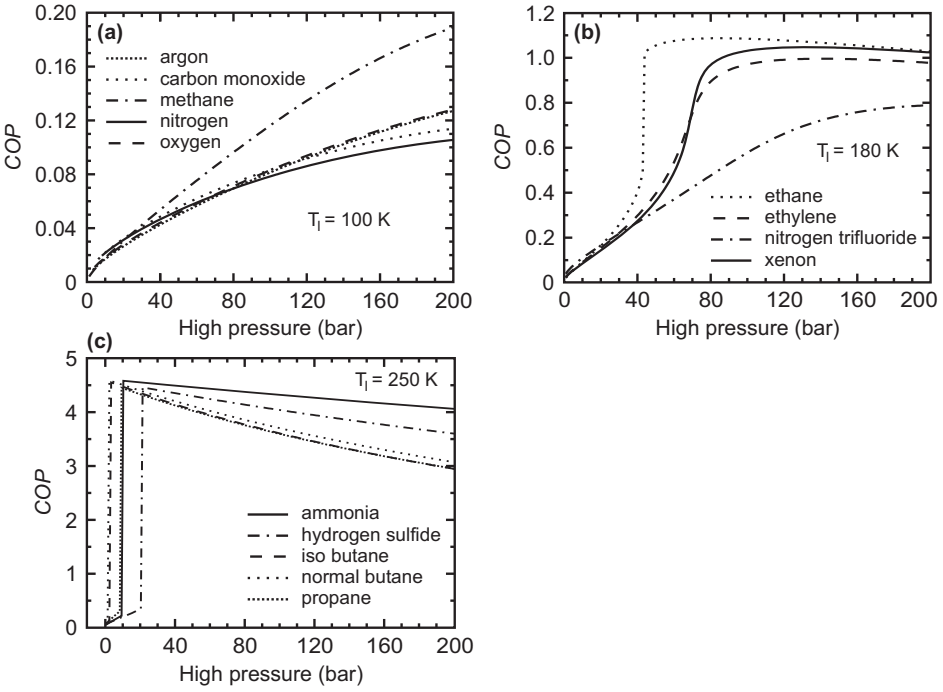

Figure 3.4: *COP* as a function of the high pressure for a cold-tip temperature of (a) 100 K, (b) 180 K and (c) 250 K.

highly non-ideal. Once in that region the fluid is compressed a much higher change in its specific enthalpy can be obtained. This explains the steep increase in *COP* of some fluids at a specific high pressure shown in Fig. 3.4b. For example, nitrogen trifluoride behaves as an ideal gas during compression, whereas the other three fluids behave highly non-ideal. Furthermore, fluids which have a critical temperature above 300 K may liquefy during compression, which causes an even steeper increase in *COP*. This is the case for all fluids shown in Fig. 3.4c.

The FOM of each fluid is calculated for the optimum high pressure, defined as the pressure for which the *COP* is highest. The parameters at maximum *COP* are shown in Table 3.1. Now, for each of the operating temperatures, the most suitable working fluid is selected on the basis of the *COP* and the FOM. For an operating temperature of 100 K, it is clear that methane can best be used as the working fluid. The *COP* and the FOM is highest for this fluid. At a cold-tip temperature of 180 K, the *COP* values of ethane, ethylene and xenon lie within 10% of each other. However, the FOM of xenon is much lower than that of ethane and ethylene. Thus, xenon is not selected. The $FOMs$ of ethylene and ethane are almost equal. Besides that ethane has a slightly higher *COP* and FOM, for this fluid also a lower high pressure is needed to reach the maximum *COP*.

Table 3.1: Maximum-*COP* parameters for a JT cold stage which has a warm-end temperature of 300 K and operates at (a) 100 K, (b) 180 K and (c) 250 K.

Fluid	**Low pressure** (bar)	**High pressure** (bar)	***COP*** (-)	***FOM*** (W m^{-1})
(a) T_l = 100 K				
Argon	3.24	200	0.13	0.049
Carbon monoxide	5.44	200	0.11	0.029
Methane	0.34	200	0.19	0.130
Nitrogen	7.78	200	0.10	0.022
Oxygen	2.54	200	0.13	0.044
(b) T_l = 180 K				
Ethane	0.79	85	1.09	0.274
Ethylene	1.82	141	1.00	0.273
Nitrogen trifluoride	7.25	200	0.79	0.115
Xenon	2.22	132	1.05	0.184
(c) T_l = 250 K				
Ammonia	1.65	11	4.72	0.989
Iso butane	0.63	4	4.69	0.145
Normal butane	0.39	3	4.73	0.148
Hydrogen sulfide	4.89	22	4.59	0.512
Propane	2.18	10	4.58	0.193

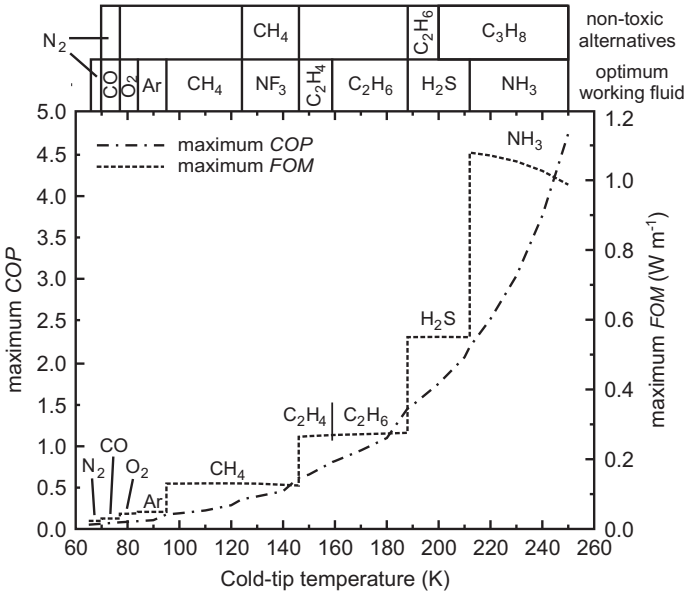

Figure 3.5: Maximum *COP* and *FOM* as a function of the cold-tip temperature.

This is a big advantage in closed-cycle cooling. Therefore, ethane will be selected as the most suitable working fluid. In Fig. 3.4c it is shown that, for a JT cold stage operating at 250 K, the maximum *COP* of all working fluids is almost equal. However, the *FOM* of ammonia is about two times higher than that of hydrogen sulfide and about seven times higher than that of the other fluids under comparison. This is caused by the large heat of condensation of ammonia, which is an order higher than that of the other working fluids [74]. This means that Δh_{warm} is much higher, resulting in a shorter length required for the CFHX (Eq. 3.21). Ammonia is thus selected as the most suitable working fluid at 250 K.

These calculations and considerations can be made for each arbitrary cold-tip temperature. In this way, the wide temperature range 65 - 250 K can be divided into several small ranges, and in each range a specific working fluid can be selected. In Fig. 3.5, the maximum *COP* and *FOM* are given as a function of the cold-tip temperature. As shown in Fig. 3.5, the most suitable working fluids in a small temperature range are nitrogen (65 - 70 K), carbon monoxide (70 - 77 K), oxygen (77 - 83 K), argon (83 - 95 K), methane (95 - 124 K), nitrogen trifluoride (124 - 146 K), ethylene (146 - 159 K), ethane (159 - 188 K), hydrogen sulfide (188 - 212 K) and ammonia (212 - 250 K). As could be expected, the maximum *COP* increases for an increasing cold-tip temperature. The *FOM* also increases, but remarkable are the levels of almost constant *FOM* within a small temperature range of the cold tip. In this temperature range, the *FOM* is determined by a single working fluid. The ratio of thermal conductivity to specific heat is rather constant

within that temperature range. As indicated by Eq. 3.21, this leads to a constant FOM.

In specific temperature ranges, carbon monoxide, nitrogen trifluoride, hydrogen sulfide and ammonia are selected as the most suitable working fluids. However, these fluids have the disadvantage that they are very toxic [75] and thus specific safety precautions have to be taken when using these fluids. Therefore, non-toxic alternatives to these fluids are also suggested in Fig. 3.5.

3.3.4 Discussion on optimization results

In this section, the influence of the constraints (defined in section 3.3.2) on the selection of the most suitable working fluid is discussed.

Warm-end temperature

Precooling of a JT cold stage can be beneficial, because then Δh_{warm} increases and thus also the COP (Eq. 1.2) [76]. Precooling is useful when the reduction of the input power of the compressor is greater than the input power required for the precooler. To investigate the effect of decreasing the warm-end temperature on the selection of the working fluid, the maximum COP and FOM are calculated as a function of this temperature. To facilitate a better comparison between the curves, the COP is normalized to the Carnot efficiency ($COP_{carnot} = T_l/(T_h - T_l)$). Fig. 3.6 shows the COP and the FOM as a function of the warm-end temperature for cold-tip temperatures of 100 K and 180 K, respectively. From this figure, it is concluded that the maximum COP increases for a decreasing warm-end temperature, which is as expected. In general, the FOM first increases and then decreases with a decreasing warm-end temperature. Furthermore, it is shown that, although the values of the COP and the FOM change, the selection of the most suitable working fluid is not affected by the warm-end temperature.

High pressure

In this analysis, the maximum high pressure was set at 200 bar. It is very difficult to produce such high pressures by means of closed-cycle compression. This means that the maximum attainable high pressure in that case will be lower. This especially affects the maximum COP of a JT cold stage operating at a temperature below 200 K. For such temperatures, the maximum attainable COP decreases. However, this will not change the selection of working fluid, because the COP of the selected working fluid is, in most cases, highest for the complete high-pressure range.

Low pressure

The temperature range within which a working fluid can be used depends on the selected low pressure. In this analysis, a low-pressure range of 0.2 - 10.0 bar is selected. If a higher

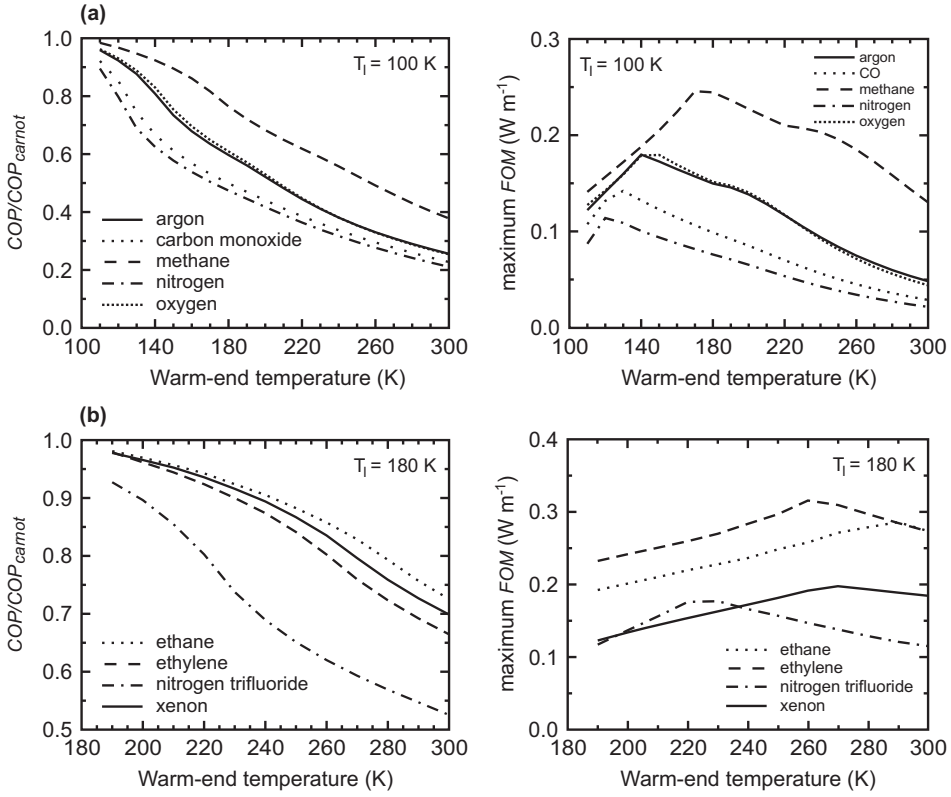

Figure 3.6: Maximum *COP* and *FOM* as a function of the warm-end temperature for a cold-tip temperature of (a) 100 K and (b) 180 K. The *COP* is normalized to the Carnot efficiency.

upper limit is selected, the maximum operating temperature for which a working fluid can be used will increase. However, in none of the cases is a fluid most suitable all the way up to the top of its operating range. At higher values of the low pressure, another fluid operating at a lower value of the low-pressure appears to perform better. So, choosing the low pressure to be above 10 bar will not affect the fluid selection. Changing the lower boundary of the low pressure affects the lowest temperature that can be achieved using a specific fluid. Changing that boundary, therefore, affects the transition temperature from one optimum fluid to the next. For instance, if the low pressure is reduced from 0.2 bar to 0.1 bar, the transition of carbon monoxide to oxygen reduces form 77.1 K to 72.7 K.

3.4 Application of JT cold stages in a wide temperature range

For cooling small detector arrays, we focus on the use of miniature JT cold stages that operate within the range of 65 - 250 K. In the previous section, the most suitable working fluid for a specific temperature range was selected. It was shown that different working fluids have to be used to cover this temperature range. To investigate whether a specific miniature JT cold stage can be operated with various working fluids a theoretical analysis based on the critical elements of a JT cold stage is performed. This analysis is discussed in this section.

3.4.1 Analysis

Critical elements of a JT cold stage in terms of its thermodynamic performance are the CFHX and the flow restriction. The CFHX should have enough contact area to efficiently exchange the enthalpy between the high pressure and low-pressure fluids. The dimensions of the flow restriction determine the mass-flow rate (section 3.2), which linearly relates to the cooling power (Eq. 1.1). The cooling power should be high enough to cool down the cold stage.

Eq. 3.20 gives a measure of the length needed for a CFHX. From this equation, we can derive a FOM_{area} that gives a measure of the area needed for a CFHX based on thermodynamic fluid properties only. In the case of laminar flow, where the Nusselt number is a constant, the FOM_{area} is given by

$$FOM_{area} = \dot{m} \int_{T_l}^{T_h} \frac{1}{([T_{fh}(0) - T_{fl}(x)] - \frac{c_{p,fl}}{c_{p,fh}}[T_{fl}(0) - T_{fl}(x)])} \frac{c_{p,fl}}{\lambda_{fl}} dT_{fl} \tag{3.22}$$

The FOM_{area} has dimension (m) and can be interpreted as the area per unit of length of the CFHX that is required to exchange all enthalpy between the high pressure and low-pressure fluids. This means that, when a JT cold stage is optimized for a certain fluid and the FOM_{area} of another fluid is lower, then the CFHX is large enough for operating with that other fluid. Here, it is assumed that the efficiency of the CFHX has to be equal for both working fluids.

In addition to a sufficiently large CFHX area, also the cooling power needs to be high enough for cooling down the cold stage. In section 3.2, it is shown that during the cool-down phase, the mass-flow rate is not a constant, but a function of the restriction temperature. This means that the gross cooling power of the cold stage changes during cool down and it, therefore, should be compared for both fluids as a function of the cold-tip temperature. If, compared to an optimized and operating cold stage, another fluid is considered, and that fluid yields a higher cooling power, then that power should be adequate to cool down the cold stage. This statement is under assumption that at each cold-tip temperature the parasitic heat losses are equal for both working fluids.

3.4.2 Analysis results

To investigate whether a miniature JT cold stage that is optimized for operating with nitrogen can be driven by other working fluids, the analysis described in section 3.4.1 was performed. This is done for a JT cold stage with a restriction length, width and height of respectively 2.8 mm, 0.98 mm and 1100 nm that is introduced in chapter 5 as low cooling-power JT cold stage.

The gross cooling power as a function of the cold-tip temperature and the FOM_{area} were calculated for the fluids nitrogen and methane. For nitrogen, this is done for a high pressure of 85 bar and a low pressure of 6 bar, for which the cold stage still cools down. For methane, the choice of the low pressure is arbitrary, but taken as 4 bar, resulting in an operating temperature of the cold stage of around 132 K. The calculations are done for various values of the high pressure and the results are given in Fig. 3.7 and Table 3.2.

Fig. 3.7 shows that the cold stage operated with methane at a high pressure above 50 bar has a comparative or larger gross cooling power than that of nitrogen in the full temperature range. In that case, the cold stage most probably will cool down. In Table 3.2, it is shown that the FOM_{area} of methane is smaller for the given high pressures, implying that the CFHX are is adequate. There will be a maximum high pressure for which the FOM_{area} is equal for both working fluids. An even higher pressure will result in a less efficient CFHX, but most probably the cold stage will still work due to the high gross cooling power. From this analysis, we can conclude that methane at a high pressure above 50 bar can be used to drive the specific cold stage

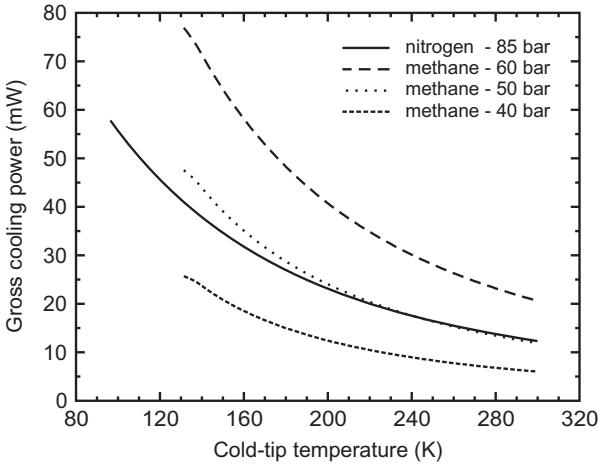

Figure 3.7: Results of the comparison of nitrogen and methane for the low cooling-power JT cold stage. The calculated gross cooling power as a function of the cold-tip temperature of both working fluids is shown. For nitrogen the cold stage is operating between 6 and 85 bar, and for methane between 4 bar and various high pressures, which are indicated in the figure.

Table 3.2: Results of the analysis of methane versus nitrogen in the low cooling-power JT cold stage

	High pressure (bar)	**Low pressure** (bar)	**Cold-tip temperature** (K)	**Mass-flow rate** (mg s^{-1})	FOM_{area} (m)	**Gross cooling power** (mW)
nitrogen	85	6	96.4	3.70	8.6	58
methane	60	4	131.4	1.38	3.9	77
methane	50	4	131.4	1.04	3.5	48
methane	40	4	131.4	0.72	3.1	26

These calculations and considerations can be made for each arbitrary working fluid. We performed this analysis for the optimum working fluids carbon monoxide, oxygen, ethylene, ethane, ammonia and propane. The results showed that this specific (low cooling-power) cold stage can be operated with these working fluids.

3.5 Thermal model of a JT cold stage in ESATAN

To predict the performance of a miniature JT cold stage, a thermal mathematical model (TMM) is built in the software program ESATAN [77]. ESATAN is a program that obtains solutions to lumped parameter thermal models. In a lumped parameter model, a continuous medium is modeled as a discrete network of nodes representing the capacitance of the system, linked by conductors representing the heat exchange between the nodes. ESATAN has facilities for dealing with conductive, convective and radiative heat transfer as well as with enthalpy flows caused by a fluid flow through a pipe.

A schematic of a miniature JT cold stage is shown in Fig. 3.8 and a schematic representation of the TMM is given in Fig. 3.9. In the TMM, the CFHX and the evaporator were separated from each other. As shown in Fig. 3.8, the CFHX is taken as the part of the cold stage between an indium seal and the restriction. The indium seal is used to make leak-tight connections between the fluid tubes and the fluid inlet and outlet of the cold stage. To simulate the CFHX, it is divided into N elements along its length. Each element consist of five sub-elements, representing the high-pressure fluid, the low-pressure fluid, the top wafer, the middle wafer and the bottom wafer. The pillars in the fluid channels are divided in half and their capacity and the convective heat flow from the fluid to the pillars is added half to the wafer above and half to the wafer below the channel. Each sub-element is represented by a node with corresponding capacitance and linked to another node by a conductive, a convective, a radiative or an enthalpy flow conductor, as shown in Fig. 3.9.

The evaporator is simulated by two nodes. The first node represents the fluid directly

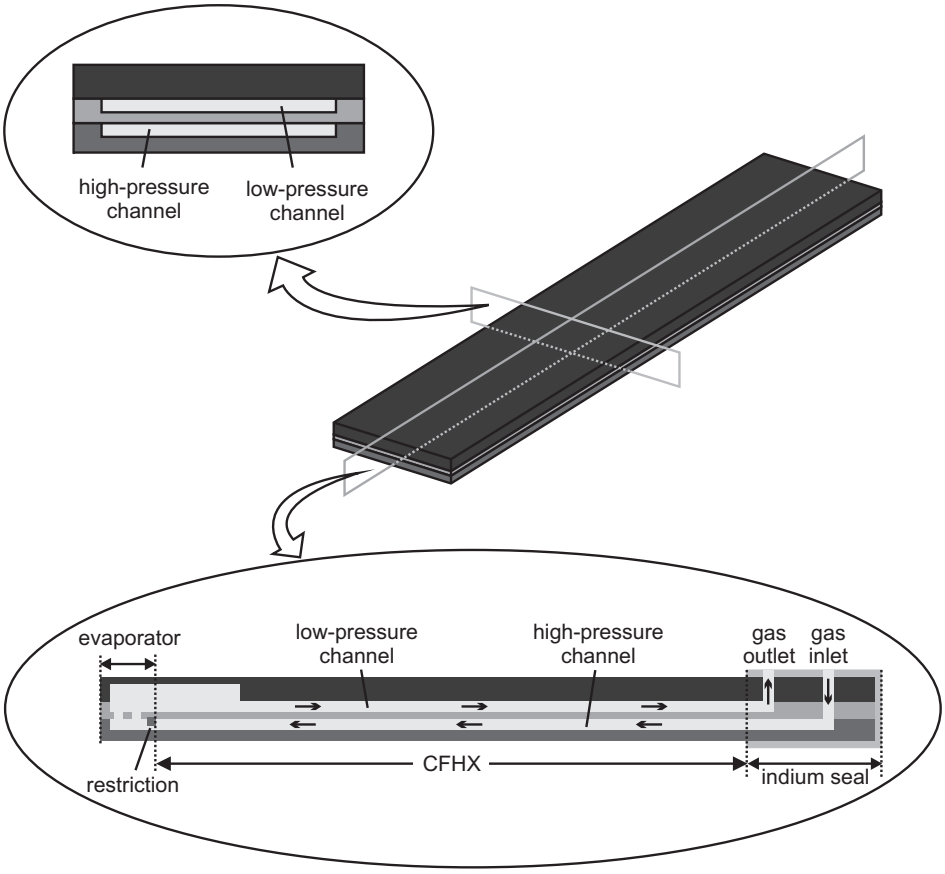

Figure 3.8: Schematic of a miniature JT cold stage.

after expansion. This node has a boundary temperature that is based on the enthalpy of the fluid during isenthalpic expansion and the low pressure. In time, its temperature changes as the enthalpy of the fluid changes. The second node represents the fluid in and the material of the evaporator. An enthalpy flow conductor is used between the first and second nodes. As shown in Fig. 3.9, this evaporator node is connected to the CFHX nodes by various flow conductors. The evaporator and low-pressure fluid are linked by an enthalpy flow conductor. Conductive flow conductors are used between the evaporator and the three material wafers. Furthermore, radiative heat flow from the surroundings to the evaporator is taken into account.

Various boundary conditions on temperature are defined. In Fig. 3.9, the nodes that have a boundary condition on temperature are indicated with a letter B. The environment of the miniature JT cold stage is assumed to be at a constant temperature and thus can

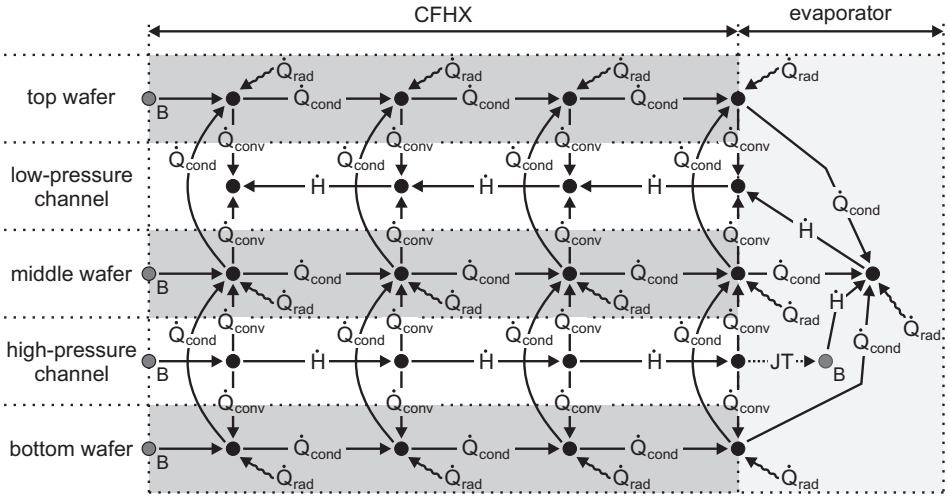

Figure 3.9: Representation of the thermal mathematical model in ESATAN.

be modeled as a single node at a temperature T_{env}. Also, at the warm end of the CFHX, the indium seal, used to make leak-tight fluid connections, connects the JT cold stage to a large heat sink. Therefore, at the warm end the temperature of the material and of the incoming high-pressure fluid are fixed at the environmental temperature. As discussed above, also the first node in the evaporator has a boundary condition on temperature.

In the model, all fluid properties depend on temperature and pressure and are taken from Refprop [74], and the material properties depend on temperature and are taken from Cryocomp [78]. In appendix B, the fluid properties of nitrogen and methane and the glass properties are given. For each node, a differential equation can be derived that contains all energy flows to this node and its capacitance. Solving all the differential equations for a small time step gives the temperature of all nodes in time. In that way, the performance of a miniature JT cold stage in time can be simulated. The cool-down time can be determined by plotting the evaporator temperature versus time. The net cooling power ($\dot{Q}_{net}$) of the JT cold stage can be calculated by

$$\dot{Q}_{net} = \dot{m}(h_{Ph,in} - h_{Pl,out}) - \sum \dot{Q}_{rad} - \sum \dot{Q}_{loss,warm} - \sum \dot{Q}_{exp} \tag{3.23}$$

Here, $h_{Ph,in}$ and $h_{Pl,out}$ are the specific enthalpy of the high-pressure fluid and low-pressure fluid at the warm end, respectively, $\sum \dot{Q}_{rad}$ is the total radiative heat load on the outer surface of the cold stage, $\sum \dot{Q}_{loss,warm}$ is the heat loss due to heat flow from the environment to the first material node induced by the conduction through the CFHX material and $\sum \dot{Q}_{exp}$ represents all the heat losses induced by the experimental characterization, such as the conductive heat flow through the wiring of the temperature sensors. The first term in Eq. 3.23 represents the cooling power of the cold stage after the

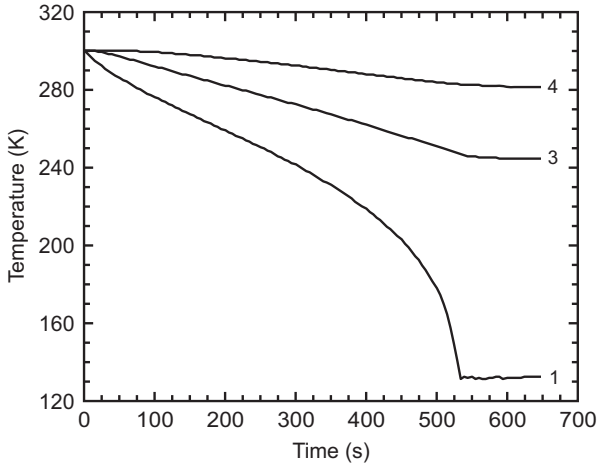

Figure 3.10: Simulated cool down of three temperature sensors as a function of the time for the low cooling-power JT cold stage operating with methane between a high pressure of 65 bar and a low pressure of 4 bar. In Table 5.2 and Fig. 5.3, the locations of the sensors on the JT cold stage are given.

heat losses due to inefficiency of the CFHX are subtracted and is a result of the model calculations.

As example, a cool down of a JT cold stage operating with methane between a high pressure of 65 bar and a low pressure of 4 bar is simulated. As is the case during the characterization experiments discussed in chapter 5, it is assumed that three temperature sensors are glued on top of the low-pressure side of the CFHX. The electrical connections from these sensors to the warm-end are made with aluminum bond wires with a diameter of 25 μm. The calculated temperatures of the various sensors as a function of the time are given in Fig. 3.10. As shown, the calculated cool-down time is 535 s. The calculated net cooling power is 96 mW. The simulation parameters and all calculated heat losses are summarized in Table 3.3. In section 5.6, the thermal model is validated with experimental data.

Table 3.3: Summary of the calculated heat losses for a JT cold stage operating with methane between a high pressure of 65 bar and a low pressure of 4 bar.

Cool-down time (s)	**Mass-flow rate** (mg s^{-1})	$\dot{Q}_{net}$ (mW)	$\dot{m}(h_{Ph,in} - h_{Pl,out})$ (mW)	$\sum \dot{Q}_{rad}$ (mW)	$\sum \dot{Q}_{loss,warm}$ (mW)	$\sum \dot{Q}_{exp}$ (mW)
535	1.8	96	113	9	0.7	7

3.6 Conclusions

In this chapter, the application of miniature JT cold stages within the temperature range of 65 - 250 K is investigated. The most suitable working fluid for a JT cold stage operating at a specific temperature in the range of 65 - 250 K is selected on basis of the *COP*, defined as the ratio of gross cooling power to the change in Gibbs free energy of the fluid during compression. In addition, a FOM is evaluated that is a measure for the efficiency of heat exchange in the CFHX. The larger the FOM, the shorter the CFHX can be. The most suitable working fluids in a small temperature range are nitrogen (65 - 70 K), carbon monoxide (70 - 77 K), oxygen (77 - 84 K), argon (84 - 95 K), methane (95 - 124 K), nitrogen trifluoride (124 - 146 K), ethylene (146 - 159 K), ethane (159 - 188 K), hydrogen sulfide (188 - 212 K) and ammonia (212 - 250 K). The non-toxic alternatives nitrogen (70 - 77 K), methane (124 - 146 K), ethane (188 - 200 K) and propane (200 - 250 K) were suggested for the toxic working fluids. Furthermore, the warm-end temperature and the maximum attainable high pressure do not play a role in the selection of the most suitable working fluid.

A theoretical analysis is developed to investigate whether a JT cold stage can be driven by different working fluids. This analysis is based on the critical elements of a JT cold stage in terms of its thermodynamic performance which are the CFHX and the flow restriction. The analysis is performed for a JT cold stage that operates with nitrogen between a high pressure of 85 bar and a low pressure of 6 bar and has a mass-flow rate of 3.7 mg s^{-1}. It is concluded that this JT cold stage can be operated with the most suitable working fluids listed above and thus is applicable in the temperature range 65 - 250 K. To predict the performance of a JT cold stage, a thermal model is built in the software program ESATAN.

CHAPTER 4

Conceptual design

Single-stage miniature JT coolers can provide cooling in the temperature range of 65 - 300 K. As discussed in chapter 2, this makes them suitable for cooling photon detector arrays made of silicon, InGaAs and HgCdTe (for the SWIR and MWIR spectrum) that typically require an operating temperature in this range. Because miniature JT coolers have a relatively low cooling capacity compared to other cryogenic coolers, the parasitic heat load to the cold tip should be minimized. A large part of this heat load is caused by conduction through the wiring of the detector array. Therefore, the design of a JT cold stage - detector array system should be optimized.

A conceptual design of a miniature JT cold stage integrated with a detector array is made. This design focuses on the interface between the cold stage and the detector array, and on the wiring of the detector array. In this chapter, various techniques are listed that can be used for bonding a detector array to a JT cold stage and the most suitable technique is selected. Furthermore, various ways for realizing the wiring of the detector array are discussed. At the end, a description of the conceptual design is given.

4.1 Interface between a miniature Joule-Thomson cold stage and a detector array

Monolithic CMOS detector arrays are usually made on a silicon wafer. In hybrid arrays, the detector array and ROIC are fabricated separately from each other on different substrates and then flip-chip bonded [32]. Usually, the ROIC is structured on a silicon wafer. This means that both CMOS and hybrid detector arrays have a silicon interface on the backside that should be bonded to the JT cold stage. The JT cold stage is made of borosilicate glass D263 T [79]. Very thin wafers (up to 30 μm thick) of this glass are available. Furthermore, it is possible to use anodic or fusion bonding on both sides of the wafer. These techniques are used in the fabrication process of the JT cold stages. Both properties make this type of glass very suitable for the production of miniature JT cold stages.

To integrate a detector chip with a JT cold stage, a silicon-to-D263 T glass bond has to be formed. A literature survey is done to find existing techniques for making such a bond. An overview of these techniques is given in the first section. In the second section, the suitable techniques are selected. The suitable techniques are experimentally tested and the results are discussed in the third section.

4.1.1 Overview of silicon-to-glass bonding techniques

Various techniques exist for making a silicon-to-glass bond. These techniques can be divided into two groups. The first group consists of techniques that do not use an intermediate layer to make the bond, such as fusion and anodic bonding. The second group contains techniques that use an intermediate layer to make the bond. Examples are solder bonding, eutectic bonding, low-temperature glass bonding and bonding by adhesives. The various techniques are now briefly discussed.

Direct or fusion bonding is a standard technique used in MEMS-technology [80–82] and is mostly used for the bonding of two silicon wafers. However, it can also be used to bond glass to glass [80], silicon to glass [83, 84], silicon to indium phosphorus (InP) [85] and silicon to GaAs [85]. In the fusion bonding process, two very clean and extremely flat wafers are brought into close contact. By doing so, the wafers will stick together due to the van der Waals forces. This process results in a rather weak bond. To increase the bond strength, the wafers are annealed at a temperature in the range of 600 - 1200 °C. Usually, direct bonding results in a strong, hermetic and reliable bond.

Anodic bonding is another technique that is often used in MEMS-technology [80] to make a bond between an electron conducting material (e.g. silicon or a metal) and an ion conducting material (e.g. alkali containing glass) [86–88]. To bond two silicon wafers to each other an intermediate glass layer has to be used [89, 90]. By anodic bonding, the two wafers are placed on top of one another and a high voltage of 200 - 1000 V is applied across them. Usually, the bonding process takes place at an elevated temperature between

180 and 500 °C. Anodic bonding results in strong, hermetic and reliable bonds.

In solder bonding, two surfaces are bonded to each other with the use of a metal or a metal alloy [81]. Normally, a thin layer of the metal or metal alloy is deposited on both surfaces. Then, the surfaces are brought into close contact and heated to the melting temperature of the solder that is used. The solder deforms and reflows, resulting in a strong, hermetic bond, that thermally and electrically conducts well. Solder bonding can take place at a relatively low bonding temperature and has the ability to join various materials. The most commonly used solder alloy is tin-lead, which melts at 360 °C [81]. Also, aluminum is used as solder in bonding silicon to glass at a bonding temperature of 700 °C [91]. In the IC industry, indium solder is widely used for the integration of a chip to its package [92, 93]. Furthermore, flip-chip bonding with indium bumps is often used by chip and hybrid detector array manufacturers to make a thermally and electrically well conducting bond [94, 95]. Typically, indium bonding techniques are performed at 200 °C, but also low-temperature indium welding at room temperature is possible [96].

Eutectic bonding is a variation on solder bonding [81]. This technique makes use of the low melting temperature of certain alloys to bond at a low temperature (typically 200 - 400 °C). It can result in strong, hermetic bonds that thermally and electrically conducts well. The disadvantage is that it is difficult to obtain a complete bond over large areas. In microfabrication, silicon-gold eutectic bonding is widely used [84, 97], which has a melting temperature of 363 °C.

By low-temperature glass bonding, glass or glass frit with a low-temperature melting point is used as intermediate layer [98, 99]. The glass or glass frit layer is deposited on one or both of the surfaces. The surfaces are brought into close contact and heated to the melting point of the glass. The glass melts and reflows which creates an hermetic bond between both surfaces. Typically, the bonding temperature lies in the range of 400 - 1000 °C [100]. This technique has the capability to bond various materials and is often used in the fabrication of hermetic packages of microsensors.

Adhesive bonding is the easiest technique to join two materials [100, 101]. It is cheap, easy to use, and can bond two dissimilar materials. Furthermore, it is not sensitive to surface roughness. A wide selection of adhesives is available for various applications. Most adhesives consist of a polymer. When required, a high thermal conductance adhesive can be made by adding metal particles, for example silver, to it. A good overview of the various types of adhesives is given in [100]. During the bonding process, adhesive is applied to one or to both surfaces. Then, the surfaces are brought into close contact and a pressure is applied. Often, the bonding process takes place at elevated temperatures to increase the bonding speed. The adhesive cures and a bond is formed. Typical bonding temperatures lie in the range of 20 - 150 °C [100]. A disadvantage of adhesives is that the life time is often limited. Furthermore, it can outgas after curing, which is a disadvantage when the device is to be used in a vacuum system.

4.1.2 Selection of suitable bonding techniques

To integrate a detector chip with a JT cold stage, a silicon interface should be bonded to a D263 T glass interface. In our application, the bond should be highly thermally conducting, suitable for use at cryogenic temperatures, strong enough to withstand launch vibrations and outgassing should be very low. Furthermore, the bond should be strong enough to withstand the differences in thermal expansion of silicon and D263 T glass. The coefficient of thermal expansion (CTE) of silicon and D263 T glass are respectively 3.2 x 10^{-6} K^{-1} and 7.2 x 10^{-6} K^{-1} over the range $0 - 300\,^{\circ}C$ [79, 102]. Due to sensitivity of detector arrays for high temperatures, the bond should be formed at a temperature below about 100 °C.

Most of the bonding techniques listed above are tested with Pyrex® glass [103], because this type of glass has a CTE of 3.3 x 10^{-6} K^{-1} that matches closely to that of silicon over the range from bonding temperature to operating temperature. Unfortunately, the CTE of D263 T glass is much higher than that of silicon. This means that not all bonding techniques described above can be used for our application. Using another glass with a similar CTE of silicon, for example Pyrex®, as material for the JT cold stage is not possible, because at present these glasses are only available in wafers with a minimum thickness of 700 μm [79], whereas in the miniature JT cold stage design a thickness down to 145 μm is required [22].

Direct and anodic bonding can only be used for bonding two materials of which the CTE matches closely in the temperature range from bonding temperature to operating temperature, else the bond will crack. Due to the difference in CTE of D263 T glass and silicon, direct and anodic bonding can not be used for making the bond between these materials. Furthermore, the required bonding temperatures for these techniques are much too high for our application. Therefore, standard fusion and anodic bonding are not suitable.

Solder bonding with aluminum, eutectic bonding and low-temperature melting glass bonding all have the disadvantage of a bonding temperature above 200 °C. In most cases, this temperature is too high for detector arrays. These techniques are therefore not suitable for our application. Flip-chip bonding and low-temperature indium welding can both be suitable techniques. Flip-chip bonding is widely used by detector manufacturers to bond the detector array chip to the silicon read-out chip in hybrid arrays [32]. Usually, this technique takes place at bonding temperatures below 100 °C. During low-temperature indium welding the bond is made at room temperature [96]. Therefore, it is expected that both techniques are very suitable for our application.

Bonding by adhesives is also a good option. It is widely used by detector manufacturers to glue a detector chip to its package [81, 104]. Special thermally conducting adhesives are designed for operating at cryogenic temperatures.

4.1.3 Experimental testing of adhesives

Among the various available bonding techniques to bond silicon to glass, adhesive bonding and low-temperature indium welding were selected as suitable techniques for our application, as discussed in the previous section. In the present study, we focus on adhesive bonding, because this is the easiest method. Various suppliers were contacted to find suitable adhesives that fulfill our requirements listed above. The advised adhesives were

- Epo-Tek T7110 of Epoxy Technologies [105]
- Stycast™ 2850 FT with catalyst 9 of Emerson & Cuming [106]
- Eccobond™ 285 with catalyst 9 of Emerson & Cuming[107]
- Hysol EA9361 of Henkel [108]
- EP21TCHT-1 of Masterbond [109]

All the advised adhesives consist of two components and result in a permanent bond. Furthermore, Stycast™ 2850 FT, Eccobond™ 285 and EP21TCHT-1 meet the NASA low outgassing standard [110]. Because of costs, we selected Stycast™ 2850 FT, Epo-tek T7110 and a single component conducting silver paint of Electrolube [111] for testing. The advantage of the latter adhesive is that it is possible to detach the components afterwards.

To test the various adhesives, samples were made consisting of a piece of silicon with dimensions 10 x 10 x 0.7 mm^3 glued to a larger piece of D263 T glass with dimensions 30 x 10 x 0.7 mm^3. Before gluing, the surfaces to join were cleaned with isopropanol. The preparation and the cure schedule for all three adhesives are given in Table 4.1.

The samples were clamped on top of a piece of copper that is connected to the cold tip of a small Stirling cooler. Apiezon N vacuum grease [112] was used as a thermal layer between the samples and the copper piece. Temperatures were measured with platinum resistors (Pt1000) that were glued on top of the silicon, the glass and the copper piece. A schematic of the measurement set-up is shown in Fig. 4.1. During the measurements, the system was placed in a vacuum environment.

Table 4.1: Preparation and cure schedule of various adhesives.

Adhesive	Number of components	Mix ratio by weight	Cure schedule
Conducting silver paint	1	-	23 °C for 24 hours
Stycast™ 2850 FT, catalyst 9	2	A:B[a] 100:4	23 °C for 24 hours
Epo-Tek T7110	2	A:B[a] 100:8	23 °C for 72 hours

[a] A=adhesive, B=catalyst

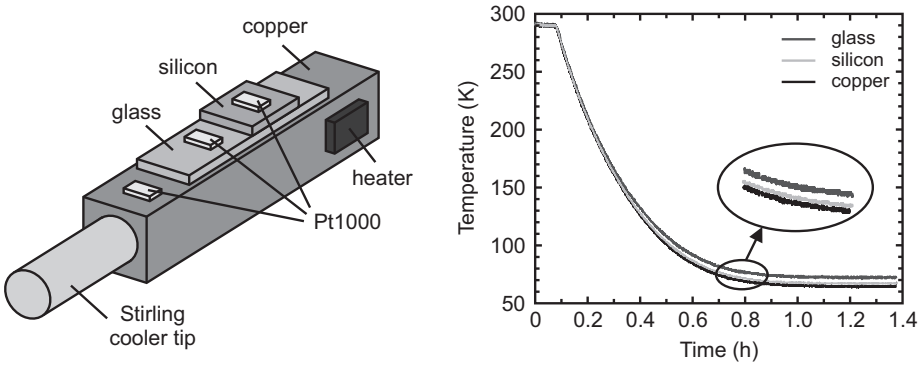

Figure 4.1: Left: schematic of the measurement set-up used for testing various adhesives. Right: measured temperatures versus the time for a typical cool down. In this particular case, Epo-Tek T7110 is used as adhesive. The temperatures from high to low are measured by the glass, silicon and copper sensors, respectively.

To test the various adhesives, the samples were cooled down multiple times from room temperature to about 70 K, during which all three temperatures were monitored. When during cool down the silicon sensor reading is almost equal to the glass sensor reading and both follow the trend of the copper sensor reading, it can be concluded that there is a good thermal contact between the glass and the silicon piece. This means that the adhesive can withstand the differences in thermal expansion and thus is suitable for our application. At last, the various samples were dropped multiple times in liquid nitrogen to test whether the adhesive bond is strong enough to withstand such a thermal shock.

To give an example of the tests, the cool-down curve of a sample that is glued with Epo-Tek T7110 is given in Fig. 4.1. All three temperature readings cooled down from room temperature to about 70 K in about 30 minutes. During cool down the trend of the three temperature readings was equal. The silicon temperature reading is about 2 K higher and the glass reading is 7 K higher than the copper reading. That the glass reading is higher than the silicon reading is due to the radiative heat load on the top surface of both pieces. The silicon is covered with a thin layer of gold, resulting in a much lower radiative heat load than the glass. Hence, the top surface of the silicon has a lower temperature. This temperature difference is confirmed by lumped parameter modeling in ESATAN.

The sample was cooled down multiple times and all different cool downs showed the same results. Therefore, we conclude that there is a good thermal contact between the glass and the silicon and thus the adhesive is strong enough to withstand the difference in thermal expansion. So, Epo-Tek T7110 passed the test. The same tests we did for all three samples and all showed the same results. Finally, the samples were dipped multiple times in liquid nitrogen. The two-component adhesives survived this thermal shock. However, the conducting silver paint did not pass this test. The silicon slice came off the glass piece. Therefore, conducting silver paint is not useful in fast cool-down applications.

4.2 Wiring of the detector array

A photon detector array requires about 50 to 100 electrical connections to its warm-end electronics. The heat conduction through the wiring of the detector array will be a large parasitic heat load on the cold tip. To reduce this heat load, every wire should be optimized in terms of acceptable impedance and thermal heat load. In this section, various methods for the wiring of a detector array are given and the most suitable technique is selected.

4.2.1 Parasitic heat load on the cold tip

The conductive load per wire ($\dot{Q}_{wire}$) of length (l) can be derived from the basic Fourier-Biot equation as [70]

$$\dot{Q}_{wire} = \frac{A_c}{l}\int_{T_c}^{T_h} \lambda_m(T)dT \qquad [\mathrm{W}] \tag{4.1}$$

Here, A_c is the cross-sectional area of the wire, $\lambda_m(T)$ is the temperature-dependent thermal conductivity of the wire material, and T_h and T_c are the warm end and cold-end temperatures, respectively. This means that for minimizing the parasitic heat load due to conduction through the wiring, the ratio A_c/l should be reduced, or a material should be used with low thermal conductivity. However, lower thermal conductivity implies lower electrical conductivity and, therefore, higher electrical losses. Also, a lower A_c/l ratio implies higher electrical losses. Thus, the optimization of a wire is a trade-off between thermal heat load and electrical impedance. A study is done to investigate what wire material can best be used. In this study, it is assumed that a maximum resistance is defined that is allowed for each wire.

The resistance of an electrical wire (R_{wire}) is given by

$$R_{wire} = \frac{l}{\sigma_m A_c} \tag{4.2}$$

where σ_m is the electrical conductivity of the wire. Substituting the ratio A_c/l of Eq. 4.2 in Eq. 4.1 gives

$$\dot{Q}_{wire} = \int_{T_c}^{T_h} \frac{1}{R_{wire}} \frac{\lambda_m(T)}{\sigma_m(T)} dT \tag{4.3}$$

For metals, the ratio of thermal conductivity to electrical conductivity is proportional to the temperature as defined by the Wiedemann-Franz-Lorenz law

$$\frac{\lambda_m(T)}{\sigma_m(T)} = LT \tag{4.4}$$

where L is the so-called Lorenz number, which is assumed to be independent of temperature. Now, the conductive heat flow through a wire can be written as

$$\dot{Q}_{wire} = \int_{T_c}^{T_h} \frac{LT}{R_{wire}} dT = \frac{L}{2R_{wire}}(T_h^2 - T_c^2) = \frac{L}{R_{wire}} T_m (T_h - T_c) \tag{4.5}$$

Here, T_m is the mean temperature of the wire. Table 4.2 gives the thermal conductivity, the electrical conductivity and the Lorenz number at different temperatures for various materials often used for wiring. The table shows that good thermal conductors, such as copper, aluminum and gold have a Lorenz number of about 2.5 x 10 $^{-8}$ V^2 K^{-2}, whereas poor thermal conductors, such as manganin and constantan, typically have a Lorenz number of 5 x 10^{-8} V^2 K^{-2}. According to Eq. 4.5, this implies that the conductive heat load through a wire with allowable resistance (R_{wire}) and length (l) between the two temperatures T_h and T_c is two times higher for bad conductors compared to good conductors.

Consider as an example a detector array that operates at 100 K and requires 50 electrical leads to its warm-end electronics at 300 K with a maximum allowable resistance of 1 Ω. Using Eq. 4.5, the conductive heat load is about 1 mW per wire for good conductors and 2 mW per wire for bad conductors. Taking into account the number of leads, this results in a total conductive heat load of 50 mW and 100 mW, respectively. A copper wire of 1 cm length should have a diameter of 13 μm and a manganin wire should have a diameter of 75 μm. The latter is more practical, but the conductive heat load is doubled in that case.

Table 4.2: Thermal conductivity, electrical conductivity and Lorenz number for various materials at different temperatures. Data taken from Cryocomp [78].

Material	**Temperature** (K)	**Thermal conductivity** (W m^{-1} K^{-1})	**Electrical conductivity** (Ω^{-1} m^{-1})	**Lorenz Number** (V^2 K^{-2})
Copper	100	339	1.78 x 10^8	1.9 x 10^{-8}
	200	350	7.75 x 10^7	2.3 x 10^{-8}
	300	358	5.10 x 10^7	2.3 x 10^{-8}
Aluminum	100	301	2.27 x 10^8	1.3 x 10^{-8}
	200	238	6.29 x 10^7	1.9 x 10^{-8}
	300	237	3.63 x 10^7	2.2 x 10^{-8}
Gold	100	308	1.22 x 10^8	2.5 x 10^{-8}
	200	312	6.10 x 10^7	2.6 x 10^{-8}
	300	312	4.07 x 10^7	2.6 x 10^{-8}
Constantan	100	20.0	2.14 x 10^6	9.3 x 10^{-8}
	200	22.8	2.08 x 10^6	5.5 x 10^{-8}
	300	24.9	2.03 x 10^6	4.1 x 10^{-8}
Manganin	100	14.0	2.22 x 10^6	6.3 x 10^{-8}
	200	17.2	2.13 x 10^6	4.0 x 10^{-8}
	300	33.0	2.10 x 10^6	3.5 x 10^{-8}

Other heat loads that add to the parasitics are the power dissipation in the wire and the radiative heat load on the wire. For photon detector arrays, the current through the wires are typically in the milliamp range and therefore the power dissipation is negligible. The radiative heat load depends on the emissivity of the wire. Bare, unoxidized wires of copper, gold and aluminum will have an emissivity up to about 0.10, whereas wires with an insulation around it will have an emissivity of 0.8 to 1.0. In the first case, the radiative heat load is negligible. When the wires have a high emissivity, the radiative heat load should be taken into account when calculating the parasitic heat load.

4.2.2 Discussion on various wiring techniques

In the IC industry, there are various techniques used to make an electrical connection between a chip and its package [94, 104]. One of them is flip-chip bonding, which, for example, is used in hybrid detector arrays [32] and for CMOS chips [81, 94, 95]. Another technique is wire bonding, where very thin wires of aluminum, copper or gold are used to make the electrical connection [94, 104]. The bond wires have diameters starting at 15 μm and can be up to several hundreds of micrometers for high-powered applications. In cryogenic systems, often long high-resistance wires, for example made of manganin and constantan [113], are used to electrically connect the sensors at the cold side to the warm end.

In flip-chip bonding, indium bumps are deposited on the contacts of both the chip and its package. Then, they are perfectly aligned and squeezed together. The pressure deforms the bumps and welds them together. The resulting bond serves either as an electrical contact and as the mechanical strength that keeps the chip and its package together. In our application, this technique can only be used for bonding monolithic detector arrays to the JT cold stage. In these arrays, usually, the detector array and ROIC are structured onto a silicon wafer and illuminated through the backside. This makes it possible to incorporate the forming of indium bumps in the production process. In hybrid arrays, the ROIC is structured on a silicon wafer and then integrated with the detector array by, for example, flip-chip bonding. It is only possible to structure on one side of the wafer, making it impossible to make electrical connections on the backside. Therefore, in our application, flip-chip bonding cannot be used.

Using high-resistance materials for the wiring, such as manganin and constantan, means that the conductive heat load on the cold tip per wire is two times larger compared to using electrically well conducting materials, as discussed in section 4.2.1. Therefore, we focus on the use of electrically well conducting wires. In this case, the cross-sectional area of the wire should be very small, making wire bonding a good option. Wire bonding is widely used to make the electrical connections between a detector array and its package. Therefore, most detector arrays are already equipped with wire bond pads.

For our application, we will focus on the use of wire bonding. Now, there are two options for the wiring of detector arrays. The first option is to wire bond directly from

Table 4.3: Conductive heat load through an aluminum bond wire of 10 mm length and a diameter of 25 μm for different cold-end temperatures. The warm-end is taken as 296 K.

Cold-end Temperature (K)	**Conductive heat load** (mW)
100	2.3
150	1.7
200	1.1
250	0.5

the detector array to, for example, a surrounding printed circuit board (PCB). One of the disadvantages of this option is that the wire bond is relatively short, typically less than 10 mm. This results in a relatively high conductive heat load. As example, the conductive heat load for an aluminum bond wire of 10 mm length and with a diameter of 25 μm for different cold-end temperatures is given in Table 4.3. In the calculations, the warm-end temperature is taken as 296 K. As shown, the conductive heat load per wire to a sensor operating at 100 K is 2.3 mW. Another disadvantage is that the PCB surrounding the JT cold stage adds additional volume and in that way makes the cooling system larger.

The second option is to structure electrical leads in the gold layer on top of the CFHX from the warm end to the cold end. At the cold end, bond wires can be used to make the electrical connections between the detector array and the leads. Compared to the first option, the advantage is that the conductive heat load is much lower due to the longer lengths of the gold leads, which are about four times longer. Also, the cross-sectional area of every lead can be optimized in terms of acceptable impedance and thermal load by making it wider or smaller. Furthermore, no PCB is surrounding the JT cold stage, resulting in a smaller cooler system. The disadvantage is that in between the leads there is bare glass which has a high emissivity. This results in a higher radiative heat load to the cold stage that can be minimized by reducing the width of the bare glass by using standard photolithography techniques. Another way is to make a three layer stack on top of the CFHX. Electrical leads are structured into the first layer consisting of gold or another electrically well conducting material. Then, an electrically insulating layer with low thermal conductivity is grown on top of the gold leads. That layer is covered subsequently by a thin gold layer that works as radiative shield. In this way, the radiative heat load is reduced a lot while the conducting heat load is only increased with a small amount, due to conduction through the insulating layer and the extra gold layer.

In conclusion, making a three layer stack is the most suitable option for the wiring of a detector array. Compared to direct wire bonding from the detector array to the warm end, the parasitic heat load on the cold tip will be lower due to a longer length of the leads. Also, the cross-sectional area of the wire can be optimized in terms of acceptable

impedance and thermal load in this case. Another advantage of this technique is that the cooling system will be smaller, because no PCB is required around the cold stage.

4.3 Discussion on the conceptual design

A conceptual design of a miniature JT cold stage - photon detector array is made. Among various techniques, adhesive bonding is selected as technique for integrating the detector array with the JT cold stage. It is shown that for our application two-component adhesives are suitable. Advised is the use of an adhesive that meets NASA low outgassing standard, for example Stycast™ 2850 FT with catalyst 9. The wiring of the detector array can best be done by making a three layer stack on top of the cold stage, consisting of a electrically well conducting layer, an insulating layer and another gold layer. Electrical leads can be structured into the first layer along the length of the cold stage. Each lead should be optimized in terms of acceptable impedance and thermal heat load. At the cold end, aluminum wire bonding can be used to make the electrical connections from the leads to the detector array. In this way, the total parasitic heat load due to the wiring is lowest. It is shown that the conductive heat load through a wire with a resistance of 1 Ω between 100 K and 300 K is about 1 mW for good electrical conducting materials and 2 mW for bad electrical conducting materials.

CHAPTER 5

Characterization of miniature Joule-Thomson cold stages

The first micromachined JT cold stages fabricated at the University of Twente had cooling powers around 10 to 20 mW at 100 K. For cooling small detector arrays, JT cold stages are required that have a higher net cooling power in the range of 50 - 150 mW. Therefore, a second generation of miniature JT cold stages was designed that can deliver this cooling power. Experiments were done to measure the performance of these cold stages.

In this chapter, the results of the characterization experiments are discussed. The performance of the bare JT cold stages operating with both nitrogen and methane is measured. The results are used to validate the thermal model of a miniature JT cold stage. Furthermore, a dummy detector array is integrated with a JT cold stage and the performance of such a system is measured and presented.

5.1 Second generation of miniature Joule-Thomson cold stages

For cooling small detector arrays, a new generation of micromachined JT coolers was developed and fabricated in 2009 consisting of two types of single-stage JT cold stages: one with a gross cooling power around 50 mW (low cooling-power cold stage) and the other with a gross cooling power around 250 mW (high cooling-power cold stage) at 100 K. A schematic and photographs of both JT cold stages are shown in Fig. 5.1. As discussed in section1.2, the JT cold stages consist of a stack of three glass wafers. The high and low-pressure lines were placed on top of one another; etched in the top and middle wafer as rectangular channels with supporting pillars. A thin, highly reflective layer of gold (about 200 nm thick) was sputtered on the outer surface to minimize the parasitic heat loss due to radiation. Both were designed to operate with nitrogen between a high pressure of 80 bar and a low pressure of 6 bar. The outer dimensions of the cold stages are 60.0 x 10.0 x 0.7 mm^3. The two types of JT cold stages differ in restriction dimensions resulting in different mass-flow rates (section 3.2) and thus in different gross

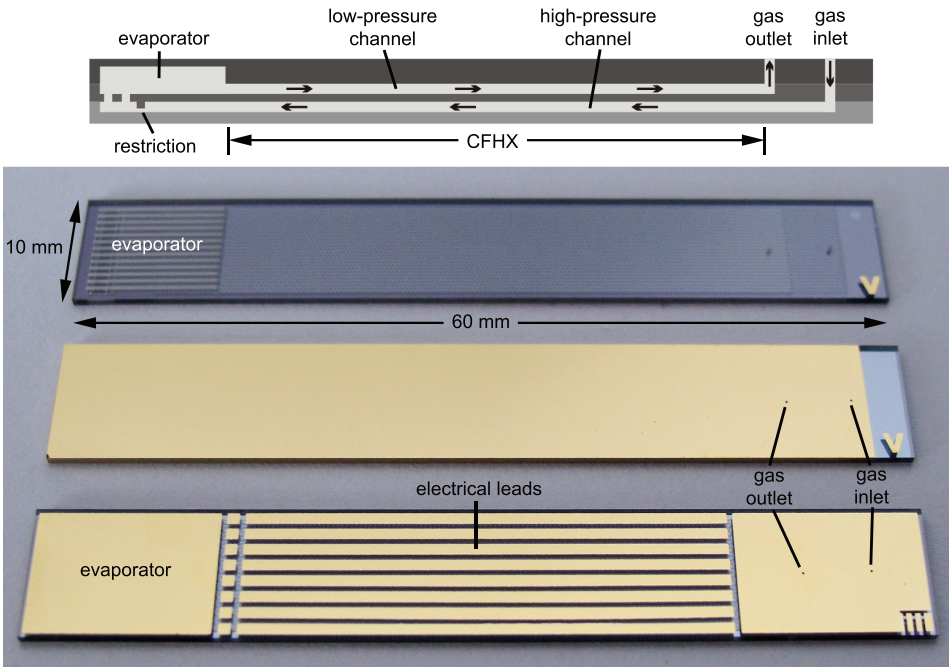

Figure 5.1: Schematic and photographs of the two types of JT cold stages produced in 2009. From top to bottom: schematic, low cooling-power cold stage without and with a gold layer and high cooling-power cold stage with electrical leads structured in the gold layer on top of the CFHX.

Table 5.1: Specifications of the two types of cold stages produced in 2009 for operation with nitrogen and methane.

Type	High pressure (bar)	Low pressure (bar)	Cold-tip temperature (K)	Mass-flow rate (mg s^{-1})	Gross cooling power (mW)
Nitrogen					
High cooling power	80	6	96.4	16.4	250
Low cooling power	80	6	96.4	3.5	53
Methane					
High cooling power	50	4	131.4	5.0	235
Low cooling power	65	4	131.4	1.5	94

cooling powers. The high cooling-power cold stage was supplied with electrical leads that were structured in the gold layer. The specifications of both cold stages for operation with nitrogen and methane are given in Table 5.1.

5.2 Measurement set-up

A schematic of the measurement set-up is given in Fig. 5.2. In the experimental set-up, the working fluid is supplied from a pressurized gas bottle. Then, it flows through a pressure controller to control the high pressure and a mass-flow meter to measure the incoming mass-flow rate. A microtorr® getter filter from Saes Pure Gas Inc. [114] is used to remove most impurities (especially water) from the gas to less than one part-per-billion. This is done to prevent clogging of the JT cold stage due to freezing of water particles [115]. Different filters are used for nitrogen and methane. The working fluid flows trough the JT cold stage that is placed in a glass vacuum chamber. The pressure and mass-flow rate of the outgoing gas stream are measured. A pressure relief valve at the outlet maintains a constant pressure at the low-pressure side and prevents air from the laboratory from flowing into the system. The piping structure in the center can be used to clean the system by means of pumping and flushing.

For the experiments, the JT cold stage is mounted into a flange and surrounded by a PCB. The connections from the gas tubes to the cold stage are made with indium seals. Temperatures are measured with Pt1000 sensors, which are glued to the cold stage by means of conducting silver paint. The accuracy in the temperature measurement is around ± 1 K. Standard surface-mounted-device (SMD) resistors are used as heaters for supplying heat to the cold tip and glued to the cold stage with conducting silver paint. Electrical connections from the sensors to the PCB are made with aluminum bond wires with a diameter of 25 μm.

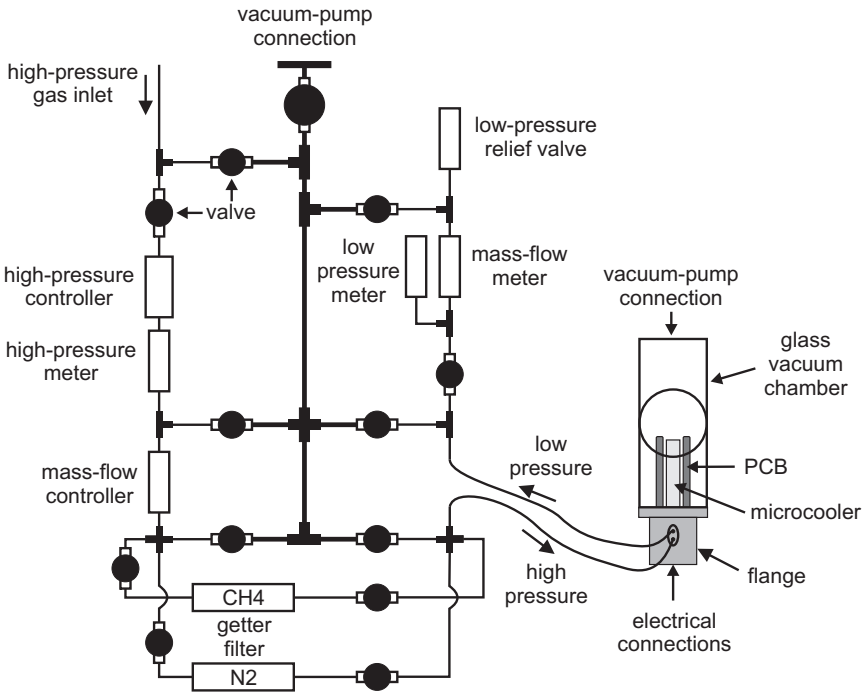

Figure 5.2: Schematic of the measurement set-up used for the characterization of miniature JT cold stages.

5.3 High cooling-power Joule-Thomson cold stage

Seven temperature sensors were glued on top of the low-pressure side of the high cooling-power cold stage to measure the temperature profile along the length of the CFHX. Furthermore, an SMD resistor was glued to the cold tip that was used as a heater for measuring the cooling power. Fig. 5.3 shows the cold stage mounted in a vacuum flange and surrounded by a PCB. The numbering of the sensors used throughout this thesis is indicated as well. Table 5.2 gives the locations of the sensors. The JT cold stage was driven by both nitrogen and methane, and the results are discussed in this section.

5.3.1 High cooling-power cold stage operated with nitrogen

The high-power JT cold stage was operated with nitrogen at a high pressure of 80 bar and a low pressure of 6 bar. In Fig. 5.4, the measured temperature readings and mass-flow rate versus the time are given. The cold tip cooled down from 290 K to 101 K in less than 7 minutes. During the cool-down phase, the mass-flow rate increased from 4.0 to 17.0 mg s^{-1} and after cool down it became stable at 15.6 mg s^{-1}. A finite volume

Table 5.2: Locations of the temperature sensors on the low and high cooling-power JT cold stage corresponding to Fig. 5.3. The numbering of the temperature sensors starts at the cold end.

Sensor	1	2	3	4	5	6	7
High cooling-power JT cold stage							
Location from cold end (mm)	1.5	9.0	13.0	18.5	25.0	30.0	35.0
Location along length of CFHX (mm)	46.5*	39.0	35.0	29.5	23.0	18.0	13.0
Low cooling-power JT cold stage							
Location from cold end (mm)	2.0	5.0	9.5	17.0	-	-	-
Location along length of CFHX (mm)	46.0*	43.0	38.5	31.0	-	-	-

* located on evaporator

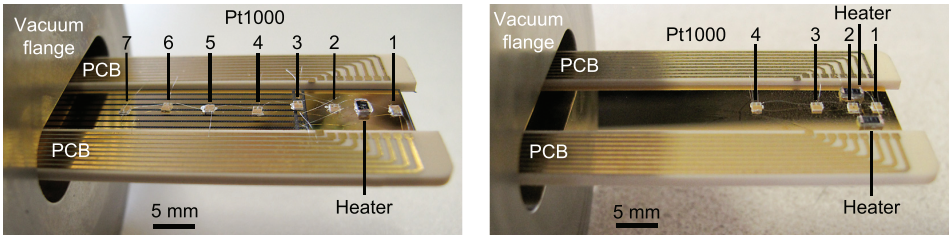

Figure 5.3: Photographs of JT cold stages mounted into a vacuum flange and surrounded by a PCB. The locations of the temperature sensors are given in Table 5.2. The numbering of the temperature sensors starts at the cold end. Aluminum bond wires are used to make the electrical connections between sensors and PCB. Left: high cooling-power JT cold stage and right: low cooling-power JT cold stage.

model made in Ansys Fluent [116] was used to calculate the pressure drop in the low-pressure channel. This pressure drop depends on the mass-flow rate and for 15.6 mg s^{-1} it was calculated to be around 1.6 bar, resulting in a pressure of 7.6 bar in the evaporator. That pressure corresponds to a boiling temperature of 99.7 K, matching the measured temperature within accuracy.

Shortly after the cold tip is 101 K, the second sensor also measured this temperature for a few seconds, but then heated up again. Also in all other temperature sensors a change in reading can be observed at that time. The mass-flow rate at this time reached its maximum value and decreased steeply, resulting in a decrease of cooling power. Most probably, this change in mass-flow rate caused the change in reading of all temperature sensors. Furthermore, at the moment that all sensors reached a stable temperature, the fourth sensor measured a lower temperature than the third one. In addition, there is a temperature difference of about 40 K between the first and the second sensor. It was expected that an isothermal two-phase region forms in the evaporator that may also partly fill the return of the CFHX until there is a heat balance between CFHX efficiency and the

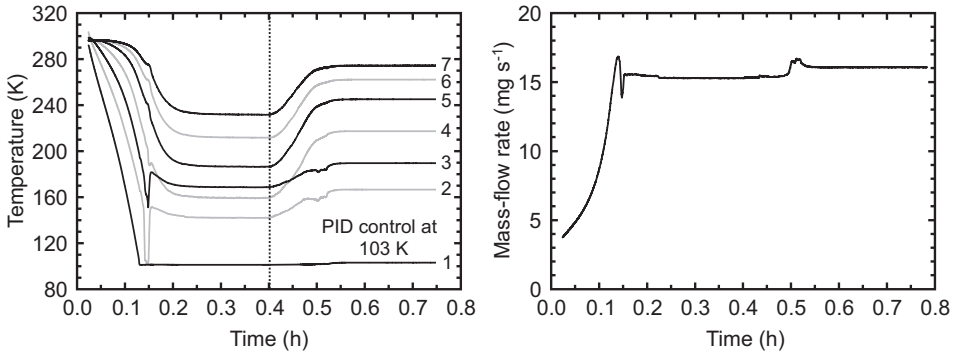

Figure 5.4: Measurement results of the high cooling-power JT cold stage that is operated by nitrogen at a high pressure of 80 bar and a low pressure of 6 bar. Left: temperature versus time measured by seven sensors along the CFHX. The locations of the sensors on the cold stage are given in Table 5.2 and Fig. 5.3. Right: mass-flow rate versus time.

available cooling power. The results show that this is not the case.

This particular cold stage has electrical leads that were structured into the gold layer with uncovered parts of glass in between. This makes it possible to look inside the CFHX while the cold stage is operating. With no heater power supplied, droplets could be observed that move with a high speed into the CFHX as far as sensor four. Most probably, the droplets evaporate around sensor four and in that way cool down this sensor further than sensor three.

By placing temperature sensor one and the heater resistor in a PID control loop, the temperature of the cold-tip can be controlled. This was done for a cold-tip temperature of 103 K. This is slightly higher than the boiling temperature, meaning that all liquid formed is evaporated. The resulting temperature profile is also shown in Fig. 5.4. In this case, all measured temperatures are in increasing order from the cold to the warm end of the CFHX. In addition, all measured temperatures are much higher than in the case where no heater power is supplied. The mass-flow rate increased slightly to a value of 16 mg s^{-1}. The net cooling power of the JT cold stage corresponds to the supplied heater power, which in this situation is 131 mW.

To investigate the effect of gravity on the performance of the JT cold stage, it was operated in different orientations (for example tip down or up). During these measurements, no significant deviations from the performance of the cold stage in horizontal orientation were observed. Mass-flow rates and cool-down times were equal as well as the final temperatures of all sensors. Therefore, it is concluded that gravity has no influence on the performance of the cold stage.

5.3.2 High cooling-power cold stage operated with methane

With the analysis described in section 3.4.1, it is predicted that the high cooling-power cold stage can also be operated with methane. Therefore, experiments were done with methane between a high pressure of 50 bar and a low pressure of 4 bar. In this experiment, only sensors one to six were connected for practical reasons. The measured temperatures, the mass-flow rate and the supplied heater power versus the time are shown in Fig. 5.5. The cold stage cooled down from 297 K in about 4 minutes to a temperature of 138 K. The calculated pressure drop in the low-pressure channel is about 0.6 bar, resulting in a low-pressure of 4.6 bar in the evaporator. That pressure corresponds to a boiling temperature of 134 K. The difference between the measured and the calculated temperature indicates that the pressure drop in the low-pressure channel is 1.1 bar higher than the calculated value. The mass-flow rate increased from 1.4 to 5.9 mg s^{-1} and after cool down it stabilized at 4.9 mg s^{-1}.

As shown in Fig. 5.5, during the cool-down phase two peaks in the mass-flow rate can be observed. The first peak is caused by the forming of two-phase flow in the restriction. As in the case of nitrogen, the second peak coincides with a dip in temperature reading of the second sensor. Again, no isothermal two-phase region was formed in the evaporator. A temperature difference of 36 K was measured between the first and second sensor. After cool down, The fourth sensor measured a lower temperature than sensor two and three, and the fifth sensor was almost at the same temperature of sensor two. By looking inside the cold stage, it was observed that droplets flow far inside the CFHX; as far as the fifth sensor. Most probably, these droplets evaporated around sensors four and five, resulting in lower temperatures of these sensors than that of sensor two and three.

After about 0.3 h, sensor one was placed in a PID loop and controlled at 140 K. Now,

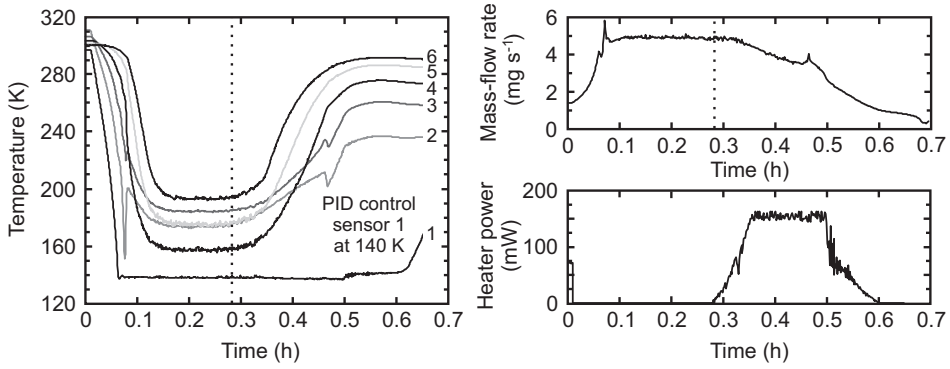

Figure 5.5: Measurement results of the high cooling-power JT cold stage operated by methane between a high pressure of 50 bar and a low pressure of 4 bar. Left: temperature versus time measured by six sensors along the CFHX. The locations of the sensors on the cold stage are given in Table 5.2 and Fig. 5.3. Right: mass-flow rate and supplied heater power versus the time.

all temperatures were in increasing order and much higher than in the case where no heater power was supplied. While heating, the mass-flow rate decreased, as shown in Fig. 5.5. This was caused by the deposition of ice crystals in the restriction, reducing the height and thereby the mass-flow rate. Finally, this resulted in clogging of the restriction at 0.6 h and heating up of the cold stage. A cold stage operating with methane is more sensitive to clogging than one operated with nitrogen, because the cold-tip temperature is much closer to the phase-transition temperature at which ice crystals deposit [115]. The restriction is located between the first and second temperature sensor. While heating, the second sensor measures a temperature in the range of 180 - 230 K. Most probably, the restriction will have a slightly lower temperature, but one which is still in the clogging temperature range, resulting in clogging of the restriction.

5.4 Low cooling-power Joule-Thomson cold stages

To see whether the above-described effects also occur in cold stages with lower mass-flow rates and hence lower cooling powers, the temperature profile was also measured along the length of the low cooling-power cold stage. Now, four temperature sensors were glued on top of the low-pressure side of the JT cold stage. Two heating SMD resistors were placed in series to distribute the applied heat more evenly over the cold tip. The location of the sensors and the heaters are given in the right photograph of Table 5.2 and Fig. 5.3.

5.4.1 Low cooling-power cold stage operated with nitrogen.

The low cooling-power cold stage was operated with nitrogen between a high pressure of 90 bar and a low pressure of 6 bar. Fig. 5.6 shows the measured temperature readings as well as the mass-flow rate and heater power versus the time.

The measured cool-down time from 300 K to 96.3 K was around 90 minutes. During the cool-down phase, the mass-flow rate increased from 1.0 to 4.2 mg s^{-1} and after cool down it became stable at 3.4 mg s^{-1}. The calculated pressure drop corresponding to this mass-flow rate was around 0.4 bar, resulting in a pressure of 6.4 bar in the evaporator. This corresponds to a boiling temperature of 97.3 K, fitting to the measured temperature within measuring accuracy.

As in the high cooling-power cold stage, one can see a drop in the second sensor reading directly followed by an increase in temperature coinciding with a peak in the mass-flow rate. There was a temperature difference of 14 K between the first and second sensor, which is much less than that of the high cooling-power cold stage. Furthermore, the temperature of the second sensor fluctuates as well as that of the third sensor, although to a lesser extent. Most probably, droplets flow into the CFHX where they evaporate at more or less random positions and in that way cause the fluctuations in both temperature readings.

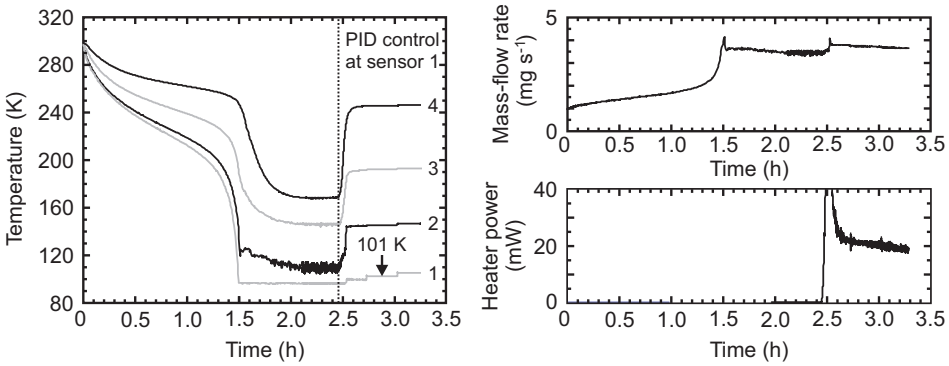

Figure 5.6: Measurement results of the low cooling-power JT cold stage operated with nitrogen at a high pressure of 90 bar and a low pressure of 6 bar. Left: temperature of four sensors placed along the CFHX versus the time. The locations of the sensors are shown in Table 5.2 and Fig. 5.3. Right: mass-flow rate and heater power versus the time.

After about 2.5 h, the temperature of sensor one was controlled by a PID control loop supplying power to both heater resistors. The control temperature was chosen slightly above the boiling point to have all liquid evaporated. The temperature profile in this situation is also given in Fig. 5.6. As shown in the figure, all measured temperatures significantly increased compared to the situation where no heater power was supplied. Also, the mass-flow rate increased due to a change in restriction temperature. When the tip was controlled at 101 K, the measured net cooling power was 21 mW at a mass-flow rate of 3.7 mg s^{-1}.

5.4.2 Low cooling-power cold stage operated with methane

The low cooling-power JT cold stage was also operated with methane at a low pressure of 4 bar. In the analysis of section 3.4.1, it is predicted that this cold stage will cool down when it is operated at a pressure higher than 50 bar. To verify this, first the cold stage was operated at a high pressure of 50 bar. The measured temperatures and mass-flow rate versus the time are given in Fig. 5.7. It is shown that, as predicted, the JT cold stage does not cool down further than about 245 K where the mass-flow rate was 0.4 mg s^{-1}.

The high pressure was increased to 65 bar and the temperatures as well as the mass-flow rate versus time are shown in Fig. 5.8. The cold-tip cooled down in about 10 minutes to 135 K, which corresponds to a boiling pressure of 4.9 bar. The mass-flow rate increased from 0.4 to 1.4 mg s^{-1} and after cool down it measured 1.0 mg s^{-1}. Shortly after cool down, sensor two also measured about 135 K, followed by sensor three. Both sensors suddenly heated up, most probably caused by the decrease in mass-flow rate and thus in cooling power. Again, the mass-flow rate increased causing sensors two and three to cool down again. After about 0.8 h an isothermal two-phase region of 10 x 10 mm^2 was

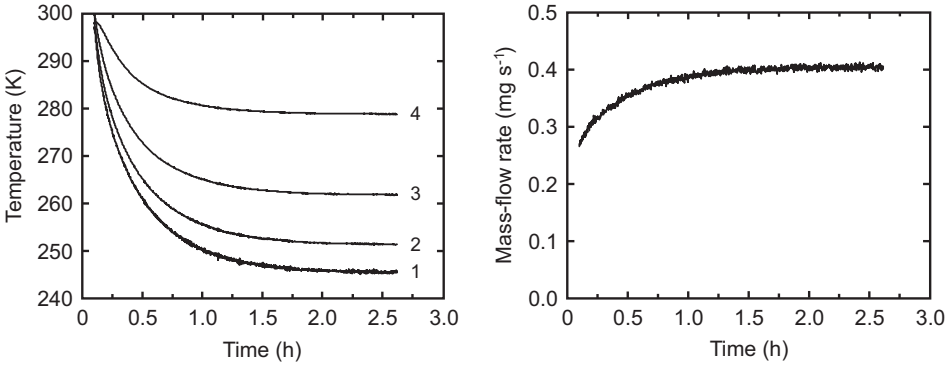

Figure 5.7: Left: measured temperatures and right: mass-flow rate versus time of the low cooling-power cold stage operated with methane between a high pressure of 50 bar and a low pressure of 4 bar. The locations of the sensors are indicated in Table 5.2 and Fig. 5.3.

formed which had a temperature of around 135 K.

By controlling the temperature of sensor four, in principle, the amount of two-phase fluid in the evaporator can be regulated and thereby the area of constant temperature. This was tried after about two hours. However, it appeared impossible to control the temperature of sensor four. Independent of the set point, the temperature of sensor four fluctuated around that value. It is expected that also this time droplets flowed into the CFHX where they evaporated and caused the fluctuations in temperature.

In addition, sensor one was placed in a PID loop and controlled at 137 K, slightly higher than the boiling temperature. As in the case of the high cooling-power JT cold

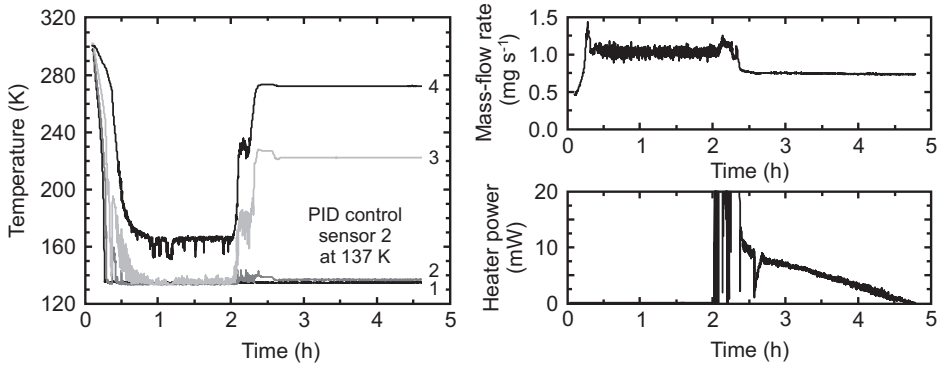

Figure 5.8: Measurement results of the low cooling-power cold stage driven by methane at a high pressure of 65 bar and a low pressure of 4 bar. Left: temperatures versus time and right: mass-flow rate and heater power versus the time. The locations of the sensors are given in Table 5.2 and Fig. 5.3.

stage, also this time the mass-flow rate decreased due to partly clogging of the restriction. However, it was possible to control the second sensor at 137 K. This was done after about 2.5 h and the results are shown in Fig. 5.8. The measured mass-flow rate was 0.75 mg s^{-1}. The supplied heater power and thus measured cooling power was 8 mW and decreased with 4 mW per hour. This decrease is not caused by clogging of the restriction, because the mass-flow rate is constant. As mentioned before, this is most probably caused by an increase in radiative heat load due to the deposition of moisture on the outside of the cold stage.

5.5 Mass-flow rate: theory versus measurement

In section 3.2, two methods were given to calculate the mass-flow rate as a function of the cold-tip temperature. To select the most suitable method, both are compared with measurement data. Fig. 5.9 shows the measured and calculated mass-flow rates versus cold-tip temperature for the high cooling-power cold stage and Fig. 5.10 for the low cooling-power cold stage. The parameters used for calculating the mass-flow rates for both cold stages are given in Table 5.3. In addition, the cold-tip end temperature corresponding to the low-pressure is included in the table. In all cases, the mass-flow rate for isenthalpic expansion (Eq. 3.11) is calculated for different heights of the restriction.

As shown in all figures, the measured mass-flow rate first increases with decreasing cold-tip temperature. At a certain temperature, the mass-flow rate starts to deviate from its trend. Depending on the type of cold stage, for nitrogen this happens around 110 - 120 K whereas for methane this happens around 160 - 180 K. It is expected that this effect is caused by the forming of two-phase fluid inside the restriction. As the cold tip reaches its lowest temperature, the mass-flow rate first increases and then decreases. This can be

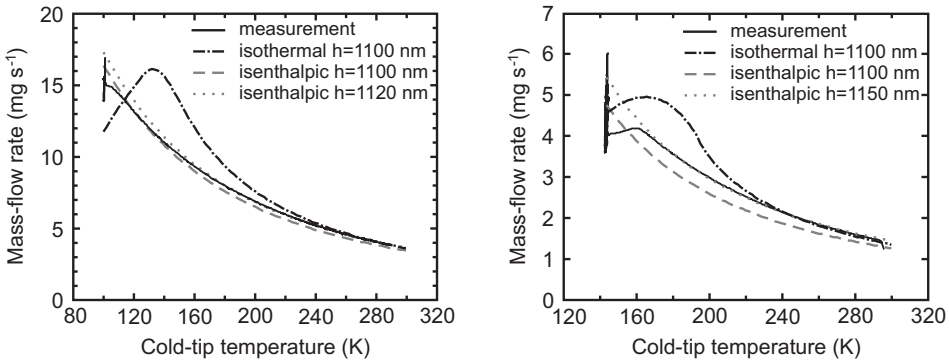

Figure 5.9: Mass-flow rate as a function of the cold-tip temperature for the high cooling-power cold stage operated with left: nitrogen and right: methane. The parameters used for the calculation are given in Table 5.3. In the graph, h is the height of the restriction.

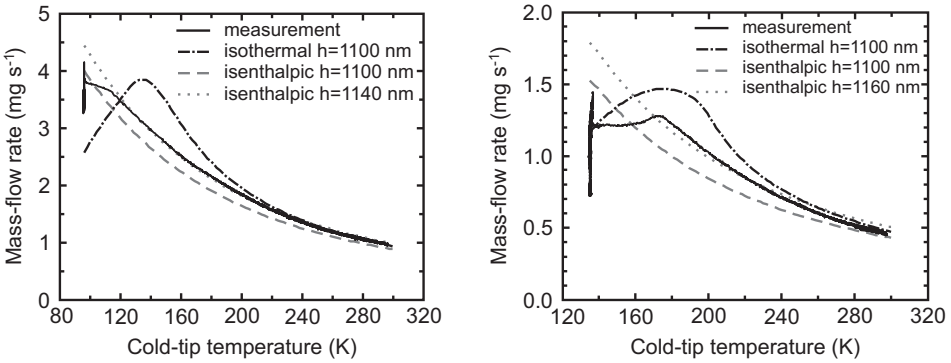

Figure 5.10: Mass-flow rate as a function of the cold-tip temperature for the low cooling-power cold stage operated with left: nitrogen and right: methane. The parameters used for the calculation are given in Table 5.3. In the graph, h is the height of the restriction.

explained by the fact that now two-phase fluid is formed in the evaporator. This flows back into the CFHX and in this way cools down the high-pressure fluid further. Thus, the high-pressure fluid enters the restriction at different temperatures, resulting in a change in mass-flow rate while the cold-tip is cold. For the calculated isenthalpic mass-flow rate curves, this behavior is not shown in order to obtain a clearer picture.

In all graphs, it can be observed that at higher cold-tip temperatures the isothermal expansion method (Eq. 3.12) very well fits the measured values, but starts to deviate at lower cold-tip temperatures. The isenthalpic expansion method (Eq. 3.11) can be used to correctly predict the mass-flow rate during the cool-down phase, with the restriction height being a critical parameter. However, when two-phase fluid starts to form, the evaluation is inaccurate and can be used for approximation only. It can be concluded that

Table 5.3: Parameters used for the calculation of the mass-flow rate for both types of JT cold stages.

Fluid	**High pressure** (bar)	**Low pressure** (bar)	**Cold-tip temperature** (K)
High cooling-power cold stage			
nitrogen	80	8.0	101
methane	50	5.8	138
Low cooling-power cold stage			
nitrogen	90	6.0	96.4
methane	65	4.9	135

the isenthalpic expansion method predicts the measured mass-flow rate better than the isothermal expansion method.

5.6 Thermal model validation

To validate the dynamic model discussed in section 3.5, the results were compared with experimental data. This was done for both types of JT cold stages operating with nitrogen and methane. For the measurements, multiple temperature sensors were placed on top of the low-pressure side of the CFHX, as discussed in sections 5.3 and 5.4. In the model, the conductive heat load through the wiring of the temperature sensors was taken into account by supplying some additional heat to the nodes where these sensors were located.

Fig. 5.11a shows the results of the high cooling-power cold stage operated with nitrogen between a high pressure of 80 bar and a low pressure of 6 bar. The measured and calculated temperatures are shown as a function of the time for the seven temperature sensors that were placed on top of the CFHX. As shown, the calculated cool-down time of sensor one is 385 s and fits very well to the measured time of 387 s. Its temperature is slightly lower than the measured value, because the pressure drop in the low-pressure channel is not taken into account. The calculated temperatures of the other sensors are also in good agreement with the measured temperatures. However, when liquid starts to form, the model is inaccurate and cannot predict the temperatures.

Fig. 5.11b gives the calculated and measured temperature profiles for the case that the first sensor is PID controlled at 103 K. In this situation, all liquid is evaporated by the supplied heater power. The temperature sensors are glued on the cold stage at the low-pressure side and thus should be compared with the calculated temperatures of the

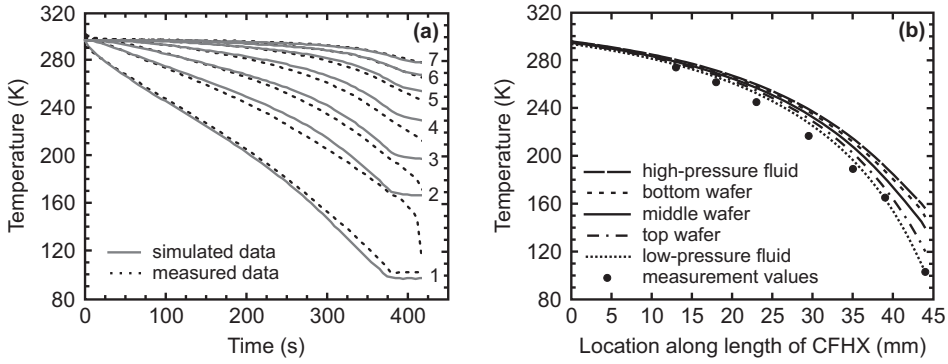

Figure 5.11: a) Calculated and measured temperatures of seven sensors versus the time for the high cooling-power cold stage operated with nitrogen. The locations of the sensors are indicated in Table 5.2 and Fig. 5.3. b) Temperature profile along the length of the CFHX when heater power is supplied.

top wafer. As shown, the calculated profiles are in good agreement with the measured ones (within 10%). In this situation, the gross cooling power minus the internal losses of the CFHX is calculated to be 203 mW. The sum of the radiation losses is 65 mW, the sum of the conduction loss at the warm side of the CHFX is 9 mW and the sum of the experimental losses due to the sensors is 9 mW. This results in a calculated net cooling power of 120 mW. This is slightly lower than the measured cooling power of 131 mW. The various calculated heat losses are summarized in Table 5.4.

Fig. 5.12a shows the calculated and measured temperatures as a function of the time for the low cooling-power cold stage operated with methane between a high pressure of 65 bar and a low pressure of 4 bar. As shown, the calculated cool-down time is 535 s whereas it is 570 s for the measured one. The calculated temperatures for all three sensors fit well to the measured temperatures. Fig. 5.12b gives the measured and calculated temperature profiles for the case that the cold-tip is PID controlled at 137 K. As shown, the calculated profiles are in good agreement with the measured ones (within 5%). The calculated cooling power is around 25 mW at a mass-flow rate of 0.75 mg s^{-1}. This value is much higher than the measured cooling power of 8 mW. The calculated heat losses and measurement results are summarized in Table 5.4.

Simulations were also done for the high cooling-power cold stage operating with methane and the low-cooling power cold stage operating with nitrogen. Table 5.4 gives an overview of the calculated and measured parameters for different measurement configurations. As shown, in all cases the calculated cold-tip temperature is lower than the measured one. This is caused by the pressure drop in the low-pressure channel, which is not taken into account in the thermal model. Furthermore, the calculated cool-down time is shorter than the measured one. This can be caused by several factors. First, the

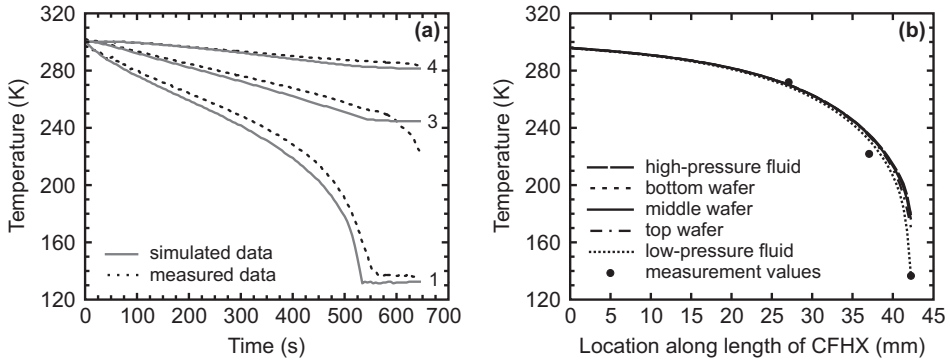

Figure 5.12: a) Calculated and measured temperatures of three temperature sensors versus the time for the low cooling-power cold stage operated with methane. The locations of the sensors are shown in Fig. 5.3 and Table 5.2. b) Temperature profile along the length of the CFHX when heater power is supplied.

Table 5.4: Overview of the calculated and measured parameters for different measurement configurations of a miniature JT cold stage.

Parameter	**High cooling-power cold stage**		**Low cooling-power cold stage**	
Fluid	nitrogen	methane	nitrogen	methane
High pressure (bar)	80	50	90	65
Low pressure (bar)	6	4	6	4
Cold-tip temperature (K)	103	138	101	137
Mass-flow rate (mg s^{-1})	15.6	4.9	3.7	0.75 [a]
Calculated cool-down time (s)	387	165	4980	535
Measured cool-down time (s)	385	190	5400	570
$\dot{Q}_{net,measured}$ (mW)	131	- [a]	21	8 [a]
$\dot{Q}_{net,calculated}$ (mW)	120	186	33	25
$\dot{Q}_{gross}$ (mW)	237	230	77	47
$\dot{m}(h_{Ph,in} - h_{Pl,out})$ (mW)	203	228	61	46
$\sum \dot{Q}_{rad}$ (mW)	65	36	14	11
$\sum \dot{Q}_{loss,warm}$ (mW)	9	1	4	3
$\sum \dot{Q}_{exp}$ (mW)	9	5	11	8

[a] clogging occurred while heating

higher calculated mass-flow rate results in a higher cooling power and thus in a shorter cool-down time. Second, the parasitic heat load due to the sensors can be underestimated in the simulations. Third, moisture can form on the outside of the cold stage, resulting in a higher radiative heat load and thus a longer cool-down time. This latter factor has more influence on the low cooling-power cold stages, because these have much longer cool-down times.

From Table 5.4, we can conclude that the TMM is in good agreement with the measurement data. The calculated values are within 10% of the measured ones. Also, it is shown that for the vapor case the calculated temperature profiles match well to the measured ones within 10%. In the case that liquid is formed the model becomes inaccurate.

5.7 Miniature Joule-Thomson cold stages cooling detector arrays

In sections 5.3 and 5.4, the performance of both types of bare JT cold stages was measured. In addition, experiments were done to study the performance of these cold stages cooling a (dummy) detector array and the results are discussed in this section. A

silicon slice of 10 x 10 mm^2 was used as dummy detector array and glued to the cold tip of the JT cold stages with conducting silver paint. Silver paint was used instead of a two-component adhesive, because then it is possible to get the silicon slice off the cold stage again. Furthermore, cooling with a JT cold stage does not give rise to thermal shocks, so silver paint is suitable for this application. One temperature sensor (Pt1000) was glued on top of the silicon slice with conducting silver paint as well as one SMD resistor that is used to supply heat to the cold tip. Furthermore, two Pt1000s were glued on top of the low-pressure side of the CFHX. Electrical connections from the sensors to the PCB are made with aluminum bond wires with a diameter of 25 μm. Fig. 5.13 shows photographs of both JT cold stages mounted in a vacuum flange and surrounded by a PCB. The numbering of the sensors used throughout the thesis is also indicated. The locations of the temperature sensors are given in Table 5.5.

Table 5.5: Locations of the temperature sensors on the low and high cooling-power JT cold stage cooling a (dummy) detector array corresponding to Fig. 5.13. The numbering of the temperature sensors starts at the cold end.

Sensor	1	2	3	4
High cooling-power JT cold stage				
Location from cold end (mm)	6.5	12.5	26.0	-
Location along length of CFHX (mm)	41.5*	35.5	22.0	-
Low cooling-power JT cold stage				
Location from cold end (mm)	1.7	7.3	11.0	23.0
Location along length of CFHX (mm)	46.3*	40.7*	37.0	25.0

* located on silicon slice

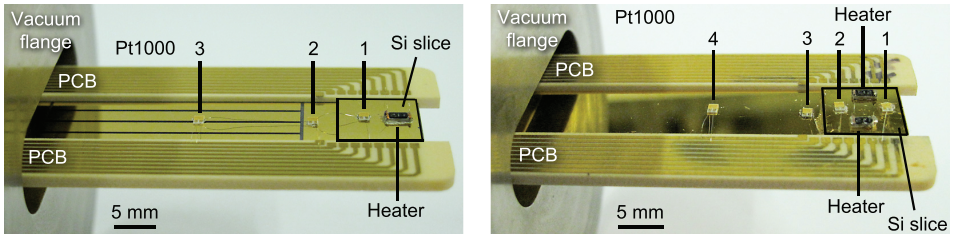

Figure 5.13: Photographs of miniature JT cold stages mounted into a vacuum flange and surrounded by a PCB. A silicon slice is used as dummy detector array and glued to the cold tip of the cold stages. Aluminum bond wires are used to make the electrical connections between the sensors and the PCB. The locations of the temperature sensors are indicated in Table 5.5. Left: high cooling-power JT cold stage and right: low cooling-power JT cold stage.

5.7.1 Low cooling-power Joule-Thomson cold stage

First, the performance of the low cooling-power JT cold stage was measured. This cold stage was operated with methane between a high pressure of 65 bar and a low pressure of 4 bar. The measured temperatures, the mass-flow rate and supplied heater power versus the time are given in Fig. 5.14. As shown, the JT cold stage cooled down from room temperature to 135 K in about 20 minutes. During the cool-down phase, the mass-flow rate increased from 0.5 to 1.9 mg s^{-1} and after cool down became around 1.1 mg s^{-1}.

After about 0.6 h, temperature sensor one was placed into a PID loop and controlled at 138 K. The result is also given in Fig. 5.14. As shown, the silicon slice has a constant temperature of 138 K and the fluctuations in the mass-flow rate reading became less. After stabilization, the supplied heater power was 28 mW.

Compared to the measurements done without a silicon slice (see section 5.4), the cool-down time is larger (20 versus 10 minutes). When no heater power is supplied, the temperature of sensor three is slightly higher than in the case without silicon slice. Most probably, this results in a slightly higher temperature of the restriction and thus in a higher mass-flow rate after cool down (1.1 versus 1.0 mg s^{-1}). The measured net cooling power is also higher (28 versus 8 mW). Part of this can be explained by the higher mass-flow rate during heating. Furthermore, in the case with silicon slice, no clogging of the restriction was observed.

The low cooling-power cold stage was also operated with nitrogen at a high pressure of 90 bar and a low pressure of 6 bar. The cool-down time from room temperature to 100 K was 70 minutes. When the first sensor was controlled at 105 K, the supplied heater power was 6 mW at a mass-flow rate of 2.7 mg s^{-1}. In this case, the measured cooling

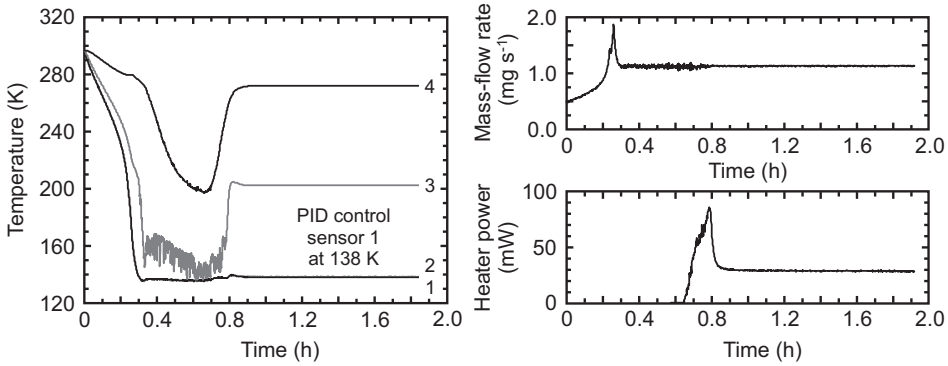

Figure 5.14: Measurement results of the low cooling-power cold stage cooling a dummy device. The cold stage is operated with methane between a high pressure of 65 bar and a low pressure of 4 bar. Left: temperature of the various sensors versus the time and right: mass-flow rate and supplied heater power versus the time. The locations of the temperature sensors are indicated in Table 5.5 and Fig. 5.13.

power is much lower than in the case of the low cooling-power cold stage without silicon slice where the cooling power was 26 mW. Part of this can be explained by the lower mass-flow rate for the cold stage with silicon slice resulting from a lower temperature of the restriction.

5.7.2 High cooling-power Joule-Thomson cold stage

The high cooling-power cold stage was operated with nitrogen between a high pressure of 80 bar and a low pressure of 6 bar. The measured temperatures as well as the mass-flow rate and supplied heater power versus the time are shown in Fig. 5.15. As shown, the JT cold stage cooled down in 11 minutes from room temperature to 103 K. The second and third temperature readings were 137 K and 183 K, respectively. During the cool-down phase, the mass-flow rate increased from 3.5 to 15.0 mg s^{-1} and became stable at 13.2 mg s^{-1}.

After one hour, the first sensor is placed in a PID loop and controlled at 105 K. After a while, the temperature readings of all sensors reached a steady state. The mass-flow rate has increased to 13.6 mg s^{-1} and the supplied heater power was 101 mW. By looking through the bare glass located in between the electrical leads, one could see droplets flowing into the CFHX. This means that not all liquid is evaporated in the evaporator. Therefore, the control temperature of the first sensor was increased to 106 K. The mass-flow rate increased to 14.6 mg s^{-1} and the supplied heater power was 133 mW. Now, no droplets flowed into the CFHX and all liquid is evaporated, resulting in a higher cooling power at the evaporator.

Compared to the measurements done without a silicon slice (see section 5.3), the

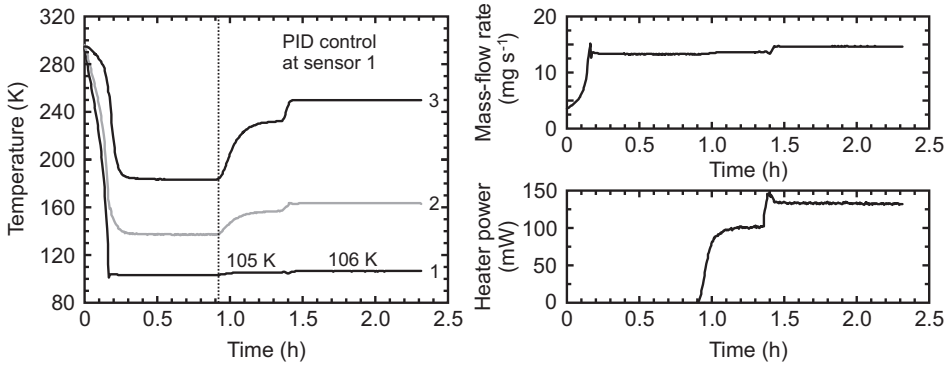

Figure 5.15: Results of the high cooling-power JT cold stage cooling a (dummy) detector array. The cold stage is operated with nitrogen between a high pressure of 80 bar and a low pressure of 6 bar. Left: temperature versus the time measured by three sensors. Top right: mass-flow rate versus the time and bottom right: heater power versus the time. The locations of the temperature sensors are indicated in Table 5.5 and Fig. 5.13.

cool-down time is larger (11 versus 7 minutes) and also the cold-tip temperature after cool down is higher (103 K versus 101 K). Furthermore, the silicon slice has an effect on the temperature profile along the length of the CFHX. At the location of sensor three, the temperature reading is lower than in the case without silicon slice. Most probably, this results in a lower mass-flow rate after cool down (13.2 versus 15.6 mg s^{-1}). The measured cooling powers were almost equal (133 versus 131 mW). However, the mass-flow rate during the measurement with silicon slice was lower (14.6 versus 16.0 mg s^{-1}).

The high cooling-power cold stage was also operated with methane gas between a high pressure of 45 bar and a low pressure of 4 bar. By controlling the first sensor at 144 K, the mass-flow rate was 3.7 mg s^{-1} and the supplied heater power was 110 mW. The same differences between the cold stages with and without silicon slice were observed as in the case of nitrogen as the working fluid.

5.7.3 Thermal model results of a Joule-Thomson cold stage - photon detector array system

In the previous sections, the performance of a miniature JT cold stage cooling a (dummy) photon detector array was measured. In these measurements, a silicon slice covered with a thin layer of gold was used to simulate the array. A detector array, however, can not be covered with such a layer and thus will have a much higher emissivity. Therefore, simulations were performed to investigate whether both types of JT cold stages will cool down when a detector array is integrated on the cold tip. The emissivity of the photon detector array is taken as 0.8, corresponding to that of glass [72].

In the simulations, the high cooling-power cold stage is operated with nitrogen between a high pressure of 80 bar and a low pressure of 6 bar. It is assumed that there are

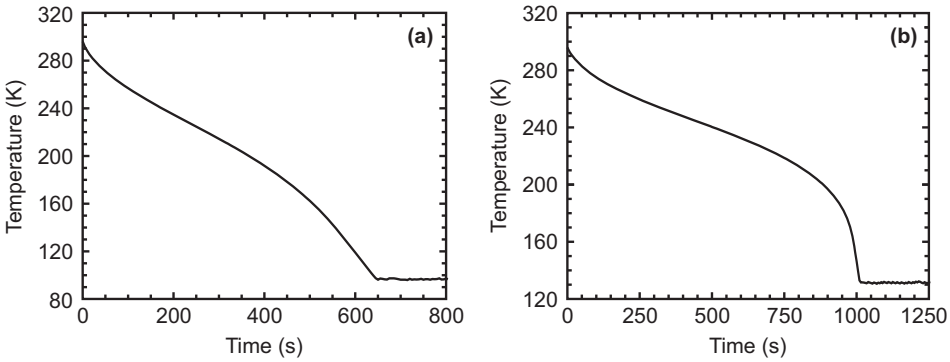

Figure 5.16: Simulated cool down of JT cold stages cooling an optical detector array for a) the high cooling-power cold stage operated with nitrogen and b) the low cooling-power cold stage operated with methane.

Table 5.6: Overview of the calculated heat losses for both types of JT cold stages cooling an optical detector array.

Parameter	High cooling-power cold stage	Low cooling-power cold stage
Fluid	nitrogen	methane
High pressure (bar)	80	65
Low pressure (bar)	6	4
Mass-flow rate (mg s^{-1})	16.7	1.8
$\dot{Q}_{gross}$ (mW)	254	115
$\dot{m}(h_{Ph,in} - h_{Pl,out})$ (mW)	211	113
$\sum \dot{Q}_{rad}$ (mW)	102	41
$\sum \dot{Q}_{loss,warm}$ (mW)	11	1
$\dot{Q}_{net}$ (mW)	99	71

no electrical leads structured into the gold layer. The calculated cold-tip temperature as a function of the time is given in Fig. 5.16a. As shown, the JT cold stage cools down in 650 s to 97 K. The calculated net cooling power is 98 mW, which means that the power dissipation of the detector array and extra parasitic heat load due to wiring should not exceed this value.

In section 5.7.1, it was discussed that the low cooling-power cold stage operating with nitrogen is only suitable for cooling a device that is covered with a thin gold layer, because its net cooling power is only 6 mW. Therefore, in the simulations the low cooling-power cold stage is operated with methane at a high pressure of 65 bar and a low pressure of 4 bar. The cold-tip temperature versus the time is shown in Fig. 5.16b. The JT cold stage cools down in 1010 s to 132 K and the net cooling power is 71 mW. An overview of all calculated heat losses for both simulated JT cold stage are given in Table 5.6.

5.8 Conclusions

The performance of the second generation of JT cold stages operating with both nitrogen and methane was measured and the results were discussed. During the measurements, the gas was supplied from a high-pressure gas bottle. Temperature profiles along the length of the CFHX of both types of miniature JT cold stage were measured as well as their cooling powers. The JT cold stages were operated with nitrogen at a low pressure of 6 bar. At a high pressure of 90 bar, the low cooling-power cold stage cooled down in about 90 minutes to 96 K. The measured net cooling power was 26 mW at a mass-flow rate of 3.4 mg s^{-1}. The high cooling-power cold stage was operated at a high pressure of 80 bar and cooled down in 7 minutes to 101 K. At a mass-flow rate of 15.6 mg s^{-1}, a net

Table 5.7: Summary of the measurement results of the second generation of JT cold stages.

Parameter	**High cooling-power cold stage**		**Low cooling-power cold stage**	
Fluid	nitrogen	methane	nitrogen	methane
High pressure (bar)	80	50	90	65
Low pressure (bar)	6	4	6	4
Cold-tip temperature (K)	103	138	101	135
Cool-down time (min)	7	4	90	10
Mass-flow rate (mg s^{-1})	15.6	4.9	3.7	0.75 [a]
Net cooling power (mW)	131	- [a]	21	8 [a]

[a] clogging occurred while heating

cooling power of 131 mW was measured.

Both miniature JT cold stages were also operated with methane at a low pressure of 4 bar. At a high pressure of 65 bar, the low cooling-power cold stage cooled down in 10 minutes to 135 K. The high cooling-power cold stage was operated at a high pressure of 50 bar and cooled down in 4 minutes to 138 K. Unfortunately, it was not possible to measure the cooling powers of the JT cold stages that were operated with methane, because clogging was occurring while supplying heat to the cold tip. An overview of the measurement results of all JT cold stages is given in Table 5.7.

In chapter 3, two methods for predicting the mass-flow rate were discussed. Both methods were compared with experimental data. It was concluded that the mass-flow rate can best be predicted by calculating it for fully developed, laminar, isenthalpic and viscous flow. However, when two-phase starts to from, the evaluation is inaccurate and can be used for approximations only.

The thermal model of a miniature JT cold stage was validated with experimental data. For all JT cold stages, the model was in good agreement with the experimental data. The calculated values were within 10% of the measured ones. Also, the calculated temperature profiles for the vapor case showed a good agreement with the measured ones.

Furthermore, the performance of miniature JT cold stages cooling a (dummy) detector array was measured. A silicon slice covered with a thin layer of gold was used as a dummy detector and glued to the cold tip of the cold stage with conducting silver paint. Measurements were done for the high cooling-power cold stage and the low cooling-power cold stage both with nitrogen and methane. Table 5.8 gives an overview of the measured properties for each type of JT cold stage. The table shows that the high cooling-power cold stage operated with nitrogen and methane have sufficient cooling power to cool detector arrays that have a power dissipation of 30 mW and require about 50 electrical connections to their warm-end electronics. The low cooling-power cold stage operating

Table 5.8: Overview of the measurement results of the second generation of JT cold stages cooling a (dummy) detector array.

Parameter	**High cooling-power cold stage**		**Low cooling-power cold stage**	
Fluid	nitrogen	methane	nitrogen	methane
High pressure (bar)	80	45	90	65
Low pressure (bar)	6	4	6	4
Cold-tip temperature (K)	106	144	106	138
Cool-down time (min)	11	11	70	20
Mass-flow rate (mg s^{-1})	14.6	3.7	2.7	1.1
Net cooling power (mW)	133	110	6	28

with methane can only be used for cooling detector arrays that have a power dissipation of a few milliwatts and require very few electrical connections. Operating with nitrogen, the low cooling-power cold stage does not have enough cooling power to cool a detector array at all.

CHAPTER 6

Closed-cycle Joule-Thomson cooling

So far, this thesis considered open-loop miniature JT coolers in which the working fluid is supplied from a pressurized gas reservoir. Obviously, the operating time of such a system is limited by the amount of fluid in the reservoir. To obtain JT coolers with a long life-time, a compressor should be used to pressurize the working fluid.

In this chapter, a closed-cycle JT cooler is investigated. A two-stage compressor that was designed for space applications by the Rutherford Appleton Laboratory was combined with a miniature JT cold stage. In the system, a gas mixture is used as the refrigerant. Theory of mixed-gas JT coolers is given and the selection of a suitable gas mixture for our application is described. The performance of the bare compressor operating with the selected gas mixture is mapped as well as that of the mixed-gas JT cooling system and the results are discussed. Furthermore, distributed microcooling in which multiple JT cold stages are driven by a single compressor is described.

6.1 Compressor

The miniature JT cold stages are intended to be combined with a sorption compressor to obtain a closed-cycle JT cooler. These compressors work on basis of the adsorption and desorption of gas on a sorber bed, such as activated carbon [12, 29, 117]. Except for some check valves, sorption compressors do not contain moving parts, resulting in an absolute minimum of vibrations and a long life-time. In another research project running in parallel, a sorption compressor is under development for integration with a miniature JT cold stage. That compressor is not yet available.

The cryogenics group at the Rutherford Appleton Laboratory (RAL) has a long history in the development of mechanical coolers for space applications [118–120]. They developed a 4 K cooler based on the JT expansion of helium through a fine nozzle as component of the closed-cycle cooling system for the high frequency instrument on the Planck explorer (launched in 2009) [121–123]. The compressors of this cooler are based on a diaphragm spring suspension system consisting of spiral arm springs with high radial stiffness enabling clearance seals to be used. The absence of rubbing parts makes the compressor capable of a long life-time (3 to 5 years). To minimize vibrations, a balanced pair of compressors is used that are driven in anti-phase. Drive electronics monitor the out of balance of the compressor pair via force transducers and adjust the drive current accordingly. Reed valves regulate the alternating pressure pulse to a DC flow as required by the JT cold stage. The compressors are described in more detail in [118, 122].

In collaboration with RAL, we have the opportunity to use a compressor pair to drive a miniature JT cold stage. In two stages, a compression of 1 to 10 bar can be obtained for helium at a mass-flow rate of about 5 mg s^{-1}. This modest compression ratio means that we can not use a pure working fluid in the cooling system. Therefore, gas mixtures will need to be used that are much more efficient and can be operated at much lower operating pressures. Mixed-gas JT coolers and the selection of the gas mixture that can deliver cooling capacity at 150 K are described in the next section.

6.2 Mixed-gas Joule-Thomson cooling

Mixed-gas JT coolers are under investigation since the mid-1930's when Podbielniak proposed a mixed-gas refrigerating system with a series of heat exchangers and phase separators for industrial use [124]. In 1969, Fuderer and Andrija for the first time operated a mixed-gas JT cooler without using phase separators [125]. Since the late 1980's, a lot of research is done regarding the use of gas mixtures in small JT cooling systems [2, 25, 69, 126–133]. Compared to JT cryocoolers operating with pure working fluids, mixed-gas JT cryocoolers have the advantage that a significant cooling power can be reached at relatively low operating pressures (below 25 bar). In this section, the theory of mixed-gas JT coolers is given and the selection of a gas mixture for our application is described.

6.2.1 Theory

As discussed in section 1.1, the operating principle of a JT cooler is based on the reduction in enthalpy of the working fluid with increasing pressure. The enthalpy of a working fluid highly depends on pressure close to its phase change from gas to liquid. Thus, JT coolers are more efficient when the compression takes place closer to the two-phase region. Cryogenic JT coolers have to establish a large temperature step and the compression of a pure working fluid takes place far from its two-phase region. During compression, the working fluid behaves almost as an ideal gas and this results in a modest JT cooler efficiency even at high pressure ratios. Fig. 6.1 gives an example of the enthalpy as a function of the temperature for nitrogen at 80 bar and 6 bar. As shown, the enthalpy difference is very low at room temperature and increases steeply close to the two-phase region.

The efficiency of a JT cooler operating with a pure fluid can be increased by adding components with a higher boiling point. This results in a more uniform enthalpy difference between the high pressure and low-pressure flows and hence a higher cycle efficiency. Maytal et al. have shown that the performance of a JT cooler is increased as the number of components is increased [2]. Mixed-refrigerant JT coolers do not boil at a constant temperature as pure fluids do. This means that the operating temperature directly depends on the amount of heat supplied to the cold tip. Supplying a little more heat directly results in an increase in operating temperature.

In section 1.1, the gross cooling power of a JT cooler was defined as the change in enthalpy at the warm end (Eq. 1.1). However, this analysis assumes that the minimum isothermal enthalpy difference (Δh_{min}) between the high pressure and low-pressure flows occurs at the warm end of the heat exchanger. This assumption holds for pure fluids, but for mixed-gas refrigerants Δh_{min} should be determined over the complete operating temperature range of the heat exchanger.

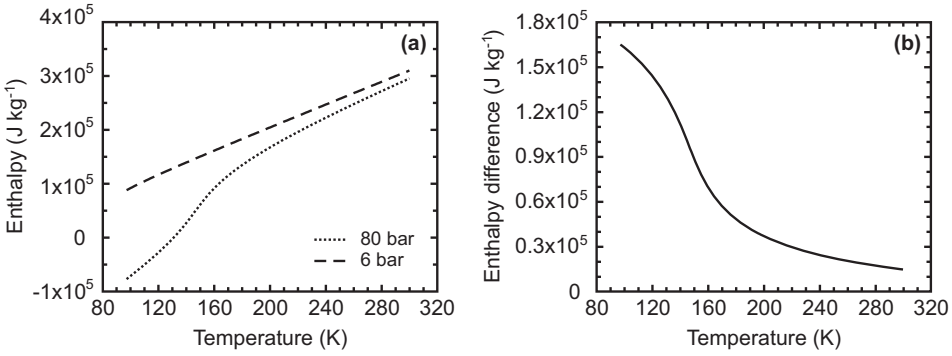

Figure 6.1: a) Enthalpy as a function of the temperature for nitrogen at 80 bar and 6 bar and b) corresponding isothermal enthalpy difference.

Marquardt et al. [126] developed a method to optimize the mixture composition that is based on maximizing Δh_{min}. Components are selected that boil at different points across the temperature range of interest. Freezing of the mixture in the JT cooler should be avoided. Unfortunately, not much is known about the freezing point of mixed-refrigerants in JT systems. In general, the freezing point temperature of a gas mixture is taken as the mole fraction weighted average of the triple points of the various components [2]. Furthermore, it should be checked whether the required temperature profile in the heat exchanger is possible (i.e. the temperature of the high-pressure fluid at any point in the heat exchanger has to be higher than that of the low-pressure fluid). This can be done by plotting the temperature of both fluid flows versus the fraction of enthalpy exchanged.

6.2.2 Selection of a mixed-gas refrigerant

The high cooling-power JT cold stage will be combined with the linear compressor of RAL to obtain closed-cycle JT cooling. An operating temperature of the cooler of 150 K is selected and the gas mixture should operate between 1 bar and 10 bar. We decided to focus on the use of a ternary mixture. Although adding more components will make the mixture more efficient, this will also lead to a more complex optimization and production process. During the selection process the temperature at the warm-end is 297 K. The fluid properties were taken from Refprop [74].

An optimization study was done to select the optimal composition of the ternary gas mixture. Various combinations of fluids and different compositions were taken into account. On basis of maximizing the minimum isothermal enthalpy difference in the temperature range of interest, a mixture of 39 mol% methane, 20 mol% ethane and 41 mol% isobutane was selected. The difference in enthalpy between the high pressure

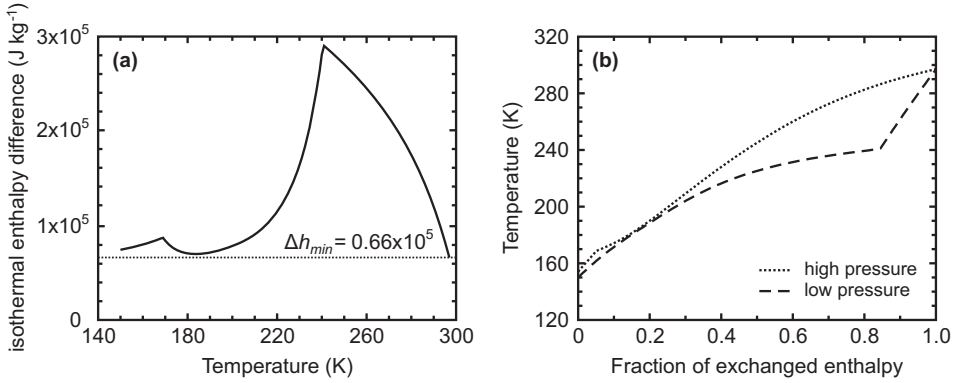

Figure 6.2: a) Isothermal enthalpy difference versus the temperature for a gas mixture of 39 mol% methane, 20 mol% ethane, 41 mol% isobutane between 1 bar and 10 bar. b) Temperature of the high pressure and low-pressure fluid in the CFHX versus the fraction of enthalpy exchanged.

and low-pressure flows as a function of the temperature is shown in Fig. 6.2a. The minimum isothermal enthalpy difference is 0.66 x 10^5 J kg^{-1} and occurs at the warm end of the heat exchanger. The temperature of both fluid flows as a function of the fraction of enthalpy exchanged in the heat exchanger is shown in Fig. 6.2b. The minimum temperature difference between both streams in the heat exchanger is calculated to be 1 K. Therefore, it is expected that this gas mixture will work.

To calculate whether the high cooling-power JT cold stage can be operated with the selected gas mixture, the analysis of section 3.4 can be performed. However, for this analysis the specific heat, thermal conductivity and viscosity of the gas mixture are required. These properties are unknown in the two-phase region. Because in the largest part of the CFHX the gas mixture is in its two-phase region, the *FOM* can not be calculated. As an indication whether the area of heat exchange is large enough, we therefore compare the enthalpy that has to be exchanged in the heat exchanger. In case of the selected gas mixture, 611 mW should be exchanged at a mass-flow rate of 1 mg s^{-1}. This is about one fifth of the heat that has to be exchanged in the case of nitrogen. Therefore, it is expected that the CFHX is large enough for operation with the gas mixture.

The mass-flow rate versus the cold-tip temperature was calculated above 230 K. There was no fluid property data available below that temperature. The result for an isenthalpic expansion is given in Fig. 6.3a. The mass-flow rate of methane operating between 33 bar and 4 bar is also indicated in this figure. As shown, the mass-flow rate at room temperature is about 0.16 mg s^{-1} and increases to 0.52 mg s^{-1} at 230 K. Over the complete temperature range, the mass-flow rate of the gas mixture is lower than that of

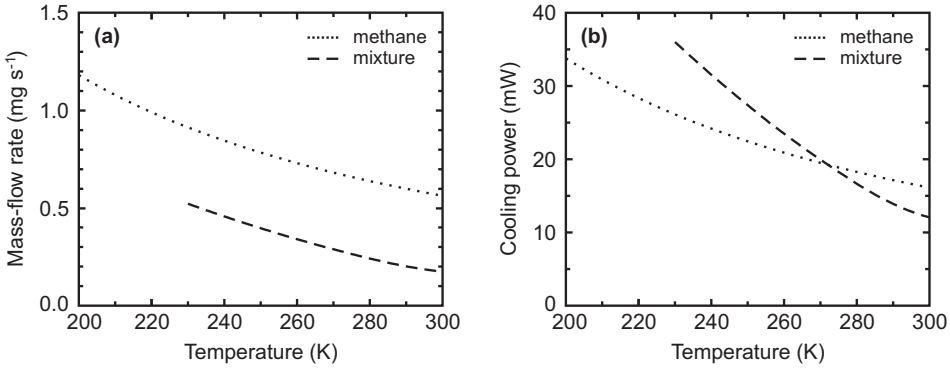

Figure 6.3: Comparison of the high cooling-power JT cold stage operating with a gas mixture of 39 mol% methane, 20 mol% ethane and 41 mol% isobutane operating between 1 bar and 10 bar, and methane between 4 bar and 33 bar. a) Calculated mass-flow rate versus the cold-tip temperature. The calculations were performed for an isenthalpic expansion. b) Calculated gross cooling power as a function of the cold-tip temperature.

methane. Fig 6.3b gives the gross cooling power as a function of the cold-tip temperature of both fluids. Measurements have shown that the high cooling-power JT cold stage can cool down as it is operated with methane between 33 bar and 4 bar and therefore this line represents the minimum gross cooling power required during cool down. As shown, above 275 K the gross cooling power of the JT cold stage operating with the gas mixture is lower than that of methane. During experiments, it is observed that JT cold stages that do not fully cool down typically reach temperatures in the range of 200 - 250 K. Therefore, it is expected that the high cooling-power JT cold stage operated with the gas mixture will cool down although at the beginning the gross cooling power is lower than in the case of methane.

In the discussion above, it is assumed that the mass-flow rate will increase with decreasing cold-tip temperature as calculated. However, measurements with methane and nitrogen have shown that the mass-flow rate does not increase or even decreases when two-phase flow is formed in the restriction. In the case of the selected gas mixture, most probably at room temperature already two-phase flow exist in the restriction. Based on the experiences with nitrogen and methane, it can be expected that the mass-flow rate will not increase during cool down. When this is the case, the high cooling-power JT cold stage will not cool down due to its very low cooling power of a few milliwatts at 0.16 mg s^{-1} mass-flow rate.

6.3 Closed-cycle Joule-Thomson cooler characterization

6.3.1 Compressor performance

The linear compressor of RAL is designed to operate with helium. The compression is assumed to be adiabatic. This means that for a given swept volume, the compression ratio that can be reached depends on the fluid that is used. For monatomic fluids, the pressure ratio will be higher than for diatomic or polyatomic fluids. Also, the input power to the compressor will be higher for monatomic fluids. Therefore, first the performance of the bare compressor operating with the selected mixture was mapped. During the experiments, the low, medium and high pressures of the two-stage compressor were measured. A needle valve is used to adjust the mass-flow rate through the system that is measured as well at the low-pressure side of the system.

During the experiments, the compressor was filled at various pressures. A higher filling pressure results in a higher outlet pressure of the compressor, but also in a higher inlet pressure and vice versa. The performance was measured for various strokes and operating frequencies of the pistons. Fig. 6.4a gives the results of the measured pressures versus the frequency of the pistons for a filling pressure of 5 bar and a stroke of 7 mm. As shown, the compression ratio increases with increasing frequency. The maximum compression is reached at 40 Hz and measures 1.5 to 10.7 bar for zero mass-flow rate.

Also, we have measured the performance of the compressor for various mass-flow

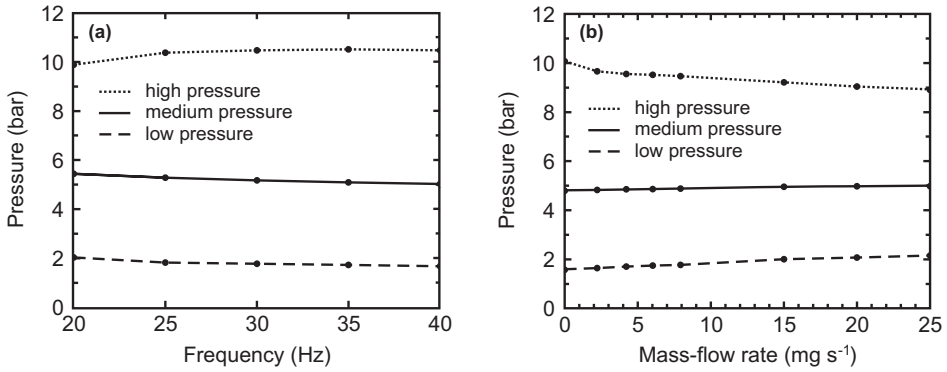

Figure 6.4: Measured performance of the linear compressor filled with 5 bar of the gas mixture 39 mol% methane, 20 mol% ethane and 41 mol% isobutane. a) Pressures versus the operating frequency for a stroke of 7 mm and b) pressures versus the mass-flow rate through the system as the compressor is operated at 40 Hz and a stroke of 7 mm.

rates at a frequency of 40 Hz and a stroke of 7 mm. The pressures versus the mass-flow rate are shown in Fig. 6.4b. It is obvious that the compression ratio decreases with increasing mass-flow rate. At a mass-flow rate of 25 mg s^{-1} the compression was from a low pressure of 2.2 bar to a high pressure of 8.9 bar.

6.3.2 Performance of a closed-cycle Joule-Thomson cooler

The high cooling-power cold stage is combined with the RAL compressor to obtain a closed-cycle JT cooler. One Pt1000 was glued to the cold tip of the cold stage with conducting silver paint. Aluminum bond wires with a diameter of 25 μm were used to make the electrical connections between the sensor and the surrounding PCB. In the experimental set-up, the high, medium and low pressures of the compressor stages are measured. The high-pressure fluid flows through a microtorr® getter filter from Saes Pure Gas Inc. [114] to decrease the amount of water particles in the gas mixture below one part-per-billion. Then, it flows through the JT cold stage and at the low-pressure side of the system the mass-flow rate is measured. A schematic of the measurement set-up is given in Fig. 6.5. The tubing in the center can be used to clean the system by means of pumping and flushing.

The compressor was filled with the gas mixture to a pressure of 5 bar and operated at a frequency of 40 Hz and a piston stroke of 7.5 mm. Fig. 6.6 gives the measured cold-tip temperature, pressures, and mass-flow rate versus the time. As shown, the JT cold stage was operating between 10.4 bar and 1.5 bar. The compression ratio is slightly higher than measured in section 6.3.1, due to the increase in piston stroke. During operation, the compression ratio slightly differed due to a change in temperature of the compressor. The JT cold stage did not cool down further than 284 K. The measured mass-flow rate

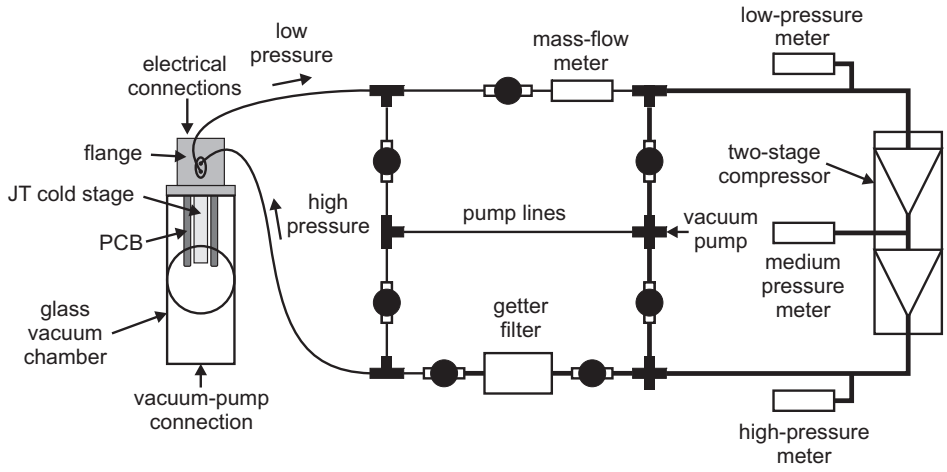

Figure 6.5: Schematic of the experimental set-up used to measure the performance of a closed-cycle JT cooler.

was 0.16 mg s^{-1} and the fluctuations indicate that liquid is formed in the evaporator. Furthermore, the mass-flow rate did not increase during cool down, resulting in a constant cooling power.

For the operation of this JT cold stage, it is crucial that the mass-flow rate increases with decreasing cold-tip temperature. Else, the cooling power is too low to cool down the cold stage. To investigate the mass-flow rate versus the cold-tip temperature, another cooler is used to precool the cold-tip. Fig. 6.7 gives the measured cold-tip temperature, pressures and mass-flow rate versus the time. The cold-tip of the cold stage was

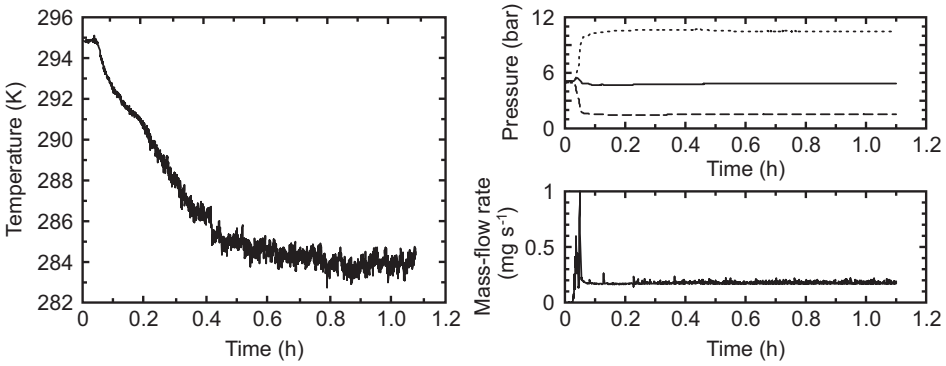

Figure 6.6: Measurement results of the high cooling-power JT cold stage combined with the RAL compressor operating with 39 mol% methane, 20 mol% ethane and 41 mol% isobutane. Left: cold-tip temperature versus the time. Right: pressures and mass-flow rate versus the time.

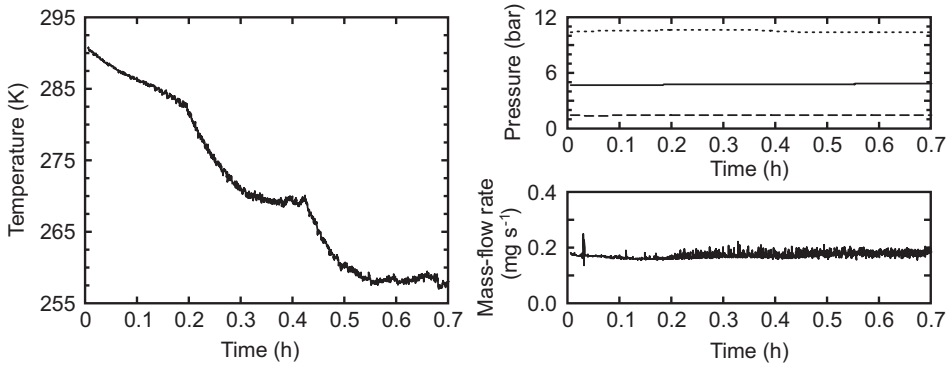

Figure 6.7: Measurement results of the high cooling-power JT cold stage combined with the RAL compressor operating with a gas mixture of 39 mol% methane, 20 mol% ethane and 41 mol% isobutane. The tip is precooled by another cooler. Left: cold-tip temperature versus the time. Right: pressures and mass-flow rate versus the time.

cooled down to 257 K. During the cool down phase, the measured mass-flow rate was 0.17 mg s^{-1} and did not increase. This means that the gross cooling power of the cold stage did not increase during cool down. Therefore, the high cooling power JT cold stage cannot be used in combination with this compressor. A JT cold stage with a larger restriction is designed for operation with this compressor. At present, this JT cold stage is not yet fabricated.

6.4 Distributed Joule-Thomson cooling

The RAL compressor can deliver a relatively large flow with only a small decrease in compression ratio. For a mass-flow rate of 10 mg s^{-1}, a compression of 1.8 bar to 9.4 bar was measured for the gas mixture with composition 39 mol% methane, 20 mol% ethane and 41 mol% isobutane (Fig. 6.4). Therefore, this compressor can be used to obtain a distributed cooling system in which multiple JT cold stages are combined with a single compressor. The JT cold stages can be distributed over the satellite, remote from the compressor. This allows for maximum flexibility in interfacing and satellite design.

In a distributed JT cooling system, in principle, each JT cold stage is operated between the same pressures. Therefore, the cooling power of each JT cold stage depends on the mass-flow rate. This means that each JT cold stage can be optimized in terms of cooling power by adjusting its restriction size. The operating temperature of each JT cold stage can be varied within limits through the heat load.

At the moment that JT cold stages are available that are suitable for operation with the selected gas mixture, experiments should be done on such a distributed cooling system.

6.5 Conclusions

To obtain a closed-cycle JT cooler, the high cooling-power JT cold stage is combined with a linear compressor of RAL. Because this compressor only can deliver a relatively modest compression of about 1 to 10 bar, a mixed-gas will be used as refrigerant in the cooling system. By optimizing the minimum isothermal enthalpy difference, a gas mixture of 39 mol% methane, 20 mol% ethane and 41 mol% isobutane was selected that can operate at about 150 K. The performance of the compressor for various operating parameters was mapped. Filled with 5 bar of the selected mixture, a maximum compression of 1.5 to 10.7 bar was measured at zero mass-flow rate. At a mass-flow rate of 25 mg s^{-1}, a compression of 2.2 to 8.9 bar was obtained.

The high cooling-power JT cold stage was combined with the compressor and the performance of the cooling system was measured. The cooler did not cool down further than 284 K due to the low mass-flow rate of 0.16 mg s^{-1}, resulting in a too low cooling power. It was observed that the mass-flow rate did not increase with decreasing cold-tip temperature as is required to have sufficient cooling power to fully cool down the cooler. Therefore, the RAL compressor cannot be combined with the available high cooling-power JT cold stage.

CHAPTER 7

Conclusions and Outlook

In this thesis, the application of miniature JT coolers for cooling small optical detector arrays in space applications is investigated. The scope of the project was to obtain distributed JT microcooling of small detector systems for future space missions. In chapter 1, the project was divided into four main steps including the identification of detector systems that are suitable for cooling with a miniature JT cold stage, the development of a conceptual design of a JT cold stage - detector system, the design and testing of micromachined JT cold stages and the realization of distributed microcooling in which multiple cold stages are driven by a single compressor. In this chapter, the main results, conclusions and outlook are discussed.

7.1 Detector arrays that are suitable for cooling with a miniature JT cold stage

A wide variety of optical detector arrays exists that can be divided into thermal and photon detector arrays. In space-based astronomy, thermal detector arrays in the form of bolometers are used for the sub-mm spectral range that operate at a temperature in the order of 100 mK. Therefore, this type of detector array is not suitable for cooling with a JT cooler. Photon detector arrays are used to detect radiation in the spectral range of 0.2 - 25 μm. The operating temperature of these arrays depends on the spectral range of interest and the incoming photon flux and lies typically within the wide range of 10 - 300 K. State-of-the-art detector arrays have dimensions as small as 2 x 2 mm^2 and as large as 40 x 40 mm^2. They have a power dissipation of a few milliwatts to about 200 mW and require about 50 to 100 electrical connections to their external warm-end electronics.

Following a survey among photon detector arrays offered by the major manufacturers, it was concluded that arrays based on silicon, InGaAs and HgCdTe (sensitive for SWIR and MWIR radiation) can be cooled by single-stage JT coolers. It is difficult to give exact specifications of a detector array required to be suitable for miniature JT cooling, because this depends on various parameters, such as operating temperature, amount of electrical connections and power dissipation. As an indication, the detector arrays can have up to 512 x 512 pixels. At a pixel pitch of 15 x 15 μm^2, the corresponding array size is about 10 x 10 mm^2. This is equal to the cold-tip size of the miniature JT cold stages used in this thesis. Furthermore, the JT cold stages typically have net cooling powers up to 150 mW at 100 K. This makes it possible to cool detector arrays which have a power dissipation up to about 50 mW, so that cooling power is left for cooling other parasitic heat loads such as conductive heat load through the large amount of wiring and radiative heat load.

State-of-the-art detector arrays require a huge amount of electrical leads to their warm-end electronics. This results in a large parasitic heat load through the wiring of the arrays that limits the application of miniature JT cold stages for cooling these detector arrays. However, the use of CMOS-technology for the fabrication of detector arrays makes it possible to implement almost any desired circuit on the detector chip. Thus, in principle, most of the read-out electronics that nowadays is external to the detector chip can be integrated on the chip. This minimizes the amount of electrical connections required to operate the detector array. Nowadays, for commercial applications, most electronics is already integrated on chip in monolithic silicon arrays. Also in space applications, some star trackers and sun sensors have electronics on chip. However, in astronomy, the focus is on fabricating high-performance detector arrays rather than on producing highly integrated detector arrays.

7.2 Conceptual design of a JT cold stage - detector array system

A conceptual design of a miniature JT cold stage - photon detector array is made focusing on the interface between cooler and detector array and on the wiring of the array. Among various techniques that can be used for integrating the detector array with the JT cold stage, adhesive bonding is selected. Experiments have shown that for our applications two-component adhesives are suitable. Advised is the use of an adhesive that meets the NASA low outgassing standard, for example Stycast™ 2850 FT with catalyst 9.

Different ways of wiring of the detector array were investigated. It was shown that the conductive heat load through a wire with a resistance of 1 Ω between 100 K and 300 K is about 1 mW for electrically well conducting materials and 2 mW for electrically bad conducting materials. In our application, the wiring of the detector array can best be done by making a three layer stack on top of the cold stage, consisting of a electrically good conducting layer, an insulating layer and a gold layer. Electrical leads can be structured into the first layer along the length of the cold stage. Each lead should be optimized in terms of acceptable impedance and thermal heat load. At the cold end, aluminum wire bonding can be used to make the electrical connections from the leads to the detector array. In this way, the total parasitic heat load due to the wiring is minimized.

7.3 Miniature JT cold stages

The application of miniature JT cold stages for cooling detector arrays within the temperature range 65 - 250 K was investigated. The most suitable working fluid for a JT cold stage operating at a specific temperature in the range of 65 - 250 K was selected on basis of the *COP*, defined as the ratio of gross cooling power to the change in Gibbs free energy of the fluid during compression. In addition, a FOM is evaluated that is a measure for the efficiency of heat exchange in the CFHX. The larger the FOM, the shorter the CFHX can be. The most suitable working fluids in a small temperature range are nitrogen (65 - 70 K), carbon monoxide (70 - 77 K), oxygen (77 - 84 K), argon (84 - 95 K), methane (95 - 124 K), nitrogen trifluoride (124 - 146 K), ethylene (146 - 159 K), ethane (159 - 188 K), hydrogen sulfide (188 - 212 K) and ammonia (212 - 250 K). The non-toxic alternatives nitrogen (70 - 77 K), methane (124 - 146 K), ethane (188 - 200 K) and propane (200 - 250 K) were suggested for the toxic working fluids. Furthermore, the warm-end temperature and the maximum attainable high pressure appear not to play a role in the selection of the most suitable working fluid.

A second generation of JT cold stages was designed and fabricated for cooling small optical detector arrays, consisting of a high cooling-power and a low cooling-power cold stage. Experiments were done to characterize these JT cold stages. Temperature profiles along the length of the CFHX of both types of miniature JT cold stage were measured

as well as their cooling powers. The JT cold stages were operated with nitrogen at a low pressure of 6 bar. At a high pressure of 90 bar, the low cooling-power cold stage cooled down in about 90 minutes to 96 K. The measured net cooling power was 26 mW at a mass-flow rate of 3.4 mg s^{-1}. The high cooling-power cold stage was operated at a high pressure of 80 bar and cooled down in 7 minutes to 101 K. At a mass-flow rate of 15.6 mg s^{-1}, a net cooling power of 131 mW was measured. In contrast to our expectations, no isothermal two-phase region was formed in the evaporator. Between two temperature sensors placed on both ends of the evaporator, a temperature difference of 40 K was measured for the high cooling-power cold stage and a difference of 14 K for the low cooling-power cold stage. Furthermore, it was observed that droplets flowed into the CFHX.

A theoretical analysis was developed to investigate whether a JT cold stage can be driven by different working fluids. This analysis is based on the critical elements of a JT cold stage in terms of its thermodynamic performance, which are the CFHX and the flow restriction. The analysis was performed for both types of JT cold stages. It was concluded that both cold stages can be operated with the most suitable working fluids listed above and thus are applicable in the temperature range 65 - 250 K. This analysis was verified by experiments in which both cold stages were operated with methane at a low pressure of 4 bar. At a high pressure of 65 bar, the low cooling-power cold stage cooled down in 10 minutes to 135 K. The high cooling-power cold stage was operated at a high pressure of 50 bar and cooled down in 4 minutes to 138 K. Unfortunately, it was not possible to measure the cooling powers of the JT cold stages that were operated with methane, because clogging was occurring while supplying heat to the cold tip. An overview of the measurement results of all JT cold stages is given in Table 7.1.

Also, the performance of miniature JT cold stages cooling a (dummy) detector

Table 7.1: Summary of the measurement results of the second generation of JT cold stages.

Parameter	**High cooling-power cold stage**		**Low cooling-power cold stage**	
Fluid	nitrogen	methane	nitrogen	methane
High pressure (bar)	80	50	90	65
Low pressure (bar)	6	4	6	4
Cold-tip temperature (K)	103	138	101	135
Cool-down time (min)	7	4	90	10
Mass-flow rate (mg s^{-1})	15.6	4.9	3.7	0.75 [a]
Net cooling power (mW)	131	- [a]	21	8 [a]

[a] clogging occured while heating

Table 7.2: Overview of the measurement results of the second generation of JT cold stages cooling a dummy detector array.

Parameter	**High cooling-power cold stage**		**Low cooling-power cold stage**	
Fluid	nitrogen	methane	nitrogen	methane
High pressure (bar)	80	45	90	65
Low pressure (bar)	6	4	6	4
Cold-tip temperature (K)	106	144	106	138
Cool-down time (min)	11	11	70	20
Mass-flow rate (mg s^{-1})	14.6	3.7	2.7	1.1
Net cooling power (mW)	133	110	6	28

array was measured. A silicon slice covered with a thin layer of gold was used as a dummy detector and glued to the cold tip of the cold stage with conducting silver paint. Measurements were done on the high cooling-power cold stage and the low cooling-power cold stage with nitrogen and methane. Table 7.2 gives an overview of the measured properties for each type of JT cold stage. The table shows that the high cooling-power cold stage operated with nitrogen and methane in both cases has sufficient cooling power to cool detector arrays that have a power dissipation of 30 mW and require about 50 electrical connections to their warm-end electronics. The low cooling-power cold stage operated with methane can only be used for cooling detector arrays that have a power dissipation of a few milliwatts and require very few electrical connections. Operated with nitrogen, the low cooling-power cold stage has not enough cooling power to cool a detector array at all.

During the characterization it was observed that a temperature difference exists over the evaporator and that droplets flow into the CFHX. These droplets should be kept in the evaporator, where they can be evaporated by the heat load coming from the device to cool. Therefore, another design of the evaporator should be made. This design has to fit into the manufacturing process of the cold stages. For example, a herringbone structure of walls can be made into the evaporator. The walls will block the flow in such a way that there is not a direct path into the CFHX. The fluid has to flow through the structure. Such a structure will be included into a new run of miniature JT cold stages.

A disadvantage of the miniature JT cold stages is that the mass-flow rate at room temperature is very low. As shown in the measurements, the mass-flow rate increases with decreasing temperature of the restriction due to a change in density and viscosity of the fluid. It is possible that during the cool down phase, the cold stage does not cool further, while it should have enough cooling power in the case it is fully cooled down. A solution for this is to realize a tunable restriction. At room temperature, its opening should be relatively large and when the cold stage is cold the opening should be smaller.

For example, it can be investigated whether piezo elements can be used in this respect.

7.4 Closed-cycle cooling

In order to obtain closed-cycle JT cooling, a miniature JT cold stage was combined with a linear compressor of the Rutherford Appleton Laboratory. Because this compressor can deliver a relatively modest compression of 1 to 10 bar, a mixed-refrigerant is used as working fluid in the miniature JT cold stage. Based on optimizing the minimum isothermal enthalpy difference over the entire operating temperature range, a ternary mixture with a composition of 39 mol% methane, 20 mol% ethane and 41 mol% isobutane was selected that can cool to about 150 K.

The performance of the linear compressor operating with the selected mixed-refrigerant was mapped. A compression of 1.5 to 10.7 bar was obtained at zero mass-flow rate. At a mass-flow rate of 25 mg s^{-1}, a compression of 2.2 to 8.9 bar was measured. The compressor was combined with the high cooling-power JT cold stage. The JT cold stage could not cool down to below 284 K due to the low mass-flow rate of 0.16 mg s^{-1}, resulting in a too low cooling power. During the cool down phase, the mass-flow rate did not increase as is the case with pure fluids. It, therefore, did not have sufficient cooling power to fully cool down the cold stage.

In a new run of miniature JT cold stages, a cold stage is designed to operate with the selected gas mixture. The mass-flow rate will be around 1 mg s^{-1} at room temperature, resulting in a gross cooling power of about 70 mW.

APPENDIX A

Characteristics of photon detector arrays

In 2010, a literature survey among the photon detector arrays offered by the major manufacturers (E2V, Raytheon, Sofradir, Sensor Inc., Teledyne and XenICs) was performed to identify their cooler needs. In this appendix, the main characteristics that are relevant for cooling are listed. The characteristics are based on the information that is given on the websites of these manufacturers.

Table A.1: Main characteristics of photon detector arrays offered by E2V Technologies [52]. All these arrays are made of silicon and have a monolithic structure.

Series	Size/architecture (pixels x pixels)	Pixel pitch (μm x μm)	Spectral range (μm)	Operating temperature (K)	Power dissipation (mW)	Output rate (outputs) (MHz)	Electric connections (pins)
Full frame							
CCD30-11	1024 x 256 /CCD	26 x 26	200 - 1060	233	-	5	15
CCD42-40	2048 x 2048 /CCD	13.5 x 13.5	200 - 1060	243	-	-	-
CCD42-80	2048 x 4096 /CCD	13.5 x 13.5	200 - 1060	173	-	-	-
CCD47-10	1024 x 1024 /CCD	13 x 13	400 - 1100	273	-	-	-
CCD50-20	770 x 1152 /CCD	22.5 x 22.5	200 - 1100	253	-	-	-
CCD50-30	1252 x 1152 /CCD	22.5 x 22.5	420 - 1060	253	-	-	-
CCD77-00	512 x 512 /CCD	24 x 24	400 - 1060	273	-	-	-
CCD203-82	4096 x 4096 /CCD	12 x 12	300 - 1060	173	185 - 1125	3 (4)	2 x 37
CCD230-42	2048 x 2048 /CCD	15 x 15	300 - 1060	248	200 - 1000	5 (4)	2 x 39
CCD230-42	2048 x 2048 /CCD	15 x 15	420 - 1060	248	176 - 1025	5 (4)	78
TH7899M	2048 x 2048 /CCD	14 x 14	400 - 1100	233 - 300	-	20 (4)	82
Scientific							
CCD39-02	80 x 80 /CCD	24 x 24	200 - 1100	243	-	-	-
CCD48-20	1024 x 1024 /CCD	13 x 13	200 - 1100	243	-	-	-
TH7891M	1024 x 1024 /CCD	17 x 17	400 - 900	218 - 300	70	6 (1)	-
CIS101	1415 x 1430 /CMOS	17.81 x 11.53	400 - 900	293	50	-	107
L3Vision							
CCD60	128 x 128 /CCD	24 x 24	400 - 900	153 - 300	-	-	24
CCD65	576 c 288 /CCD	20 x 30	400 - 1060	153 - 300	-	-	36
CCD97	512 x 512 /CCD	16 x 16	400 - 1060	218 - 300	-	11 (2)	30
CCD201-20	1024 x 1024 /CCD	13 x 13	400 - 900	223	-	15 (2)	36

Table A.2: Main characteristics of photon detector arrays offered by Raytheon [53].

Series	**Detector material**	**Size/architecture*** (pixels x pixels)	**Pixel pitch** (μm x μm)	**Spectral range** (μm)	**Operating temperature** (K)	**Power dissipation** (mW)	**Output rate (outputs)** (MHz)
Aquarius	Si:As IBC	1024 x 1024 /H	30 x 30	5 - 28	8 - 10	35 or 100	3 (16 or 64)
Orion	InSb	2048 x 2048 /H	25 x 25	0.6 - 5.4	30	-	- (64)
Virgo	HgCdTe	2048 x 2048 /H	20 x 20	0.85 - 2.5	70 - 80	10	- (4 or 16)
Iris	InSb	512 x 412 /H	30 x 30	1 - 5	15 - 30	-	- (6)
	Si:As IBC	512 x 412 /H	30 x 30	1 - 28	4 - 10	-	- (6)
Aladin III	InSb	1024 x 1024 /H	27 x 27	1 - 5	30 - 35	-	- (32)
AE 194	InSb	128 x 128 /H	30 x 30	3 - 5	78	< 20	5 (2)
AE 195	InSb	384 x 256 /H	25 x 25	3 - 5	78	< 65	5 (2)
AE 197	InSb	640 x 512 /H	25 x 25	3 - 5	78	< 120	10 (1, 2 or 4)
SB339	HgCdTe	1280 x 1024 /H	20 x 20	0.9 - 1.7	250	50 - 250	11 (2, 4 or 64)
	HgCdTe	1280 x 1024 /H	20 x 20	0.9 - 2.5	120	50 - 250	11 (2, 4 or 64)
SB347	HgCdTe	260 x 256 /H	40 x 40	7 - 12.5	40 - 50	< 200	6 (6)
Osprey	Si PIN	2048 x 2048 /M	10 x 10	0.4 - 1.1	273 - 300	-	-
SDA	InSb	640 x 480 /H	20 x 20	3 - 5	78	< 20	5 (2)
SB240	InSb	1024 x 1024 /H	20 x 20	3 - 5	-	120	20 (16)
AE187	InSb	512 x 512 /H	25 x 25	3 - 5	80	< 45	5 (4)

* H=Hybrid, M=Monolithic

Table A.3: Main characteristics of photon detector arrays manufactured by Sensor Inc. [54].

Series	**Detector material**	**Size/architecture*** (pixels x pixels)	**Pixel pitch** (μm x μm)	**Spectral range** (μm)	**Operating temperature** (K)	**Power dissipation** (mW)
LD/LDB/LSB	InGaAs	1 x 512 /H	25 x 25	0.8 - 1.7	253 - 300	150
S41024LE	InGaAs	1 x 1024 /H	25 x 25	0.8 - 1.7	-	-
LC	InGaAs	1 x 256 /H	25 x 25	1.0 - 2.6	223	-
	InGaAs	128 x 128 /H	60 x 60	0.9 - 1.7	300	-
	InGaAs	320 x 320 /H	40 x 40	0.9 - 1.7	300	-

* H=Hybrid, M=Monolithic

Table A.4: Main characteristics of photon detectors that are offered by Sofradir [55].

Series	**Detector material**	**Size/architecture*** (pixels x pixels)	**Pixel pitch** (μm x μm)	**Spectral range** (μm)	**Operating Temperature** (K)	**Output rate (outputs)** (MHz)
Epsilon	HgCdTe	384 x 288 /H	15 x 15	3.4 - 4.8	100 - 110	17 (1)
Jupiter	HgCdTe	1280 x 1024 /H	15 x 15	3.7 - 4.8	77 - 110	20 (4 or 8)
Mars	HgCdTe	320 x 256 /H	30 x 30	0.8 - 2.0/2.5	250 / 200	3 (4)
	HgCdTe	320 x 256 /H	30 x 30	3.7 - 4.8	80 - 110	6.6 (1 or 4)
	HgCdTe	320 x 256 /H	30 x 30	7.7 - 11	70 - 77	6.6 (1 or 4)
Mercury	HgCdTe	480 x 6 /H	50 x 25	7.7 - 10.3	77 - 90	5 (16)
Neptune	HgCdTe	500 x 256 /H	30 x 30	0.8 - 2.5	200	8 (2 or 4)
Pluton	HgCdTe	288 x 4 /H	28 x 43	7.7 - 10.3	77 - 90	6 (4)
Saturn	HgCdTe	1000 x 256 /H	30 x 30	0.8 - 2.5	< 200	5 (4 or 8)
Scorpio	HgCdTe	640 x 512 /H	15 x 15	3.7 - 4.8	90 - 110	5 (4)
Sirius	AlGaAs QWIP	640 x 512 /H	20 x 20	8 - 9 ($\lambda_{peak} = 8.5$)	70 - 75	8 (1, 2 or 4)
Uranus	HgCdTe	640 x 512 /H	20 x 20	3.7 - 4.8	80 - 110	6 (4)
Vega	AlGaAs QWIP	384 x 288 /H	25 x 25	8 - 9 ($\lambda_{peak} = 8.5$)	73	5 (1, 2 or 4)
Venus	HgCdTe	384 x 288 /H	25 x 25	7.7 - 9.5	77 - 80	5 (1 or 4)

* H=Hybrid, M=Monolithic

Table A.5: Main characteristics of photon detector arrays of Teledyne [56].

Series	**Detector material**	**Size/architecture*** (pixels x pixels)	**Pixel pitch** (μm x μm)	**Spectral range** (μm)	**Operating temperature** (K)	**Power dissipation** (mW)	**Output rate (outputs)** (MHz)
Picnic	HgCdTe	256 x 256 /H	40 x 40	0.9 - 2.5	77	-	0.25 (4)
Hawaii-2RG	HgCdTe	2048 x 2048 /H	18 x 18	0.4 - 1.7	140	< 0.5	0.1 - 5 (1,4 or 32)
	HgCdTe	2048 x 2048 /H	18 x 18	0.4 - 2.5	77	< 0.5	0.1 - 5 (1,4 or 32)
	HgCdTe	2048 x 2048 /H	18 x 18	0.4 - 5.4	40	< 0.5	0.1 - 5 (1,4 or 32)
TCM6604A	Si PIN	640 x 480 /H	27 x 27	0.2 - 1.1	150 - 200	< 70	8 (4)
TCM8050A	Si PIN	1024 x 1024 /H	18 x 18	0.2 - 1.1	150 - 200	< 100	6 (4)
H4RG-10	Si PIN	4096 x 4096 /H	10 x 10	0.2 - 1.1	150 - 200	< 16	0.1 - 5 (1,4,16,32 or 64)
V1M	Si PIN	1280 x 1280 /H	14 x 14	0.4 - 1.1	150 - 200	200	-

* H=Hybrid, M=Monolithic

Table A.6: Main characteristics of photon detector arrays manufactured by XenICs [57].

Series	**Detector material**	**Size/architecture** * (pixels x pixels)	**Pixel pitch** (μm x μm)	**Spectral range** (μm)	**Operating temperature** (K)	**Output rate** (MHz)
Xlin	InGaAs	1 x 512, 1 x 256, 1 x 512 /H	50, 50, 25	0.9 - 1.7	263	2.5
	InGaAs	1 x 512, 1 x 256, 1 x 512 /H	50, 50, 25	1.0 - 2.2	243	2.5
	InGaAs	1 x 512, 1 x 256, 1 x 512 /H	50, 50, 25	1.1 - 2.5	223	2.5
Cheetah	InGaAs	640 x 512 /H	20 x 20	0.9 - 1.7	263	-
Xeva	InGaAs	320 x 256, 640 x 512 /H	30 x 30, 20 x 20	0.9 - 1.7	263	-
	HgCdTe	320 x 256 /H	30 x 30	0.85 - 2.5	200	-
Xmid	InSb	320 x 256, 640 x 256 /H	30 x 30, 20 x 20	3 - 5	80	2.5

* H=Hybrid, M=Monolithic

APPENDIX *B*

Fluid and glass properties

In this appendix, the properties of nitrogen and methane as a function of temperature and pressure are given. This fluid data was taken from Refprop [74]. Furthermore, the thermal conductivity and specific heat as a function of the temperature of glass are shown that was taken from MPDB [102].

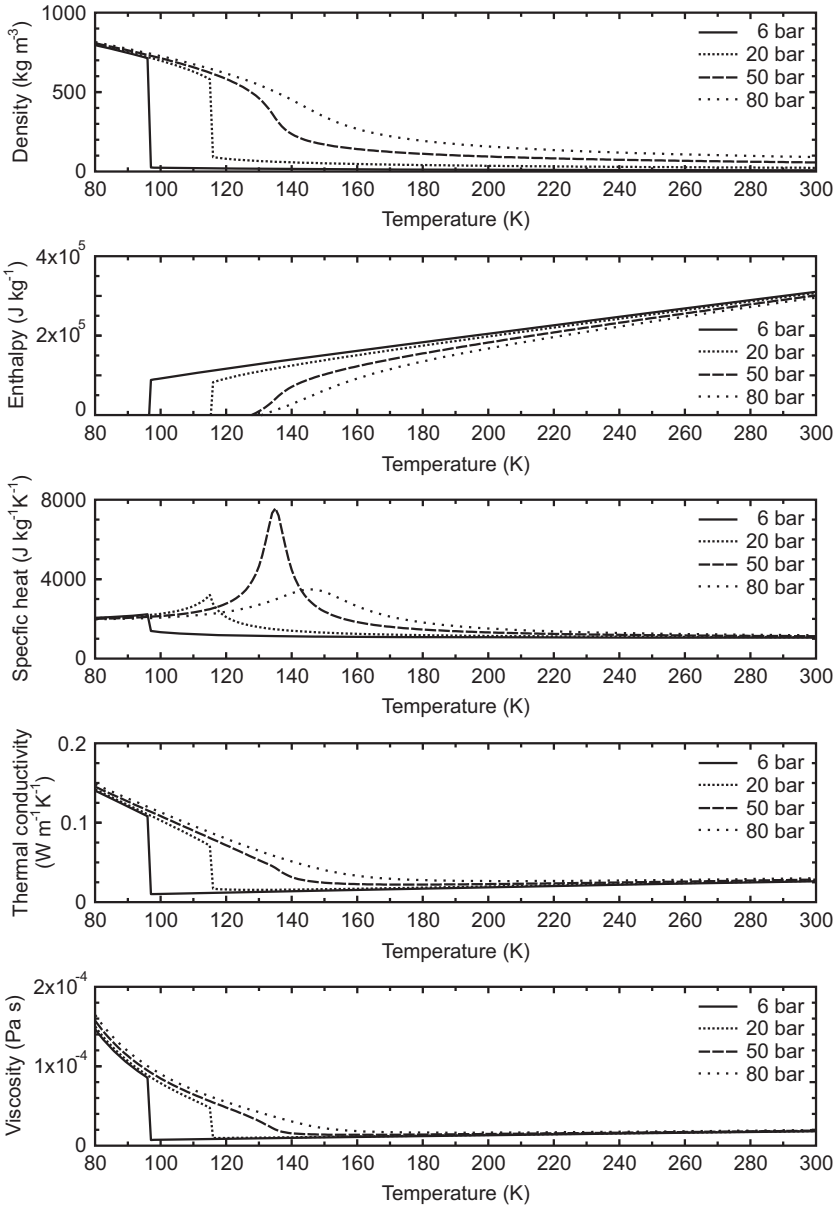

Figure B.1: Fluid properties of nitrogen as a function of temperature and pressure. Taken from Refprop [74].

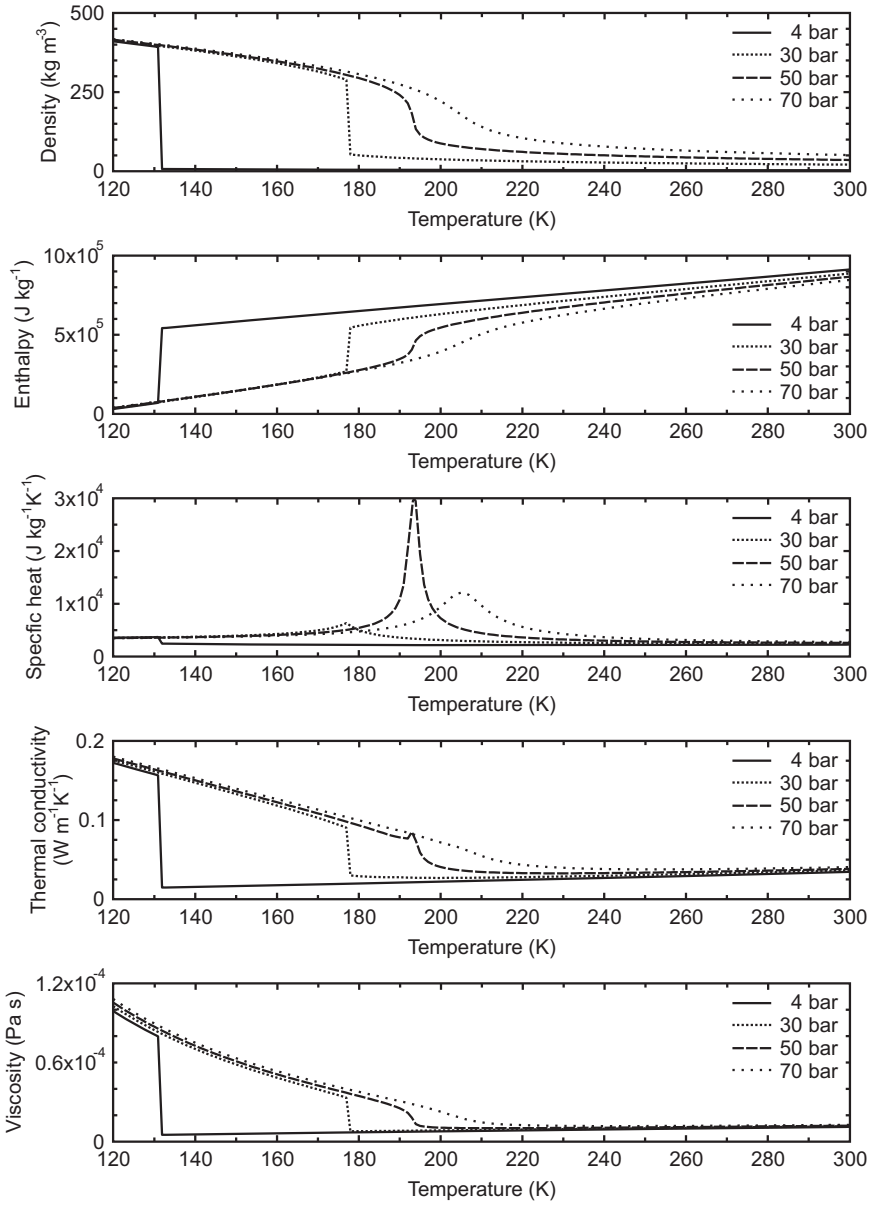

Figure B.2: Fluid properties of methane as a function of temperature and pressure. Taken from Refprop [74].

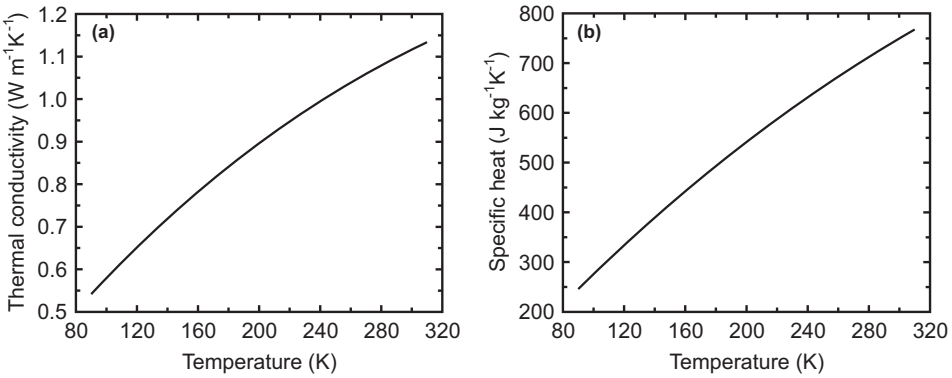

Figure B.3: a) Thermal conductivity and b) specific heat versus the temperature for glass. Taken from MPDB [102].

Bibliography

[1] H.J.M. ter Brake, *Cryogenic systems for superconducting devices*, In: Applications of Superconductivity, 561–639, Kluwer Academic Publishers, ISBN: 0-7923-6113-X (2000).

[2] B.Z. Maytal, G.F. Nellis, S.A. Klein and J.M. Pfotenhauer, *Elevated-pressure mixed-coolants Joule-Thomson cryocooling*, Cryogenics **46**, 55-67 (2006).

[3] G. Walker, R. Fauvel and G. Reader, *Miniature refrigerators for cryogenic sensors and cold electronics*, Cryogenics **29**, 841–845 (1989).

[4] R. Radebaugh, *Recent developments in cryocoolers*, In: Proc. 19th Int. Congr. Refrig. **IIIb**, 973–989 (1995).

[5] P.P.P.M. Lerou, G.C.F. Venhorst, C.F. Berends, T.T. Veenstra, M. Blom, J.F. Burger, H.J.M. ter Brake and H. Rogalla, *Fabrication of a micro cryogenic cold stage using MEMS-technology*, J. Micromech. Microeng. **16**, 1919–1925 (2006).

[6] S. Garvey, S. Logan, R. Rowe and W.A. Little, *Performance characteristics of a low-flow rate 25 mW, LN_2 Joule-Thomson refrigerator fabricated by photolithographic means*, Appl. Phys. Lett. **42**, 1048–1050 (1983).

[7] W.A. Little, *Microminiature refrigeration*, Rev. Sci. Instrum. **55**, 661–680 (1984).

[8] R.L. Paugh, *New class of microminiature Joule - Thomson refrigerator and vacuum package*, Cryogenics **30**, 1079–1083 (1990).

[9] E. Bodio, M. Chorowski, M. Wilczek and A. Bozek, *Miniature Joule - Thomson liquefier with sintered heat exchanger*, Cryogenics **32**, 13–16 (1992).

[10] E. Mikulin, J. Shevich, T. Danilenko, N. Solovov and V. Veselov, *The miniature Joule-Thomson refrigerator*, Cryogenics **32**, 17–19 (1992).

[11] H.J. Holland, J.F. Burger, N. Boersma, H.J.M. ter Brake and H. Rogalla, *Miniature 10-150 mW Linde-Hampson cooler with glass-tube heat exchanger operating with nitrogen*, Cryogenics **38**, 407–410 (1998).

[12] J. Burger, H. Holland, J. Seppenwoolde, E. Berenschot, H. ter Brake, J. Gardeniers, M. Elwenspoek and H. Rogalla, *165 K microcooler operating with a sorption compressor and a micromachined cold stage*, Cryocoolers **11**, 551–560, Kluwer Academic / Plenum Publishers (2001).

[13] H. Xue, K.C. Ng and J.B. Wang, *Performance evaluation of the recuperative heat exchanger in a miniature Joule-Thomson cooler*, Appl. Therm. Eng. **21**, 1829–1844 (2001).

[14] K.C. Ng, H. Xue and J.B. Wang, *Experimental and numerical study on a miniature Joule-Thomson cooler for steady-state characteristics*, Int. J. Heat Mass Transfer **45**, 609–618 (2002).

[15] S. Jeong, *How difficult is it to make a micro refrigerator?*, Int. J. Refrig. **27**, 309–313 (2004).

[16] L.Y. Xiong, G. Kaiser and A. Binneberg, *Theoretical study on a miniature Joule-Thomson & Bernoulli cryocooler*, Cryogenics **44**, 801–807 (2004).

[17] Y.J. Hong, S.J. Park, H.B. Kim and Y.D. Choi, *The cool-down characteristics of a miniature Joule-Thomson refrigerator*, Cryogenics **46**, 391–395 (2006).

[18] H.T. Chua, X. Wang and H.Y. Teo, *A numerical study of the Hampson-type miniature Joule-Thomson cryocooler*, Int. J. Heat Mass Transfer **49**, 582–593 (2006).

[19] J. Yu, *Improving the performance of small Joule-Thomson cryocooler*, Cryogenics **48**, 426–431 (2008).

[20] M.H. Lin, P.E. Bradley, H.J. Wu, J.C. Booth, R. Radebaugh and Y.C. Lee, *Design, fabrication, and assembly of a hollow-core fiber-based micro cryogenic cooler*, In: Transducers 2009, 1114–1117 (2009).

[21] J.F. Burger, *Cryogenic microcooling, a micromachined cold stage operating with a sorption compressor in a vapor compression cycle*, PhD thesis, University of Twente, Enschede, The Netherlands, ISBN: 90-365-1536-X (2001),<doc.utwente.nl/23470/>.

[22] P.P.P.M. Lerou, *Micromachined Joule-Thomson cryocooler*, PhD thesis, University of Twente, Enschede, The Netherlands, ISBN: 90-365-2458-X (2007),<doc.utwente.nl/57770/>.

[23] P.P.P.M. Lerou, H.J.M. ter Brake, J.F. Burger, H.J. Holland and H. Rogalla, *Characterization of micromachined cryogenic coolers*, J. Micromech. Microeng. **19**, 1956–1960 (2007).

[24] P.P.P.M. Lerou, T.T. Veenstra, J.F. Burger, H.J.M. ter Brake and H. Rogalla, *Optimization of counterflow heat exchanger geometry through minimization of entropy generation*, Cryogenics **45**, 659–669 (2005).

[25] M.H. Lin, P.E. Bradley, M.L. Huber, R. Lewis, R. Radebaugh and Y.C. Lee, *Mixed refrigerants for a glass capillary micro cryogenic cooler*, Cryogenics **50**, 439–442 (2010).

[26] P. Bhandari, M. Prina, R.C. Bowman Jr., C. Paine, D. Pearson and A. Nash, *Sorption coolers using a continuous cycle to produce 20 K for the Planck flight mission*, Cryogenics **44**, 395–401 (2004).

[27] J.F. Burger, H.J.M. ter Brake, H. Rogalla and M. Linder, *Vibration-free 5 K sorption cooler for ESA's Darwin mission*, Cryogenics **42**, 97–108 (2002).

[28] R. Levenduski and R. Scarlotti, *Joule-Thomson cryocooler for space applications*, Cryogenics **36**, 859–866 (1996).

[29] G.F.M. Wiegerinck, J.F. Burger, H.J. Holland, E. Hondebrink, H.J.M. ter Brake and H. Rogalla, *A sorption compressor with a single sorber bed for use with a Linde-Hampson cold stage*, Cryogenics **46**, 9–20 (2006).

[30] W. Chen and M. Zagarola, *Vibration-free Joule-Thomson cryocoolers for distributed microcooling*, Cryocoolers **15**, 433-440, Boulder CO: ICC Press (2009).

[31] A. Rogalski, *Optical detectors for focal plane arrays*, Opto-Electron. Rev. **12**, 221–245 (2004).

[32] G. Rieke, *Detection of Light*, Cambridge University Press, ISBN: 0-521-01710-6 (2003).

[33] J.M. Liu, *Photonic devices*, Cambridge University Press, ISBN: 0-521-55195-1 (2005).

[34] P.R. Norton, *Infrared image sensors*, Opt. Eng. **30**, 1649–1663 (1991).

[35] R.E. McMurray Jr, *Infrared detector requirements which drive cryogenic development*, Cryogenics **34**, 425–429 (1994).

[36] A.L. Woodcraft, *Detectors for sub-millimetre continuum astronomy*, Nucl. Instrum. Methods Phys. Res. A **604**, 30–33 (2009).

[37] A. Rogalski, *Infrared detectors: status and trends*, Prog. Quantum Electron. **27**, 59–210 (2003).

[38] A.L. Woodcraft et al., *Electrical and optical measurements on the first SCUBA-2 prototype 1280 pixel submillimeter superconducting bolometer array*, Rev. Sci. Instrum. **78**, 024502-1-7 (2007).

[39] A. Poglitsch et al., *The photodetector array camera and spectrometer (PACS) on the Herschel space observatory*, Astron. Astrophys. **518**, L2-1-12 (2010).

[40] J.H. Derking, H.J.M. ter Brake, A. Sirbi, M. Linder and H. Rogalla, *Optimization of the working fluid in a Joule-Thomson cold stage*, Cryogenics **49**, 151–157 (2009).

[41] P. Magnam, *Detection of visible photons in CCD and CMOS: A comparative view*, Nucl. Instrum. Methods Phys. Res. A **504**, 199–212 (2003).

[42] D.H. Lumb, N. Rando, A. Peacock, F. Favata and M.A.C. Perryman, *Focal plane cameras for ESA optical astronomy missions*, Nucl. Instrum. Methods Phys. Res. A **513**, 112–117 (2003).

[43] G.D. Mackay, *Charge-coupled devices in astronomy*, Ann. Rev. Astron. Astrophys. **24**, 255-283 (1986).

[44] B. Burke, P. Jorden and P. Vu, *CCD technology*, In: Scientific detectors for astronomy 2005, 225–264, Springer Netherlands, ISBN: 978-1-4020-4329-1 (2005).

[45] M. Clampin, D. Lumb, M. Sirianni and E. Smith, *Detectors for space science*, Exp. Astron. **19**, 45–67 (2005).

[46] A. El Gamal and H. Eltoukhy, *CMOS image sensors*, IEEE Circuits Devices Mag. **21**, 6–20 (2005).

[47] E.R. Fossum, *CMOS image sensors: electronic camera-on-a-chip*, IEEE Trans. Electron Devices **44**, 1689–1698 (1997).

[48] A. Hoffman, M. Loose and V. Suntharalingam, *CMOS detector technology*, Exp. Astron. **19**, 111–134 (2005).

[49] P.R. Norton, *Infrared sensors in spacecraft that monitor planet Earth*, Opto-Electron. Rev. **16**, 105–117 (2008).

[50] A. Rogalski, *Infrared detectors: an overview*, IR Phys. Technol. **43**, 187–210 (2002).

[51] J.W. Beletic, R. Blank, D. Gulbransen, D. Lee, M. Loose, E.C. Piquette, T. Sprafke, W.E. Tennant, M. Zandian and J. Zino, *Teledyne imaging sensors: infrared imaging technologies for astronomy and civil space*, In: Proc. SPIE **7021**, 70210H–14 (2008).

[52] E2V Technologies, Chelmsford, Engeland, <www.e2v.com>.

[53] Raytheon Company, Waltham, MA, USA, <http://www.raytheon.com/>.

[54] Sensors Unlimited Inc., Part of Goodrich Corporation, Princeton, NJ, USA, <http://www.sensorsinc.com/arrays.html>.

[55] Sofradir, 92290 Chatenay-Malabry, France, <www.sofradir.com>.

[56] Teledyne Technologies Inc., Thousand Oaks, CA, USA, <www.teledyne-si.com>.

[57] Xenics infrared solutions, Leuven, Belgium, <www.xenics.com>.

[58] O. Yadid-Pecht, B. Pain, C. Staller, C. Clark and E. Fossum, *CMOS active pixel sensor star tracker with regional electronic shutter*, IEEE J. Solid-State Circ. **32**, 285–288 (1997).

[59] J. Leijtens, *Sunsensor miniaturization where is the end?*, In: IEEE Sensors 2008, 1348–1351 (2008).

[60] M. Clampin, *Ultraviolet-optical charge-coupled devices for space instrumentation*, Opt. Eng. **41**, 1185–1191 (2002).

[61] R.W.M. Hoogeveen, R.J. van der A and A.P.H. Goede, *Extended wavelength InGaAs infrared (1.0-2.4 µm) detector arrays on SCIAMACHY for space-based spectrometry of the Earth atmosphere*, IR Phys. Techn. **42**, 1–16 (2001).

[62] M.H. Ettenberg, M.J. Lange, M.T. O'Grady, J.S. Vermaak, M.J. Cohen and G.H. Olsen, *Room temperature 640x512 pixel near-infrared InGaAs focal plane array*, In: Proc. SPIE **4028**, 201–207 (2000).

[63] A. Rogalski, *HgCdTe infrared detector material: history, status and outlook*, Rep. Prog. Phys. **68**, 2267–2236 (2005).

[64] P. Norton, *HgCdTe Infrared detectors*, Opto-Electron. Rev. **10**, 159–174 (2002).

[65] A.W. Hoffman, P.J. Love and J.P. Rosbeck, *Megapixel detector arrays: visible to 28 µm*, In: Proc. SPIE **5167**, 194–212 (2004).

[66] E. Costarda, P. Boisa, A.D. Rossia, A. Nedelcua, O. Cocleb, F.H. Gauthierb and F. Audierb, *QWIP detectors and thermal imagers*, C.R. Phys. **4**, 1089–1102 (2003).

[67] S.D. Gunapala, S.V. Bandara, J.K. Liu, C.J. Hill, S.B. Rafol, J.M. Mumolo, J.T. Trinh, M.Z. Tidrow and P.D. LeVan, *1024 x 1024 pixel mid-wavelength and long-wavelength infrared QWIP focal plane arrays for imaging applications*, Semicond. Sci. Technol. **20**, 473-480 (2005).

[68] M. Jhabvalaa, K.K. Choib, C. Monroyb and A. Laa, *Development of a 1K x 1K, 812 µm QWIP array*, IR Phys. Technol. **50**, 234–239 (2007).

[69] W.A. Little, *Advances in Joule-Thomson cooling*, Adv. Cryog. Eng. **35**, 1305–1314, Plenum Press, New York (1990).

[70] A. Bejan, *Heat transfer*, John Wiley & Sons, ISBN: 0-471-50290-1 (1993).

[71] S.M. Marco and L.S. Han, *A note on limiting laminar Nusselt number in ducts with constant temperature gradient by analogy to thin-plate theory*, Trans. ASME **77**, 625–630 (1955).

[72] C.K. Hsieh and K.C. Su, *Thermal radiative properties of glass from 0.32 to 206 µm*, Solar Energy **22**, 37–43 (1979).

[73] A. Bendavida, P.J. Martina and L. Wieczorekb, *Morphology and optical properties of gold thin films prepared by filtered arc deposition*, Thin Solid Films **354**, 169–175 (1999).

[74] E.W. Lemmon and M.L. Huber and McLinder MO, *Refprop version 8.0*, NIST standard reference database 23, <http://www.nist.gov/srd/nist23.htm>.

[75] Air Liquide, Paris, France, <http://encyclopedia.airliquide.com>.

[76] J. Lester, *Closed cycle hybrid cryocooler combining the Joule-Thomson cycle with thermoelectric coolers*, Adv. Cryog. Eng. **35**, 1335–1340, Plenum Press, New York (1990).

[77] ESATAN-TMS^{TM}, ITP Engines UK, <www.itp-enginesuk.com/>.

[78] Cryocomp v3.01, Cryodata Inc, Eckels engineering, Florence SC, USA.

[79] Schott AG, Mainz, Germany, <www.schott.com>.

[80] M. Elwenspoek and H.V. Jansen, *Silicon micromachining*, Cambridge University Press, ISBN: 0-521-59054-X (1998).

[81] T.R. Hsu, *MEMS packaging*, Inspec, London, ISBN: 0-86341-335-8 (2004).

[82] J. Haisma, B.A.C.M. Spierings, U.K.P. Biermann and A.A. van Gorkum, *Diversity and feasibility of direct bonding: a survey of a dedicated optical technology*, Appl. Opt. **33**, 1154–1168 (1994).

[83] Z.X. Xiao, G.Y. Wu, Z.H. Li, G.B. Zhang, Y.L. Hao and Y.Y. Wang, *Silicon-glass wafer bonding with silicon hydrophilic fusion bonding technology*, Sens. Act. A **72**, 46–48 (1999).

[84] L. Lin, *MEMS post-packaging by localized heating and bonding*, IEEE Trans. Adv. Packag. **23**, 608–616 (2000).

[85] V. Lehmann, K. Mitani, R. Stengl, T. Mii and U. Gösele, *Bubble-free wafer bonding of GaAs and InP on silicon in a microcleanroom*, Jpn. J. Appl. Phys. **28**, L2141 - L2143 (1989).

[86] W.B. Choi, B.K. Ju, Y.H. Lee, M.H. Oh, N.Y. Lee and M.Y. Sung, *Silicon-to-indium tin oxide coated glass bonding for packaging of field emission arrays fabricated on silicon wafer*, J. Mat. Sci. **34**, 4711–4717 (1999).

[87] M.T. Blom, E. Chmela, J.G.E. Gardeniers, J.W. Berenschot, M. Elwenspoek, R. Tijssen and A. van den Berg, *Local anodic bonding of Kovar to Pyrex aimed at high-pressure, solvent-resistant microfluidic connections*, J. Micromech. Microeng. **11**, 382-385 (2001).

[88] P. Knapkiewicz, R. Walczak and J.A. Dziuban, *The method of integration of silicon micromachined sensors and actuators to microreactor made of Foturan® glass*, Optica Applicata **37**, 65–72 (2007).

[89] P. Krause, M. Sporys, E. Obermeier, K. Lange and S. Grigull, *Silicon to silicon anodic bonding using evaporated glass*, In: Transducers '95, 228–231 (1995).

[90] M. Esashia, A. Nakanoa, S.I. Shojia and H. Hebiguchia, *Low-temperature silicon-to-silicon anodic bonding with intermediate low melting point glass*, Sens. Act. A **23**, 931-934 (1990).

[91] Y.T. Cheng, L. Lin and K. Najafi, *Fabrication and hermeticity testing of a glass-silicon package formed using localized aluminum/silicon-to-glass bonding*, In: IEEE MEMS 2000, 757–762 (2000).

[92] Y. Cheng, L. Lin and K. Najafi, *Localized bonding with PSG or indium solder as intermediate layer*, In: IEEE MEMS 1999, 285–289 (1999).

[93] E.R. Murphy, T. Inoue, H.R. Sahoo, N. Zaborenkoa and K. Jensen, *Solder-based chip-to-tube and chip-to-chip packaging for microfluidic devices*, Lab Chip **7**, 1309–1314 (2007).

[94] W.J. Greig, *Integrated circuit packaging, assembly and interconnections*, Springer, New York, ISBN: 978-0-387-33913-9 (2007).

[95] A. Singh, D.A. Horsley, M.B. Cohn, A.P. Pisano and R.T. Howe, *Batch transfer of microstructures using flip-chip solder bonding*, IEEE J. MicroElectoMech. Syst. **8**, 27–33 (1999).

[96] Indium Corporation, Clinton, NY, USA, <www.indium.com>.

[97] S.E. Shoaf and A.D. Feinerman, *Aligned AuSi eutectic bonding of silicon structures*, J. Vac. Sci. Technol. A **12**, 19–22 (1994).

[98] L.A. Fielda and R.S. Mullera, *Fusing silicon wafers with low melting temperature glass*, Sens. Act. A **23**, 935-938 (1990).

[99] R. Legtenbergt, S. Bouwstra and M. Elwenspoek, *Low-temperature glass bonding for sensor applications using boron oxide thin films*, J. Micromech. Microeng. **1**, 157–160 (1991).

[100] F. Niklaus, G. Stemme, J.Q. Lu and R.J. Gutmann, *Adhesive wafer bonding*, J. Appl. Phys. **99**, 031101 (2006).

[101] B.G. Yacobia, S. Martin, K. Davis, A. Hudson and M. Hubert, *Adhesive bonding in microelectronics and photonics*, J. Appl. Phys. **91**, 6227–6262 (2002).

[102] MPDB v6.60, JAHM software Inc., North Reading, MA, USA, <www.jahm.com>.

[103] Pyrex®, Corning Inc., Corning, NY, USA, <www.corning.com>.

[104] R.R. Tummala, *Microelectronics packaging handbook part 2: semiconductor packaging*, Chapman and Hall, New York, ISBN: 0-412-08441-4 (1997).

[105] Epoxy Technology Inc, *Epo-Tek T7110*, Billerica, MA, USA, <www.epotek.com>.

[106] Emerson & Cuming, *Stycast 2850 FT*, Henkel Corporation, Düsseldorf, Germany, <www.henkel.com>.

[107] Emerson & Cuming, *Eccobond 285*, Henkel Corporation, Düsseldorf, Germany, <www.henkel.com>.

[108] Henkel Corporation, *Hysol EA9361*, Aerospace Group, Bay Point, CA, USA, <www.aerospace.henkel.com>.

[109] Master Bond Inc., *EP21TCHT-1*, Hackensack, NJ, USA, <www.masterbond.com>.

[110] NASA low outgassing database, <http://outgassing.nasa.gov>.

[111] Electrolube, *Conducting silver paint*, Wargrave, Berkshire, UK, <www.electrolube.com>.

[112] Apiezon N, Apiezon, Manchester, UK, <http://www.apiezon.com>.

[113] Lake Shore Cryotronics Inc., Westerville, OH, USA, <www.lakeshore.com>.

[114] Saes Pure Gas Inc., San Luis Obispo, CA, USA, <www.saesgetters.com>.

[115] P.P.P.M. Lerou, H.J.M. ter Brake, H.J. Holland, J.F. Burger and H. Rogalla, *Insight into clogging of micromachined cryogenic coolers*, Appl. Phys. Lett. **90**, 064102 (2007).

[116] Ansys Inc., *Fluent*, <www.fluent.com>.

[117] J.F. Burger, H.J.M. ter Brake, H.J. Holland, R.J. Meijer, T.T. Veenstra, G.C.F. Venhorst, D. Lozano-Castello, M. Coesel and A. Sirbi, *Long-life vibration-free 4.5 K sorption cooler for space applications*, Rev. Sci. Instrum. **78**, 065102 1-10 (2007).

[118] S.T. Werett, G.D. Peskett, G. Davey, T.W. Bradshaw and J. Delderfield, *Development of a small Stirling cycle cooler for spaceflight applications*, Adv. Cryog. Eng. **31**, 791–799, Plenum Press, New York (1986).

[119] T.W. Bradshaw, J. Delderfield, S.T. Werrett and G. Davey, *Performance of the Oxford miniature Stirling cycle refrigerator*, Adv. Cryog. Eng. **31**, 801–809, Plenum Press, New York (1986).

[120] A.H. Orlowska, T.W. Bradshaw and J. Hieatt, *Closed cycle coolers for temperatures below 30 K*, Cryogenics **30**, 246–248 (1990).

[121] G. Morgante, D. Pearson et al., *Cryogenic characterization of the Planck sorption cooler system flight model*, JINST **4**, T12016 (2009).

[122] S.R. Scull, B.G. Jones, T.W. Bradshaw, A.H. Orlowska and C.I. Jewell, *Design and development of a 4 K mechanical cooler*, Cryocoolers **10**, 513–519, Kluwer Academic / Plenum Publishers (1999).

[123] T.W. Bradshaw, A.H. Orlowska and C. Jewell, *Life test and performance testing of a 4 K cooler for space applications*, Cryocoolers **10**, 521–528, Kluwer Academic / Plenum Publishers (1999).

[124] W.J. Podbielniak, *Art of refrigeration*, US Patent **2.041.725**, (1936).

[125] M. Fuderer and A. Andrija, *Verfahren zur Tiefkühlung*, German Patent **1426956**, (1969).

[126] E.D. Marquardt, R. Radebaugh and J. Dobak, *A cryogenic catheter for treating heart arrhythmia*, Adv. Cryog. Eng. **43**, 903–910, Plenum Press, New York (1998).

[127] M. Boiarski, A. Khatri and O. Podcherniaev, *Enhanced refrigeration performance of the throttle-cycle coolers operating with mixed refrigerants*, Adv. Cryog. Eng. **45**, 291–297, Kluwer Academic / Plenum Publishers (2000).

[128] E.C. Luo, M. Gong, Y. Zhou, J.T. Liand and L. Zhang, *The research and development of cryogenic mixed-refrigerant Joule-Thomson cryocoolers in Cl/CAS*, Adv. Cryog. Eng. **45**, 299–306, Kluwer Academic / Plenum Publishers (2000).

[129] E. Luo, M. Gong, Y. Zhou and L. Zhang, *Experimental investigation of a mixed-refrigerant J-T cryocooler operating from 30 to 60 K*, Adv. Cryog. Eng. **45**, 315–321, Kluwer Academic / Plenum Publishers (2000).

[130] M.Q. Gong, E.C. Luo, J.F. Wu and Y. Zhou, *On the temperature distribution in the counter flow heat exchanger with multicomponent non-azeotropic mixtures*, Cryogenics **42**, 195–804 (2002).

[131] M.Q. Gong, J.F. Wu and E.G. Luo, *Performances of the mixed-gases Joule-Thomson refrigeration cycles for cooling fixed-temperature heat loads*, Cryogenics **44**, 847–857 (2004).

[132] J.M. Pfotenhauer, J.F. Pettitt, D.W. Hoch and G.F. Nellis, *Progress towards a low power mixed-gas Joule-Thomson cryocooler for electronic current leads*, Cryocoolers **14**, 443–452, Kluwer Academic, New York (2007).

[133] P.E. Bradley, R. Radebaugh, M. Huber, M. H.Lin and Y.C. Lee, *Development of a Mixed-Refrigerant Joule-Thomson Microcryocooler*, Cryocoolers **15**, 425–432, Boulder CO: ICC Press (2010).

Summary

Vibration-free miniature Joule-Thomson (JT) coolers have a high potential for cooling low-power electronic devices, such as detector arrays, low-noise amplifiers, and semi-conducting and superconducting electronics. These devices are cooled to reduce their thermal noise, to increase the bandwidth or to obtain superconductivity. In this thesis, the utilization of micromachined JT coolers for cooling small optical detector arrays for future space missions is investigated. The focus is on the use of single-stage JT coolers that can provide cooling in the temperature range of 65 - 300 K. The scope is to obtain a distributed cooling system in which multiple miniature JT cold stages, each cool a small detector array, are driven by a single compressor.

To identify the detector arrays used in space applications that can be cooled by miniature JT coolers, a literature survey was performed. This survey showed that only photon detector arrays of silicon, indium-gallium-arsenide and mercury-cadmium-telluride are suitable for cooling with single-stage JT coolers. Micromachined JT coolers are made of glass, have typical cold-tip dimensions of 10 x 10 mm^2 and net cooling powers up to 150 mW at 100 K. Based on these specifications, detector arrays can have up to 512 x 512 pixels. At a pixel pitch of 15 x 15 μm^2 this corresponds to an array size of about 10 x 10 mm^2 equal to the size of the cold-tip. Giving exact numbers for the power dissipation is difficult, because this depends on various parameters including the amount of electrical leads and radiative heat load. As indication, the power dissipation can be up to about 50 mW.

A conceptual design of a micromachined JT cold stage - photon detector array is made that focuses on the interface between a JT cold stage and a detector array

and on the wiring of the array. To integrate a detector array with a cold stage, a silicon to D263 T glass bond has to be formed. This bond should be highly thermally conducting, suitable for use at cryogenic temperatures, strong enough to withstand launch vibrations and differences in thermal expansion of both materials, and outgassing should be very low. Among various techniques used in micro-electro-mechanical-systems (MEMS) technology to form a silicon to glass bond, adhesive bonding is selected as the most suitable technique. Various thermally conducting adhesives were experimentally tested and these tests showed that two-component adhesives can be used. The use of adhesives that meet NASA low outgassing specifications, for example the tested adhesive Stycast™ 2850 FT with catalyst 9, is advised.

State-of-the-art detector arrays require a large amount of electrical connections to the warm-end electronics. Therefore, it is important to minimize the parasitic heat load on the cold-tip of the JT cold stage due to heat conduction through the wires. Each wire should be optimized in terms of acceptable impedance and thermal heat load. Considering that a wire is allowed to have a certain resistance, it is shown that the use of bad electrical conductors (i.e. manganin or constantin) results in a larger heat load than the use of good electrical conductors (for example copper or gold). In our application, the wiring of the detector arrays can best be done by making a three layer stack on top of the JT cold stage consisting of an electrically well conducting layer, an insulating layer and a gold layer. Electrical leads can be structured in the first layer along the length of the cold stage and the gold layer on top is used to minimize the radiative heat load. At the cold end, aluminum wire bonding can be used to make the electrical connections from the leads to the detector array.

The application of miniature JT coolers in the temperature range of 65 - 250 K was investigated. The most suitable working fluid for a JT cold stage operating at a specific temperature in this range was selected on basis of the coefficient of performance, defined as the ratio of gross cooling power to the change in Gibbs free energy of the fluid during compression. In addition, a figure of merit (FOM) is introduced that gives a measure for the efficiency of heat exchange in the counter-flow heat exchanger (CFHX). The larger the FOM, the shorter the CFHX can be. The most suitable working fluids in a specific temperature range are nitrogen (65 - 70 K), carbon monoxide (70 - 77 K), oxygen (77 - 84 K), argon (84 - 95 K), methane (95 - 124 K), nitrogen trifluoride (124 - 146 K), ethylene (146 - 159 K), ethane (159 - 188 K), hydrogen sulfide (188 - 212 K) and ammonia (212 - 250 K). The non-toxic alternatives nitrogen (70 - 77 K), methane (124 - 146 K), ethane (188 - 200 K) and propane (200 - 250 K) were suggested for the toxic working fluids. Furthermore, it appears that the warm-end temperature and the maximum attainable high pressure do not play a role in the selection of the most suitable working fluid.

To investigate whether existing JT coolers can be operated with different working fluids a theoretical analysis was developed. This analysis is based on the critical components of a miniature JT cold stage in terms of its thermodynamic performance, which are the CFHX and the flow restriction. The analysis showed that all optimum

working fluids listed above can be used in a JT cold stage that is optimized for operating with nitrogen. This analysis was validated with experimental data.

For cooling small optical detector arrays, a second generation of micromachined JT cold stages was designed and fabricated consisting of two types: a high cooling-power cold stage and a low cooling-power cold stage with gross cooling powers around 250 mW and 50 mW at 100 K, respectively. Temperature profiles along the length of the CFHXs of both types were measured as well as their net cooling powers. During the experiments, the fluid was supplied from a pressurized gas bottle. Operating with nitrogen at a low pressure of 6 bar, a net cooling power of 26 mW at 100 K was measured for the low cooling-power cold stage and 131 mW at 100 K for the high cooling-power cold stage. In contrast to our expectations, no isothermal two-phase region was formed in the evaporator. Between two temperature sensors placed on both ends of the evaporator, a temperature difference of 40 K was measured for the high cooling-power cold stage and a difference of 14 K for the low cooling-power cold stage. Furthermore, it was observed that droplets flowed into the CFHX.

These experiments were also done for both JT cold stages operating with methane at a low pressure of 4 bar. The cold stages cooled down to about 140 K. For the high cooling-power cold stage again a temperature difference over the evaporator was measured after cool down. However, in the low cooling-power cold stage an isothermal two-phase region of 10 x 10 mm^2 was formed at the cold tip. Unfortunately, it was not possible to measure the cooling powers of the JT cold stages that were operated with methane, because clogging of the restriction was occurring while supplying heat to the cold tip.

In order to measure the performance of both JT cold stages cooling a (dummy) detector array, a silicon slice covered with a thin layer of gold was glued to the cold-tip. Experiments were done for both cold stages operating with nitrogen and methane. In all experiments, a constant temperature over the silicon slice was measured. The high cooling-power cold stage showed a net cooling power of 133 mW at 100 K for nitrogen and 110 mW at 140 K for methane. This means that both have sufficient cooling power to cool detector arrays that have a power dissipation of 30 mW and require about 50 electrical connections to their warm-end electronics. The low cooling-power cold stage operating with methane has a net cooling power of 28 mW at 140 K and can only be used for cooling detector arrays that have a power dissipation of a few milliwatts and require very few electrical connections. Operating with nitrogen, the low cooling-power cold stage has not enough cooling power to cool a detector array at all.

To obtain closed-cycle JT cooling, a miniature JT cold stage was combined with a linear compressor of the Rutherford Appleton Laboratory. Because this compressor can deliver a relatively modest compression of 1 to 10 bar, a mixed-refrigerant has to be used as the working fluid in the miniature JT cold stage. Based on optimizing the minimum isothermal enthalpy difference over the entire operating temperature range, a ternary mixture with a composition of 39 mol% methane, 20 mol% ethane and 41 mol% isobutane was selected that can cool down to about 150 K.

The performance of the linear compressor operating with the selected mixed-refrigerant was mapped. A compression of 1.5 to 10.7 bar was obtained at zero mass-flow rate. For a mass-flow rate of 10 mg s^{-1}, a compression of 1.8 bar to 9.4 bar was measured. Therefore, this compressor is suitable for obtaining a distributed cooling system. The compressor was combined with the high cooling-power JT cold stage. The JT cold stage could not cool down to below 284 K due to the low mass-flow rate of 0.16 mg s^{-1}, resulting in a too low cooling power. During the cool down phase, the mass-flow rate did not increase as is the case with pure fluids. It, therefore, did not have sufficient cooling power to fully cool down the cold stage.

Samenvatting

(Summary in Dutch)

Trillingsvrije miniatuur Joule-Thomson (JT) koelers zijn een interessante optie voor het koelen van elektronica met weinig tot geen dissipatie, zoals optische detectoren, lage ruis versterkers, halfgeleidende elektronica en supergeleidende elektronica. Deze applicaties worden onder andere gekoeld om de thermische ruis te verminderen, de bandbreedte te vergroten of om supergeleiding te verkrijgen. In dit proefschrift is het koelen van optische detectoren in het temperatuurgebied 65 - 300 K met miniatuur JT koelers voor toekomstige ruimtevaartmissies onderzocht. Het doel van het onderzoek is het ontwikkelen van een gedistributeerd koelsysteem waarin één enkele compressor gecombineerd wordt met meerdere miniatuur JT koelers die elk een kleine optische detector koelen.

Via een literatuur studie zijn de optische detectoren die gebruikt worden in de ruimtevaart in kaart gebracht. De studie heeft aangetoond dat alleen fotondetectoren gemaakt van silicium, indium-gallium-arsenide en kwik-cadmium-telluride relevant zijn om te combineren met ééntraps JT koelers. De in dit proefschrift besproken miniatuur JT koelers zijn gemaakt van glas, hebben een koud oppervlak van ongeveer 10 x 10 mm^2 en een netto koelvermogen tot 150 mW op 100 K. Dit betekent dat de optische detectoren uit maximaal 512 x 512 pixels kunnen bestaan als aangenomen wordt dat de pixelgrootte 15 x 15 μm^2 is. Het is moeilijk om exacte specificaties te geven voor de toegestane dissipatie van de detector. Deze zijn afhankelijk van verschillende parameters, zoals het

aantal elektrische connecties naar de warme kant en de stralingsinlek. Als indicatie kan een waarde van 50 mW aangehouden worden.

Er is een conceptueel ontwerp gemaakt van een miniatuur JT koeler geïntegreerd met een fotondetector, waarin de focus lag op de integratie van de koeler met de detector en het optimaliseren van de bedrading van de detector. Voor de integratie moet er een silicium - D263 T glas verbinding gemaakt worden. Deze verbinding moet goed thermisch geleiden, bestand zijn tegen cryogene temperaturen, sterk genoeg zijn om de lanceervibraties te weerstaan en het verschil in thermische uitzetting van beide materialen opvangen. Verder moet de verbinding nauwelijks uitgassen. Na het in kaart brengen van verschillende technieken die gebruikt worden voor het maken van een silicium-glas verbinding is er voor een lijmverbinding gekozen. We hebben verschillende thermisch geleidende lijmen experimenteel getest en het is gebleken dat de geteste 2-componenten lijmen geschikt zijn voor onze toepassing. Een goede optie is Stycast™ 2850 FT met katalysator 9, omdat deze voldoet aan NASA's standaard voor lage uitgassing.

Huidige optische detectoren hebben veel elektrische connecties naar de elektronica aan de warme kant. De warmtegeleiding door deze connecties zorgt voor een grote parasitaire warmteinlek. Het is van belang om deze warmteinlek te minimaliseren door middel van het optimaliseren van de weerstand van elk elektrisch draadje in combinatie met de thermische warmteinlek. Het is aangetoond dat als een draadje is gemaakt van een slechte elektrische geleider (bijv. manganine en constantaan) de warmteinlek groter is dan wanneer het draadje is gemaakt van een goede elektrische geleider (bijv. koper en goud). Voor het koelen van optische detectoren kan de bedrading het best in een 3-laags structuur gemaakt worden boven op de koeler, bestaande uit een goed elektrisch geleidende laag, een isolerende laag en een afdekkende goudlaag. In de eerste laag worden de elektrische connecties gestructureerd. De afdekkende goudlaag werkt als een stralingsscherm om de warmteinlek door straling te minimaliseren. Standaard aluminium 'bond wiring' kan gebruikt worden om de elektrische verbindingen tussen de detector en de koeler te maken.

De toepassing van JT koelers in het temperatuurgebied van 65 - 250 K is onderzocht. Het meest geschikte werkgas voor een JT koeler die koelt naar een specifieke temperatuur binnen dit gebied is geselecteerd op basis van de 'Coefficient of Performance' (*COP*). De *COP* is gedefinieerd als de ratio van het bruto koelvermogen tot de Gibbs vrije energie van het werkgas tijdens de compressie. Ook is er een 'Figure of Merit' (FOM) gedefinieerd dat een maat geeft voor de efficiëntie van warmte-uitwisseling in de tegenstroomwarmtewisselaar (TSWW). Hoe hoger de FOM, hoe korter de TSWW kan zijn. De meest geschikte werkgassen in een specifiek temperatuurgebied zijn stikstof (65 - 70 K), koolstofmonoxide (70 - 77 K), zuurstof (77 - 84 K), argon (84 - 95 K), methaan (95 - 124 K), stikstoftrifluoride (124 - 146 K), ethyleen (146 - 159 K), ethaan (159 - 188 K), waterstofsulfide (188 - 212 K) en ammonia (212 - 250 K). Als alternatief voor de giftige werkgassen zijn de niet giftige gassen stikstof (70 - 77 K), methaan (124 - 146 K), ethaan (188 - 200 K) en propaan (200 - 250 K) geselecteerd. Het is aangetoond dat de temperatuur aan de warme kant en de geselecteerde maximale hoge druk geen rol spelen

in de selectie van het meest geschikte werkgas.

Via een theoretische studie is onderzocht of bestaande miniatuur JT koelers kunnen opereren met andere werkgassen dan die waarvoor ze geoptimaliseerd zijn. Deze studie is gebaseerd op de kritieke elementen van miniatuur JT koelers in thermodynamisch opzicht, namelijk de TSWW en de restrictie. De studie toont aan dat alle bovenstaande meest geschikte werkgassen gebruikt kunnen worden in een miniatuur JT koeler die geoptimaliseerd is voor stikstof. De studie is gevalideerd met experimentele data.

Er is een tweede generatie miniatuur JT koelers voor het koelen van kleine optische detectoren ontwikkeld en gefabriceerd, bestaande uit twee koeler types: een hoog vermogen koeler en een laag vermogen koeler met een bruto koelvermogen van respectievelijk 250 mW en 50 mW op 100 K. Het temperatuurprofiel langs de TSWW en het netto koelvermogen zijn gemeten voor beide koelers. Tijdens de metingen is het werkgas aangeboden vanuit een gasfles. Met stikstof als werkgas bij een lage druk van 6 bar is er een netto koelvermogen van 26 mW op 100 K gemeten voor de laag vermogen koeler en 131 mW op 100 K voor de hoog vermogen koeler. In tegenstelling tot onze verwachtingen ontstond er geen isothermisch twee-fase gebied in de verdamper van beide koelers. Tussen twee temperatuursensoren, geplaatst aan beide uiteinden van de verdamper, is er een temperatuurverschil van 40 K gemeten voor de hoog vermogen koeler en een verschil van 14 K voor de laag vermogen koeler. Ook stroomden er druppeltjes met hoge snelheid de TSWW in.

Dezelfde experimenten zijn uitgevoerd voor beide koelers met methaan als werkgas bij een lage druk van 4 bar resulterend in een temperatuur van ongeveer 140 K. Opnieuw is er een temperatuurverschil over de verdamper gemeten voor de hoog vermogen koeler. De laag vermogen koeler heeft een isothermisch twee-fase gebied van 10 x 10 mm^2. Het was niet mogelijk om het netto koelvermogen van deze koelers te meten. Het aanbieden van warmte aan de koude kant resulteerde in een afname van de massastroom door de depositie van ijs in de restrictie. Dit zorgde uiteindelijk voor het verstoppen van de restrictie en opwarming van de koeler.

De prestaties van beide koelers terwijl ze een detector koelen is gemeten door een silicium plakje afgedekt met een dun laagje goud op de koude kant te lijmen. Er zijn metingen gedaan met stikstof en methaan als werkgas. Tijdens alle experimenten is er een isotherme temperatuur over het silicium plakje gemeten. De hoog vermogen koeler heeft een netto koelvermogen van 133 mW op 100 K voor stikstof en 110 mW op 140 K voor methaan. Beide koelers hebben dus genoeg koelvermogen om een detector te koelen met een dissipatie van 30 mW en 50 elektrische connecties naar de elektronica aan de warme kant. De laag vermogen koeler heeft een netto koelvermogen van 28 mW op 140 K voor methaan en is alleen geschikt voor detectoren met een dissipatie van een aantal milliwatts en heel weinig elektrische connecties. Met stikstof als werkgas heeft de laag vermogen koeler te weinig koelvermogen (8 mW) voor het koelen van een detector.

Om een gesloten koelcyclus te maken is de hoogvermogen JT koeler gecombineerd met een lineaire compressor van het Rutherford Appleton Laboratory. Deze compressor

levert een relatief kleine compressie van 1 tot 10 bar. Om die reden moet er een gasmengsel worden gebruikt als werkgas in de koelcyclus. Het gasmengsel is geselecteerd op basis van het maximaliseren van het minimale isotherme enthalpieverschil over het gehele temperatuurgebied waarover de koeler opereert. Er is gekozen voor een gasmengsel bestaande uit 3 componenten met een samenstelling van 39 mol% methaan, 20 mol% ethaan en 41 mol% isobutaan. Dit gasmengsel kan koelen tot ongeveer 150 K.

Eerst is de prestatie van de lineaire compressor met het gasmengsel gemeten. Wanneer er geen massastroom is wordt er een compressie van 1.5 tot 10.7 bar gehaald. De compressie voor een massastroom van 10 mg s^{-1} is 1.8 tot 9.4 bar. Dit maakt de compressor geschikt voor het gebruik in een gedistributeerd koelsysteem. Daarna is de lineaire compressor gecombineerd met de hoog vermogen koeler. De koeler koelde niet verder af dan 284 K vanwege de lage massastroom van 0.16 mg s^{-1}. Dit resulteerde in een te laag koelvermogen. Tijdens de afkoelfase nam de massastroom niet toe, zoals het doet voor pure gassen. De koeler had dus niet genoeg koelvermogen om zichzelf volledig af te koelen.

List of publications

J.H. Derking, H.J. Holland, P.P.P.M. Lerou, T. Tirolien and H.J.M. ter Brake, *Micromachined Joule-Thomson cold stages operating in the temperature range 80 - 250 K*, submitted to Int. J. Refr., (2011).

M. Garcia, **J.H. Derking**, C.H. Vermeer, H.J. Holland, P.P.P.M. Lerou and H.J.M. ter Brake, *How to prevent clogging in micromachined cryogenic coolers*, submitted to Appl. Phys. Lett., (2011).

J.H. Derking, H.J.M. ter Brake, A. Sirbi, M. Linder and H. Rogalla, *Optimization of the working fluid in a Joule-Thomson cold stage*, Cryogenics, **49**, 151-157, (2009).

H.J.M. ter Brake, **J.H. Derking**, H. Chao, H.J. Holland, M. Garcia, A.V. Mudaliar and P.P.P.M. Lerou, *Microcooling developments at the University of Twente*, In: Proc. ICEC **23**, 67-72, (2011).

J.H. Derking, D.W. Zalewski, M. Garcia, H.J. Holland, A.V. Mudaliar, H. Chao, P.P.P.M. Lerou and H.J.M. ter Brake, *Progress in Joule-Thomson microcooling at the University of Twente*, Cryocoolers **16**, 463-471, ICC Press: Boulder CO, USA, (2010).

J.H. Derking, H.J.M. ter Brake, M. Linder and H. Rogalla, *Interfacing issues in microcooling of optical detectors in space applications*, Adv. Cryog. Eng. **55**, 617-624, (2010).

J.H. Derking, H.J.M. ter Brake, A. Sirbi, M. Linder and H. Rogalla, *On-chip cooling for detectors in space applications*, In: Proceedings of the 7th IEEE conference of sensors, 1436-1439, IEEE Sensors 2008, October 27-29, (2008).

J.H. Derking, H.J.M. ter Brake, A. Sirbi, M. Linder and H. Rogalla, *On-chip cooling for detectors in space applications*, In: Proceedings of the 7th International conference on space optics, October 14-17, (2008).

J.H. Derking, H.J.M. ter Brake, A. Sirbi, M. Linder and H. Rogalla, *On-chip detector cooling for space applications*, Cryocoolers **15**, 405-413, ICC Press: Boulder CO, USA, (2008).

Dankwoord

(Acknowledgements)

Met het schrijven van dit dankwoord ben ik aan het einde gekomen van mijn promotie-traject. Na het behalen van de bul, was ik op zoek naar een promotie-opdracht. Marcel had een erg leuke positie vrij op het gebied van cryogene koelers. Dat betekende wel een verandering van werkveld van de SQUIDs naar de cryogene koeltechnieken. Ik heb geen moment spijt gehad van deze keuze. Het resultaat van 4 jaar onderzoek ligt in de vorm van dit proefschrift voor je. Aangezien je promoveren niet alleen doet, wil ik op deze plek alle mensen bedanken die mij hebben geholpen tijdens dit traject. Een paar mensen wil ik in het bijzonder noemen.

Op de eerste plaats wil ik mijn promotor Marcel ter Brake bedanken. Marcel had 4.5 jaar geleden een leuke promotie-opdracht liggen en na een aantal intensieve gesprekken mocht ik als promovendus beginnen. De vele inhoudelijke discussie hebben geleid tot dit proefschrift. Je deur stond altijd open voor vragen en discussies, zelfs nu je de laatste 1.5 jaar heel erg druk bent met je nieuwe positie als professor. Ook de conferentiebezoeken aan Noordwijk, Long Beach, Toulouse en Spokane zal ik niet vergeten. Het incheckverhaal van Spokane blijft hilarisch! Naast het werk toonde je altijd interesse in de persoonlijke situatie en elke maandag was het weer tijd om de stand van zaken in het voetbal te bespreken. Heel erg bedankt voor alles!

Zodra je wat in het lab wilt doen kom je automatisch bij Harry en Cris terecht. Harry is de technische vraagbaak van de groep en heeft ontzettend veel kennis op het gebied

van cryogene technieken. Naast assistentie in het lab kan je ook altijd voor inhoudelijke discussies over het werk bij Harry terecht. Ongeveer 1.5 jaar geleden is Cris erbij gekomen in de groep. Ook Cris staat altijd voor je klaar als er weer een opstelling in elkaar geschroefd moet worden. Beide zijn ook altijd in voor een bak koffie, een goed gesprek of een last-minute vrijdagmiddag experiment. Via deze weg wil ik jullie beide bedanken voor al de hulp, de vele discussies tijdens het koffiedrinken en de gezellige lunches en borrels.

Tijdens de promotie heb ik samengewerkt met verschillende onderzoeksinstituten. The research was done under ESA contract and I have worked for a short period at ESTEC in Noordwijk. It was a pleasure working together with Thierry, Martin and Adriana, the project officers at ESA. Thanks a lot for all the input during the project. Also, I want to thank James for his help with thermal modeling in ESATAN, Didier for his input on optical detectors and the people of the thermal group at ESTEC for their hospitality during my stay at ESTEC.

Samen met de Universiteit Delft en TNO hebben we gekeken naar het koelen van een zonsensor die gebruikt wordt voor de positiebepaling van satellieten. Graag wil ik Albert, Johan, Ning en Yue bedanken voor de samenwerking. Helaas is het koelen van de sensor op niets uitgelopen. For the distributed cooling system, we used a compressor of the Rutherford Appleton Laboratory. I want to thank Martin and Tom for their willingness to collaborate in this research effort, their hospitality during my stay at RAL and the compressor driving lessons. Unfortunately, the existing micro cold stages were not suitable for combining with the compressor, but when the new run of cold stages arrive we certainly will go on with this work.

De microkoeling groep bestaande uit Marcel, Harry, Cris, Dawid, Srini en Haishan wil ik bedanken voor de input tijdens de werkbesprekingen. Mijn voorganger, Pieter, heeft de koelers ontworpen en het productieproces begeleid. Bedankt en veel succes met het op de kaart zetten van Kryoz Technologies. Dat het een groot succes mag worden!

Tijdens de afgelopen 4.5 jaar heb ik vanwege de verhuizing naar Carre drie verschillende werkplekken gehad. Met name mijn kamergenoten Dawid, Michael, Haishan en Harald wil ik bedanken voor de gezelligheid en sfeer op de werkplek. Ook wil ik bij deze nog de andere leden van de 'koeling' groep, Johannes, Robert-Jan, Wilco en Roger, bedanken voor de discussies en gezelligheid tijden lunches, borrels en andere gelegenheden.

Geen promovendus kan zonder de ondersteuning van Ans en Inke, de secretaresses van de groep. Ze staan altijd voor je klaar voor het boeken van een reis, het invullen van papieren rompslomp en zelfs het zoeken van tijdelijke woonruimte. Ook staat de deur altijd open voor een gezellig gesprek. Bedankt! Verder wil ik alle vaste staf, technici, post-docs, AIO's en studenten van EMS, ICE en LT bedanken voor de gezelligheid tijdens de koffiepauzes en borrels.

Naast hard werken is de nodige onspanning ook een pré om te kunnen presteren. Mijn kroegmaten, vakantiegenoten en fietsvrienden, Maarten, Jeroen en Pieter, hebben hier een

belangrijke bijdrage aan geleverd. Amsterdam, Valkenburg, de Ardennen, Chersonissos en het 'foute' Llorett en Salou. Een aantal uit de lijst van plaatsen waar we de afgelopen 12 jaar geweest zijn. Ondanks dat de avondjes stappen wel eens een kater opleverde, zorgde het ook voor veel ontspanning. Bedankt! Ook wil ik mijn oud-flatgenoot, vriend en fitnessmaat Andre noemen. Bedankt voor de gezellige bier drink avondjes, en de discussies over voetbal en andere zaken.

Sonja heeft alles van heel dichtbij meegemaakt. De stage in het buitenland, het afstuderen, samenwonen en het promotie-onderzoek. Ze heeft me gesteund tijdens al deze momenten en stond altijd voor me klaar. De kampeervakanties, het wandelen in de bergen, de verre reizen naar Gambia en Ecuador en de vele stedentrips naar onder andere Berlijn, Rome en Parijs waren super. Ook de korte vakanties in eigen land en de vele fiets- en wandeltochtjes zal ik nooit vergeten. Sonja, heel erg bedankt voor de leuke tijd!

Op de laatste, maar zeker niet de minste plaats, wil ik mijn naaste familie, Pap, Mam, Corlien, Ronald, Richard, Sander en Georgette bedanken voor alle steun en gezelligheid. Zeker in de laatste maanden van het traject kwam de steun op het goede moment.

Na 12 jaar wonen in de mooie stad Enschede is voor mij de tijd aangebroken om verder te trekken. Het buitenland lonkt, een spannende tijd breekt aan. Ongetwijfeld wordt ook dat een periode om nooit te vergeten!

Hendrie

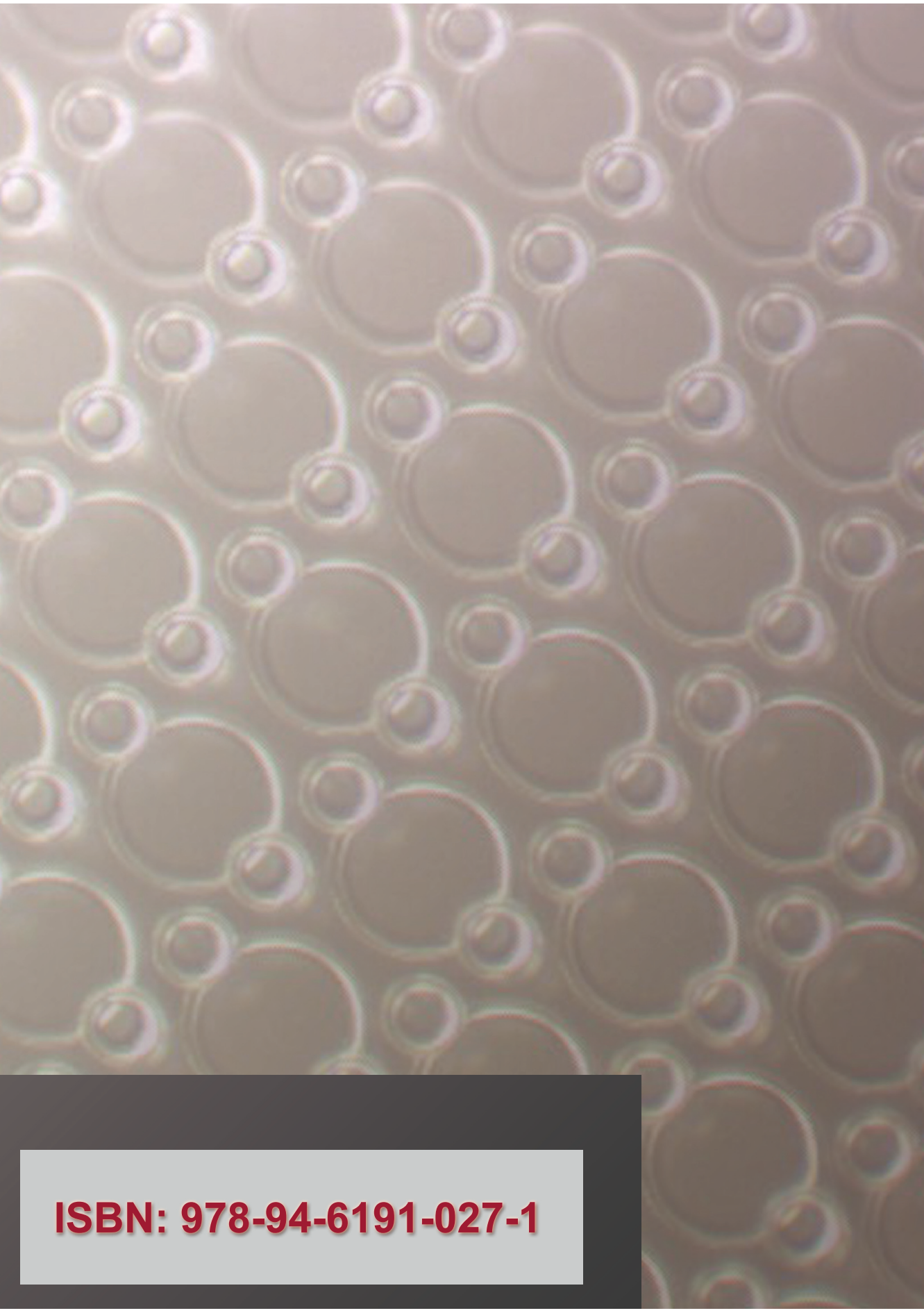

ISBN: 978-94-6191-027-1